



Università degli Studi di Pavia
Facoltà di Ingegneria



Gent Universiteit
Faculteit
Ingenieurswetenschappen

Finite Element Analysis of Carotid Artery Stenting

by

Michele Conti

A Thesis submitted in Partial Fulfilment of the Requirements
for the Degree of Doctor in Philosophy in

Bioengineering and Bioinformatics
at Università degli Studi di Pavia, Pavia, Italy

and

Biomedical Engineering (Joint PhD)
at Ghent University, Ghent, Belgium

Supervisors:

Prof. F. Auricchio - Università degli Studi di Pavia

Prof. B. Verheghe - Ghent University

Dr. M. De Beule - Ghent University

Accademic Year: 2009-2010

Acknowledgements

Cu nescia rinescia - detto siciliano
Cu torna rinascia - questo lo aggiungo io...

These three years of PhD have provided me the opportunity to carry out several activities, mostly resumed in this dissertation, but also have contributed to my personal growth; there are several people without whom this great experience would not have been possible and whom I need to thank.

I want to thank Prof. Ferdinando Auricchio for his great support, kindness and professional competence; I really have learnt a lot from his way to approach and solve the problems and from his enthusiasm for research.

I thank Dr. Matthieu De Beule for introducing me into the fascinating research field of computational biomechanics and for providing me the opportunity of joint PhD. I'm really grateful to him for keeping my motivation high during these three years and for long-lasting support to our research collaboration.

I wish also to thank Prof. Verheghe for supervising the joint PhD activities and for his useful technical suggestions.

I want to thank Eng. Simone Morganti since I've got the privilege to share the enthusiasm for research work with a good friend. Thanks to Dr. Alessandro and Elisa Reali for their support and useful suggestions. Many thanks to my lab colleagues, here in Pavia, who have contributed to transform the rooms of Structural Mechanics Department in a nice and cosy place to work; so thanks Anna, Balduzzi, Giuseppe, Enrico, Jamal, Carolina, Adrien. Many thanks also to Prof. P. Segers, Prof. P. Verdonck and my colleagues of IBiTech, who have contributed to make my stay in Ghent fruitful and pleasant. Thanks to Gianluca, Aniello, Francesco, "ministro" Andrea and the all italian crew in Ghent, who have brought in Belgium a home atmo-

sphere.

Thanks to my parents, who give me an unconditional support for what I'm doing.

Finally, my best acknowledgements are for my personal reference point, Giovannella, who has sustained me during this period with her nice smile and deep love.

Pavia, January 2011

Contents

English summary	v
Italian summary	vii
Dutch summary	ix
1 Introduction and motivation	1
1.1 Carotid artery anatomy	2
1.2 Carotid artery stenosis	4
1.2.1 Atherosclerosis	4
1.2.2 Diagnosis	6
1.2.3 Measurement of stenosis degree	7
1.2.4 Treatment options for carotid artery stenosis	9
1.3 Carotid Artery Stenting: state-of-art, limitations and future directions	11
1.4 Thesis rationale and organization	15
2 Nitinol embolic protection filters: design investigation by finite element analysis	19
2.1 Introduction	19
2.2 Materials and Methods	21
2.2.1 Model geometry	21
2.2.2 Filter free expansion	24
2.2.3 Circumferential basket-vessel wall apposition	27
2.3 Results	29
2.3.1 Filter free expansion	29
2.3.2 Circumferential basket-vessel wall apposition	29
2.4 Limitations	32

2.5	Conclusions	32
3	Carotid artery stenting: from medical images to finite element analysis	33
3.1	Introduction	33
3.2	Materials and Methods	35
3.2.1	Patient-specific carotid artery model	35
3.2.2	Stent models	36
3.2.3	Finite element analysis of carotid artery stenting . . .	38
3.2.4	Post-processing	40
3.3	Results	42
3.3.1	von Mises stress in the post-stenting vessel wall	42
3.3.2	Lumen gain	42
3.3.3	Pre- and post-stenting tortuosity	43
3.4	Limitations	47
3.5	Conclusions	48
3.6	Appendix	49
3.6.1	Mesh convergence analysis	49
3.6.2	Kinetic-Internal energy ratio	49
4	Patient-specific finite element analysis of carotid artery stenting: a focus on the vessel modeling	53
4.1	Introduction	53
4.2	Material and Methods	55
4.2.1	Carotid artery model	55
4.2.2	Stent finite element model	71
4.2.3	Finite element analysis of carotid artery stenting . . .	71
4.2.4	Post-processing	72
4.3	Results	73
4.4	Discussion	79
4.5	Limitations	81
4.6	Conclusions	83
4.7	Appendix	84
4.7.1	Mesh convergence analysis	84
4.7.2	Assigning local coordinate system for fiber orientation	86

5	Impact of carotid stent cell design on vessel scaffolding: a case study comparing experimental investigation and numerical simulations	89
5.1	Introduction	89
5.2	Materials and Methods	93
5.2.1	Validation of patient-specific finite element analysis of carotid artery stenting	93
5.2.2	Vessel scaffolding evaluation	100
5.3	Results	101
5.3.1	Validation of patient-specific finite element analysis of carotid artery stenting	101
5.3.2	Vessel scaffolding evaluation	103
5.4	Limitations	106
5.5	Conclusions	106
6	Final remarks	109
6.1	Conclusions	109
6.2	Future works	112
	Bibliography	115

English summary

Cardiovascular diseases (CVDs) are nowadays the leading cause of death in the Western countries, corresponding to high social and economical costs. CVDs are often related to atherosclerosis, a degeneration of the vessel wall causing a number of events, ranging from arterial hardening to lumen narrowing (stenosis), potentially resulting in heart attack or stroke.

In particular atherosclerotic stenosis of the carotid artery (CA), narrowing the bifurcation neck, causes 20% of all ischemic strokes and transient ischemic attacks. Several treatment options are nowadays available for managing CA stenosis but, thanks also to the encouraging outcomes achieved for coronary stenosis treatment, the application of percutaneous minimally-invasive techniques, such as stenting, for CA revascularization is rapidly arising. Carotid artery stenting (CAS) is a procedure which restores the vessel patency by enlarging the narrowed lumen by the expansion of a metallic mesh, which is driven to the target lesion through a catheter, running inside an endoluminal path accessed by groin incision. A low profile angioplasty balloon can be used for predilation and an embolic protection device can be used to minimize the risk of ischemic attacks due to migration of clots, released during the procedure.

Design, development and performance assessment of the devices used in this procedure are the natural application field of (computational) biomechanics, which applies the principle of mechanics to investigate biological systems and their interaction with artificial implants. The present dissertation is collocated within this scenario since we use numerical simulations to investigate several aspects of carotid artery stenting (CAS), ranging from the performance assessment of embolic protection filters to modeling of CA. Furthermore, we mainly attempt to move a first step towards the application of numerical simulations of CAS to support the clinical practice, through

English summary

a quantitative assessment of the relation between the complex mechanical features of a given stent design and a given patient-specific anatomy.

Italian summary

Le malattie cardiovascolari (CVDs) sono oggi la causa principale di morte nei paesi Occidentali, comportando così alti costi economici e sociali. Le CVDs sono spesso legate all'aterosclerosi, degenerazione della parete vascolare, che causa l'irrigidimento delle arterie, la riduzione del lume vascolare (stenosi) e, in alcuni casi, eventi drammatici come infarto ed ictus.

In particolare, la stenosi della carotide causa il 20% di tutti gli ictus e gli attacchi ischemici temporanei. Diverse opzioni di trattamento sono ad oggi disponibili per la cura della stenosi carotidea ma, grazie anche agli incoraggianti risultati ottenuti nel distretto coronarico, l'uso di tecniche percutanee e minimamente-invasive, come lo stenting, è in rapida ascesa anche nel caso del distretto carotideo.

Lo stenting della carotide (CAS) è una procedura che ripristina la funzione vascolare allargando il lume dell'arteria tramite l'apposizione di una maglia metallica, stent, la quale viene guidata alla lesione per via endovascolare tramite un catetere. Un palloncino da angioplastica può essere usato per predilatate la stenosi; mentre un apposito dispositivo viene utilizzato per minimizzare il rischio di ischemie intra-operatorie dovute al rilascio di emboli da parte della placca.

La progettazione, lo sviluppo e la valutazione delle prestazioni dei dispositivi in questa procedura sono i naturali campi di applicazione della biomeccanica (computazionale), la quale applica i principi della meccanica allo studio dei sistemi biologici ed alla loro interazione con impianti artificiali.

La presente dissertazione si colloca in questo contesto, proponendo l'uso delle simulazioni numeriche per studiare diversi aspetti dello stenting carotideo: dalla valutazione dei filtri embolici alla modellazione della carotide. Inoltre lo studio condotto muove un primo passo verso l'applicazione delle simulazioni dello stenting carotideo a supporto della pratica clinica, at-

Italian summary

traverso un'oggettiva e quantitativa valutazione della relazione tra le proprietà meccaniche di un dato stent e l'anatomia vascolare, specifica del singolo paziente.

Dutch summary

Hart-en vaatziekten (CVDs) zijn tegenwoordig de belangrijkste doodsoorzaak in de Westerse landen, resulterend in hoge sociale en economische kosten. CVD's zijn vaak gerelateerd aan atherosclerose, een degeneratie van de vaatwand die kan zorgen voor arteriële verstijving tot vernauwing (stenose), mogelijk resulterend in een hartaanval of een beroerte.

In het bijzonder atherosclerotische stenose van de halsslagader (CA), het vernauwen van de nek van de bifurcatie, veroorzaakt 20 % van alle ischemische beroertes en transiente ischemische aanvallen. Tegenwoordig zijn verschillende opties beschikbaar voor de behandeling van CA stenose waaronder, mede dankzij de bemoedigende resultaten bereikt voor de revascularisatie van coronaire stenoses, de toepassing van percutane minimaal-invasieve technieken, zoals het gebruik van stents. Het behandelen van de halsslagader met een stent (CAS) is een procedure waarbij het vernauwde lumen vergroot wordt via de ontplooiing van een metalen veertje, dat via een kleine incisie in de lies met een katheter ter plaatse gebracht wordt. Tijdens deze ingreep kan een angioplastie ballon gebruikt worden voor predilatatie van de vernauwing en kan ook een hulpmiddel gebruikt worden om eventuele losgekomen partikels op te vangen.

Het ontwerp, de ontwikkeling en de beoordeling van de prestaties van de implantaten die gebruikt worden tijdens deze procedure zijn een interessante toepassing in het gebied van (computationele) biomechanica, waarin de beginselen van de mechanica toegepast worden om inzicht te verwerven in biologische systemen en hun interactie met kunstmatige implantaten. In dit proefschrift worden numerieke simulaties gebruikt om verschillende aspecten van het stenten van de halsslagader (CAS) te onderzoeken, variërend van de beoordeling van de prestaties van beschermingsfilters tot het modelleren van (patient-specifieke) CA stenting procedures.

Dutch summary

Dit werk kan gezien worden als een eerste stap naar de toepassing van numerieke simulaties van CAS ter ondersteuning van de klinische praktijk, door middel van een kwantitatieve beoordeling van de relatie tussen de complexe mechanische eigenschappen van een bepaald stent ontwerp en een bepaalde patiënt-specifieke anatomie.

Chapter 1

Introduction and motivation

Cardiovascular diseases (CVDs) is the generic name given to the dysfunctions of the cardiovascular system such as hypertension, coronary heart disease, heart failure or stroke. CVDs are nowadays the leading cause of death in the Western countries: a recent report of American Heart Association [1] states that, on the basis of 2006 mortality rate, nearly 2300 Americans die of CVD each day, an average of 1 death every 38 seconds. This data explains well the high incidence of such pathologies which lead to high social and economical costs; in fact, the estimated direct and indirect cost of CVD for 2010 is \$ 503.2 billion.

Among CVDs, stroke¹ has a significant incidence; approximately, every 40 seconds someone in the United States has a stroke. The pathologic events which lead to stroke are complex but most of them can be referred to atherosclerosis, a degeneration of the arterial wall, characterized by accumulation of cells, lipids, connective tissue, calcium, and other substances inside its inner layers resulting in the so-called atheroma or plaque.

Atherosclerosis is the potential source of a number of events, ranging from arterial hardening to narrowing of the vessel lumen, i.e. stenosis, which can lead to blockage of the blood flow. Atherosclerosis of the aorta and its branches and in particular carotid artery (CA) is one of the causes of stroke. Several treatment options are nowadays available for managing CA stenosis but, thanks also to the encouraging outcomes achieved for coronary stenosis treatment, the application of percutaneous minimally-invasive techniques,

¹Sudden diminution or loss of consciousness, sensation, and voluntary motion caused by rupture or obstruction (as by a clot) of a blood vessel of the brain.

such as stenting, is rapidly arising as treatment of CA stenosis. Carotid artery stenting (CAS) is a procedure which restores the vessel patency by enlarging the narrowed lumen by the expansion of a metallic mesh, which is driven to the target lesion through a catheter, running inside an endoluminal path accessed by groin incision. A low profile angioplasty balloon can be used for predilation and an embolic protection device can be used to minimize the risk of ischemic attacks due to migration of clots, released during the procedure.

Design, development and performance assessment of the devices used in this procedure are the natural application field of (computational) biomechanics, which applies the principle of mechanics to investigate biological systems and their interaction with artificial implants. The present dissertation is collocated within this scenario, as we use numerical simulation to investigate several aspects of CA stenting. In this chapter, we provide a brief introduction to the anatomical and pathological aspects of CA stenosis, highlighting the current treatment strategies to motivate the aim of the present dissertation and its organization.

1.1 Carotid artery anatomy

Following the path of blood flow ejected from the left ventricle, the aortic arch gives rise to the right brachiocephalic artery, the left CA and the left subclavian artery (see figure 1.1-a). The brachiocephalic artery and the left CA are more anterior on the arch (see figure 1.1-b). The right common carotid artery (CCA) and right vertebral arteries arise from the right brachiocephalic artery. The right CCA splits into the right internal (ICA) and the right external carotid arteries (ECA). The left CCA, arising directly from the aortic arch, gives rise to the left ICA and the left ECA. From figure 1.1-c it is possible to notice that the CA can be considered as the root of the cerebral vascular tree and this aspect underlines the importance of such artery for the cerebral function.

With respect to the vascular anatomy of the CA, the carotid bulb (see figure 1.1-d) refers to the region just proximal to the bifurcation of the ICA which supplies the anterior brain, the eye, the forehead, and the nose, giving rise also to many branches (e.g. hypophyseal artery, ophthalmic artery, etc.). The ECA arises anteriorly from the CCA and gives rise to multiple facial branches (e.g. anterior, posterior and ascending branches, etc.).

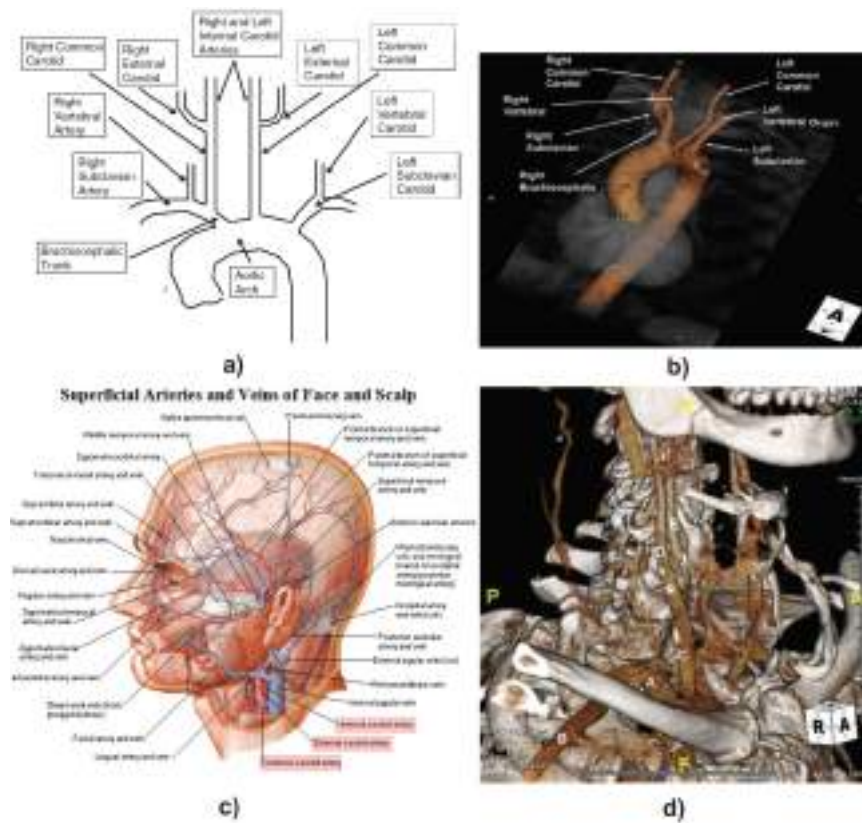


Figure 1.1: Representations of carotid artery vascular anatomy: a) illustrative scheme and b) 3D reconstruction from Computed Tomographic Angiography (CTA) of a normal aortic arch and its great vessels and branches (adapted from [2]); c) anatomical illustration of the head vascular tree (adapted from [3]); d) Anterior view of carotid artery anatomy reconstructed from CTA: carotid bulb (white asterisk), A: Right brachiocephalic artery, B: Right subclavian artery, C: Right common carotid artery (CCA), D: Right internal carotid artery (ICA), E: Right external carotid artery (ECA), F: Right vertebral artery.

1.2 Carotid artery stenosis

If, on the one hand, it is obvious that CA stenosis can potentially lead to neurological complications, on the other hand, it is not trivial to relate the mechanisms underlying the appearance of such a phenomenon and its neurological consequences. In order to elucidate this relation, in this section atherosclerosis progression is briefly described, and then medical imaging techniques used for the diagnosis of CA stenosis are discussed, highlighting finally the current treatment options and the corresponding selection criteria.

1.2.1 Atherosclerosis

Atherosclerosis can be roughly defined as a local inflammatory disease of arteries, which primarily impairs vessel patency. As depicted in figure 1.2, the pathogenesis of the plaque is characterized by a cascade of bio-chemical events which can be resumed² in the following steps:

- initiation of the plaque formation: endothelial dysfunction of the vessel wall and lipoprotein retention;
- starting of the inflammatory response: adhesion of leukocytes to the endothelial surface;
- formation of fatty streak: migration of monocytes within the artery wall and formation of foam cells;
- progression of the lesion (stable plaque): vascular smooth muscle cell migration and proliferation;
- progression of the lesion (unstable plaque): formation of the fibrous cap, plaque rupture and thrombus formation.

From the above mentioned description, it is clear that the classification of the stenotic lesion depends on both the pathology stage and the plaque composition; in fact, as atherosclerosis progresses, the plaque leads to vessel wall thickening, changing also its morphology, becoming a complex structure characterized by several components (e.g. lipid pool, necrotic core,

²Since the detailed description of this stages is beyond the goal of the present dissertation, for a deep understanding of atherosclerosis pathogenesis we invite the reader to refer to the excellent study of George S.J and colleagues [4].

calcified nodules, etc.). All the plaque components contribute to plaque stability; in fact, in the final stage the atheroma may either become stable, thus impairing only the blood flow, or unstable, thus being thrombogenic.

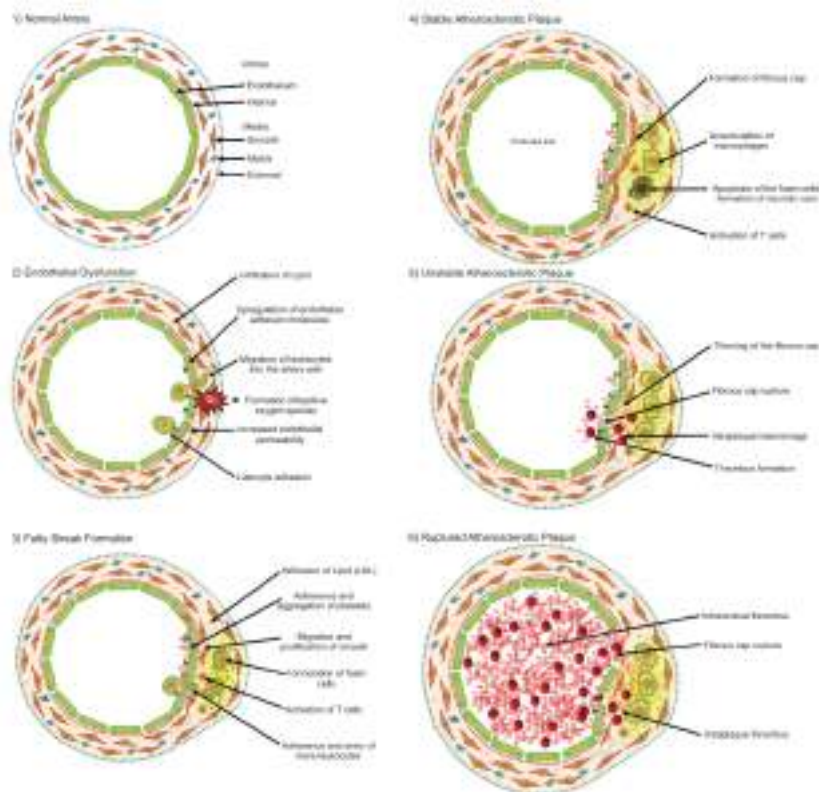


Figure 1.2: Illustrative representation of the main steps of atherosclerosis disease progression. Adapted from [4].

1.2.2 Diagnosis

As highlighted in section 1.2.1, both stenosis degree and plaque composition contribute to define the risk level of stroke; consequently, the current diagnosis of CA stenosis has a dual aim: i) evaluation of the stenosis degree (luminal imaging techniques); ii) assessment of plaque composition and its stability (morphological plaque imaging). Given the rapid evolution in medical imaging, different methods are nowadays available for the diagnosis of CA stenosis; clearly each of them having advantages and drawbacks and they often are combined to maximize the information for optimal treatment planning.

In the following a brief description, based on the excellent survey of Gillard and colleagues [5], of CA diagnostic medical imaging techniques is reported. The main medical imaging techniques used for CA stenosis visualization are:

- Digital Subtraction Angiography (DSA);
- Doppler Ultrasound (or Carotid Duplex);
- Magnetic resonance angiography (MRA);
- Computed Tomographic Angiography (CTA).

Digital Subtraction Angiography (DSA) is a fluoroscopy technique used to assess the severity of luminal stenosis. It was routinely used during the NASCET and ECST trials³. For this reason, it became the standard for stenosis assessment though its use is nowadays declining because of new non-invasive technique (e.g. MRA, CTA). Moreover DSA requires high cathetering skills, is not a low-cost procedure, and has also high rate of neurological complications.

Doppler Ultrasound (or Carotid Duplex) uses spectral Doppler, color-flow, and B-mode (gray-scale) to mainly determine the flow velocity at different CA regions. Color-Doppler imaging supports the assessment of stenosis severity, while B-mode provides information regarding plaque morphology such as surface irregularity, ulceration or echolucency. This technique has the advantages to be cost-effective and non-invasive but the accuracy of the

³These clinical trials [6, 7] demonstrated the superiority of surgery over medical therapy in symptomatic patients with severe CA stenosis. Symptomatic patients are usually defined as individuals with transient ischemic attacks (TIAs), unilateral transient monocular blindness (amaurosis fugax), or non-disabling stroke on the same side as the carotid artery stenosis.

obtained diagnostic criteria may vary between laboratories or may be biased by the operator skills.

The term Magnetic Resonance Angiography (MRA) indicates a series of MRI techniques, which are used to non-invasively characterize vascular structures, i.e. Contrast enhanced (CE-MRA), Time-of-flight (TOF), Phase-contrast (PC-MRA). With respect to CA stenosis, the impressive technological advancements for both MR hardware and softwares have supported the wide-spreading of MRA, which can be now considered as one of the leading non-invasive modalities to image the CA. MRA is currently used to both characterize the vascular anatomy and the plaque (including fibrous cap thickness and disruption, intra-plaque lipid content and hemorrhage). MRA has several advantages, as the avoidance of nephrotoxic contrast and ionization radiation, but the diagnostic exam cannot be performed on subject with pacemakers, implantable defibrillators or suffering obesity and claustrophobia.

Computed Tomographic Angiography (CTA) is a medical imaging technique used to obtain an accurate reconstruction of the CA lumen; it allows orthogonal carotid imaging and simultaneous intracranial evaluation. CTA offers high spacial resolution and it is a very fast technique but it has the drawback of using contrast dye and ionization radiations, which can be potentially harmful. Moreover bone and calcification artifacts affect CTA images but this issue has been mitigated by state-of-art data post-processing.

1.2.3 Measurement of stenosis degree

Accurate CA imaging and the related measurement of the degree of stenosis is the fundamental step in patient selection for CA stenosis treatment. A series of well-established methodologies to measure stenosis degree are based on a planar view of the CA luminal profile since, in the early 1990, NASCET and ECST trials stratified the stroke risk on lumen severity stenosis, which was measured with DSA in that period.

As depicted in figure 1.3, three different methods are used in literature to quantify CA stenosis:

1. NASCET method: the stenosis is calculated from the ratio of the most narrow luminal diameter of the diseased section of the artery to the diameter of the ICA beyond any post-stenotic dilation;
2. ECST method: the stenosis is calculated by comparing the most nar-

row luminal diameter to an estimated non-stenotic vessel diameter at the point of narrowing;

3. CC method: the stenosis is calculated using the ratio of the most narrow luminal diameter to the diameter of a normal segment of the CCA, proximal to the carotid bulb.

Clearly due to different approaches, there are several technical issues which should be taken into account to avoid measurement inaccuracy [8].

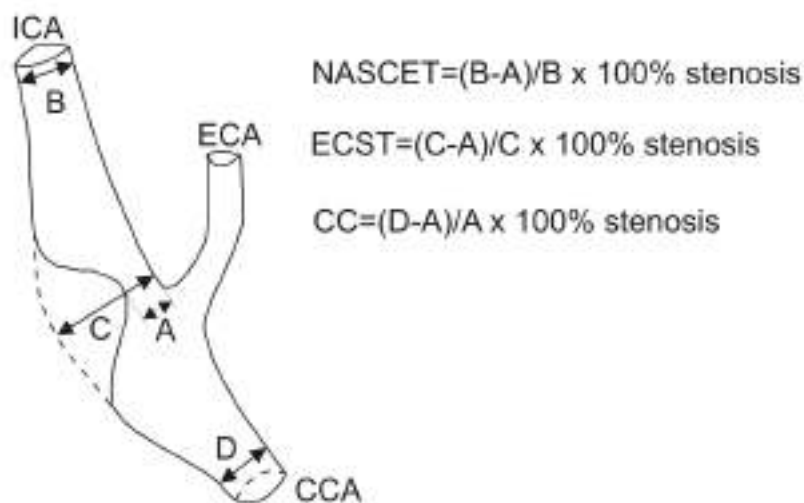


Figure 1.3: Schematic illustration of carotid artery bifurcation with internal carotid artery (ICA) stenosis illustrating the three different measurement methods.

1.2.4 Treatment options for carotid artery stenosis

There are three common treatment options for CA stenosis: 1) medical therapy; 2) carotid endarterectomy (CEA); 3) carotid artery stenting (CAS). The medical treatment usually consists of antiplatelet therapy (i.e. aspirin or clopidogrel) and aims mainly at limiting the progression of the disease and reducing the risk of stroke.

CEA is a surgical procedure which physically removes the source of emboli, i.e. the plaque, through an incision in the neck at the location of the blockage. During the procedure the blood flow is temporary re-routed using a tube, which is inserted above and below the blockage while the plaque is peeled away. After the procedure the CA can be closed with or without a patch (see figure 1.4).

CAS is a minimally invasive technique which aims at restoring the vessel patency through the deployment of tubular prosthesis, i.e. stent, potentially after the enlargement of the stenosis by balloon angioplasty; this procedure will be detailed in the next section. The selection criteria of the treatment strategy for CA stenosis are based on three main items: i) stenosis degree; ii) plaque vulnerability; iii) patient symptoms. In the following we report mainly the indications proposed by Bates and colleagues [9], who resume somehow the huge clinical literature regarding these criteria.

Sole medical therapy is preferred for: i) patient having low risk of stroke (symptomatic stenosis less than 50%, asymptomatic stenosis less than 60%); ii) high risk of procedure-related stroke; iii) any other case where the risk of revascularization is not justified by the consequent benefits.

CEA is recommended for: i) symptomatic patients with stenosis ranging from 50% to 99%, if the risk of perioperative stroke or death is less than 6%; ii) asymptomatic patients with stenosis ranging from 60% to 99%, if the risk of perioperative stroke or death is less than 3%.

CAS is considered as an evaluable option to CEA especially for high risk patients; the American health system (CMS) limits the reimbursement to CAS performed on high-risk patients with symptomatic stenosis greater than 50% or asymptomatic stenosis greater than 80%.

In a very recent paper, Yilmaz and colleagues [10] suggest the following indications for CAS: i) recurrent stenosis after CEA; ii) radiation-induced carotid stenosis; iii) anatomical features (high carotid bifurcation near the skull base); iv) tandem lesions (proximal CCA stenosis or distal stenosis in the carotid siphon associated with the carotid bifurcation stenosis).

Whether CEA is better than CAS or vice versa is a matter a debate, many (contrasting) research articles are dealing with this issue⁴, and a very recent clinical trial, Carotid Revascularization Endarterectomy versus Stent Trial (CREST), concludes that among patients with symptomatic or asymptomatic carotid stenosis, the risk of the composite primary outcome of stroke, myocardial infarction, or death did not differ significantly in the group undergoing CAS and the group undergoing CEA [12]; though it seems plausible that the clinical debate will continue [13].

In the following section we focus on current technical issues of CAS in order to highlight those limitations which can be investigated using the (computational) biomechanical methods.

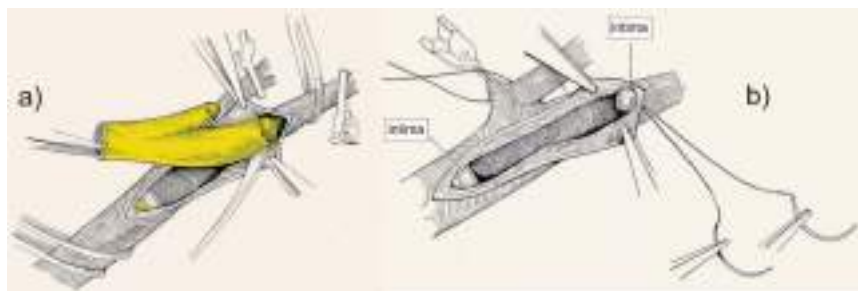


Figure 1.4: Carotid endarterectomy (CEA): a) the plaque has been separated from the outer wall of the common carotid artery (CCA) and external carotid artery (ECA) and is now being removed from the internal carotid artery; b) Arteriotomy closure; sutures are placed at the distal end of the arteriotomy with particular attention to suture both intimal and wall layers on both sides. Adapted from [5].

⁴For a detailed discussion about CAS vs CEA please refer to the work of Paraskevas and colleagues [11] and to the references therein reported.

1.3 Carotid Artery Stenting: state-of-art, limitations and future directions

Typical CAS procedure is a minimally invasive technique consisting of several steps [14, 15]:

1. pre-operative antiplatelet therapy: the patient is routinely placed on dual antiplatelet therapy; the treatment duration depends on the therapeutic option;
2. intravascular access performed mainly through the superficial femoral artery and selective catheterization of the CCA;
3. ICA access and crossing of the stenosis with embolic protection device (EPD);
4. EPD deployment (see figure 1.5-a);
5. lesion pre-dilation by balloon inflation (see figure 1.5-b): this allows the stent delivery system to be advanced without being constrained or trapped;
6. stent deployment (see figure 1.5-c);
7. post-dilation by balloon inflation and EPD retrieval (see figure 1.5-d).

The current procedure is the result of long-lasting process of technological improvements. In fact CAS is not certainly a brand-new technique as the first balloon angioplasty for carotid stenosis was performed in 1979, while 10 years later the first Palmaz-Schatz balloon expandable (BX) stent⁵ was deployed in the CA. Unfortunately CA stenting, at that time, had no great success since BX stents were prone to collapse, due to the external loading affecting the CA region; the reported restenosis rate due to stent compression ranges from 1% to 15% [17, 18, 19], moreover BX stents have unsuitable length for the CA region and low capability to accommodate to the bifurcation tortuosity [20]. Subsequently issues about stent deformation

⁵With respect to deployment mechanics, stents can be classified as: i) balloon-expanding (BX); ii) self-expanding (SX). BX stents are mounted on a balloon which is gradually inflated driving the stent deployment. SX stents are manufactured at the vessel diameter, then crimped and constrained in the delivery system; during the deployment the SX stent is gradually released from the catheter recovering the target diameter thanks to its mechanical properties [16].

were resolved by the use of self-expanding braided wirestent, i.e. Wallstent (Boston Scientific Co., Natick, MA, USA) and later by self-expanding Nitinol⁶ stents. The advantage of using such stents in the CA district is related to their ability to recover large deformations due to external loads and to the possibility to cover long stenosis using only one device. While the Wallstent is manufactured by braiding cobalt-chromium (CoCr) wires to make a tubular mesh, which behaves like a spring, most of the current Nitinol carotid stent designs are obtained through laser-cutting of low-profile tube and comprise of sequential aligned annular ring segments, interconnected in a helical fashion.

Despite such a technologic effort to improve the stent designs and their capability to adapt to the vessel tortuosity, the major concerns for this endovascular treatment were related to the intra/post-operative risk of embolism. A significant improvement with respect to this issue has been done thanks to treatment strategies focusing on neurological protection. In fact, embolic protection devices (EPD) were introduced in CAS procedure in order to capture and remove embolic debris generated during the intervention (see section 2.1).

With respect to carotid stent design, even a small difference in material, size, design and configuration can correspond to a notable difference with respect to its functional characteristics, which can be resumed as follows:

- foreshortening: difference between the length of the stent within the delivery system and after its deployment;
- conformability: stent ability to accomodate to vessel anatomical features such as tortuosity or change in the vessel cross-sectional profile;
- scaffolding: stent ability to cover and support the vessel wall and the plaque;

⁶Nitinol is Nickel-Titanium alloy and refers to a class of alloys denominated as shape memory alloys (SMA), sometimes even called “adaptive” or “smart”, which have the ability to return to an original shape when subjected to appropriate thermo-mechanical loads, thanks to their peculiar pseudo-elastic (PE) and shape-memory (SME) effects. Briefly, PE is the material ability to undergo large deformations without experiencing permanent deformations; in fact when the load is removed, the material recovers the original desired shape. On the other hand, SME is the material ability to recover apparent permanent deformations through a heating process. Both effects are related to the material intrinsic solid-solid phase transformations, driven by forces during PE and by thermo-mechanical loadings during SME.

- radial strength: it describes the external pressure that a stent is able to withstand without incurring clinically significant damage;
- radial stiffness: measure for the stent diameter reduction by the application of an external pressure.

The relation between these features and the stent design has been discussed by several experts [16, 20, 21] and quantitatively assessed in several ways [22, 23]. With the use of embolic protection devices, there is a shift from intra- to post-procedural complications [24] and thus to capability of a given stent design to avoid plaque protrusion through its cells. Consequently, it is reasonable to suppose that novel stent designs will be a trade-off of conformability and vessel scaffolding defining a sort of hybrid stent, having functional/mechanical features which vary along the “tailored” design [23]. In a very recent literature review aiming at explaining the poor results of CAS in symptomatic patients, Paraskevas and colleagues [11] suggest the following items as key factors to improve CAS outcomes:

- modification of vascular risk factors and pre- and post-CAS plaque stabilization;
- better patient selection;
- improved CAS skills/techniques;
- improved technology for CAS - better EPDs (flow reversal and proximal occlusion) and better stents (membrane-covered, ultra-closed cell, and biodegradable).

Current refinements of CAS technology are evolving steadily and are already following these indications; new delivery sheaths, guiding/access catheters, design improvements for EPDs, new stent materials and coatings are expected to emerge in close future. But it is necessary to underline that the future of CAS is still not decided as current indications for CAS can change depending on the results of ongoing and future trials; this aspect can dramatically influence the clinical interest for such procedure and consequently the investment of (bio)medical industries in CAS devices.

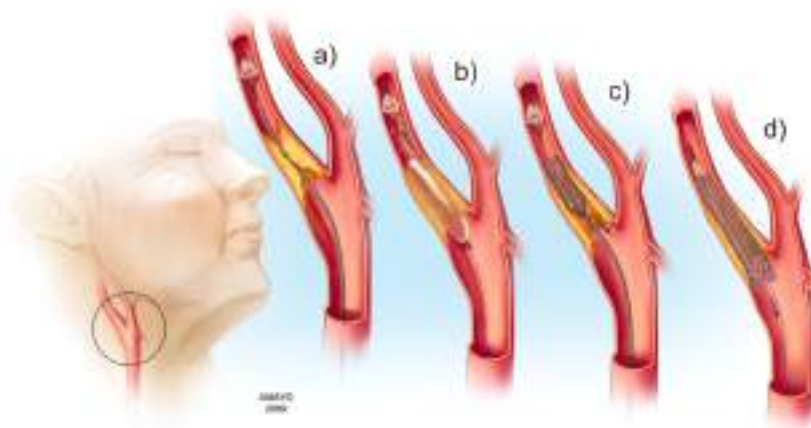


Figure 1.5: Carotid angioplasty and stenting. a) Guide catheter (not shown) is placed in the CCA proximal to the stenosis. Through this catheter, a filter wire is used to cross the stenosis and deploy an embolic protection filter (EPF) in the ICA distal to the plaque. The filter captures emboli dislodged during the procedure. b) pre-dilation of the plaque is performed with an angioplasty balloon, followed by c) stent deployment; occasionally, angioplasty may be necessary after stenting to further dilate residual stenosis. d) the filter is withdrawn into the guide catheter. The procedure is done with full heparinization. Patients receive maintenance dual antiplatelet therapy, usually aspirin plus clopidogrel, for at least 4 to 6 weeks. Adapted from [25].

1.4 Thesis rationale and organization

The research activities described in this dissertation are motivated by the previous discussion and are based on the following considerations:

- the widespread acceptance of CAS and its effectiveness compared to CEA is still a matter of debate [13];
- clinical experts underline that the success of CAS is strongly dependent on the operator ability/experience [14, 15, 26];
- different stent designs and EPDs with intrinsic different mechanical features [22, 23] are available in a growing dedicated market, this aspect, on the one hand, is enlarging the available interventional options but, on the other hand, is complicating the standardization of the treatment strategy;
- CAS outcomes are dependent on a proper selection of patients and devices [27];
- the dramatic technologic advancement in medical imaging allows nowadays an accurate assessment of the main vascular features [5, 28, 29];
- Finite Element Method (FEM) based simulations can be considered as a reliable tool to investigate the prosthesis/vessel interaction [30, 31].

Consequently, we exploit the use of numerical simulation to investigate different biomechanical aspects of CAS, ranging from the performance assessment of embolic protection filter to modeling of CA, but we mainly attempt to move a first step towards the application of numerical simulation of CAS to support the clinical practice. In fact, we investigate the feasibility to implement the work-flow depicted in figure 1.6, which represents a virtual framework aiming at evaluating the performance of different stent designs in a patient-specific CA model through finite element analysis - FEA (see Chapter 3).

In particular, the dissertation is organized as follows:

- Chapter 2: we investigate the role of filter design on its capability to adapt to the vessel wall;
- Chapter 3: we evaluate the impact of different stent designs on the revascularization of a single vessel anatomy in order to move a first

step towards a quantitative assessment of the relation between a given carotid stent design and a given patient-specific CA anatomy;

- Chapter 4: we analyze the impact of carotid stent apposition on CA wall stress distribution and in particular the influence of constitutive vessel wall modeling on the predicted tensional state over the CA wall;
- Chapter 5: we evaluate the influence of stent cell type (open versus closed) on vessel scaffolding in a realistic, experimentally-validated case.

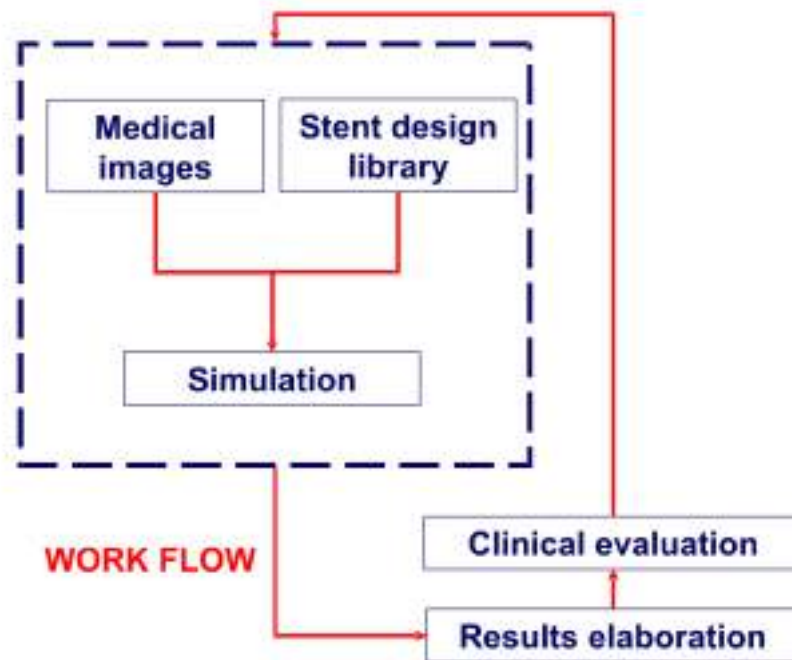


Figure 1.6: Work-flow of the virtual framework to assess the stent performance in a given patient-specific carotid artery anatomy: starting from medical images, we develop the patient-specific CA model; we combine the vessel model with a given stent model available within a predefined stent design library to perform a simulation of CAS through FEA; the results are elaborated to assess clinically relevant parameters of stenting performance (e.g. lumen gain or vessel straightening). The framework allows to investigate virtual scenarios and to perform an evaluation loop aiming at supporting the CAS procedure planning.

Chapter 2

Nitinol embolic protection filters: design investigation by finite element analysis

2.1 Introduction

Cardiovascular disease (CVD) is the main cause of death in Western countries. Each year CVD causes over 4.35 million deaths in Europe (accounting for 49% of all deaths in 2005)[32]. CVD is often related to atherosclerosis, a degeneration of the vessel wall which has the main consequence of narrowing the vessel lumen, i.e. a stenosis, leading to blood flow reduction or blockage.

At present, the deployment of an intravascular stent has become a common and widely used minimally invasive treatment for stenotic arteries, including mainly coronary arteries but also peripheral stenotic vessels such as the carotid arteries.

In recent years, carotid artery stenting (CAS) has emerged as a less invasive treatment as compared to the conventional surgical approach, carotid endarterectomy (CEA) [33], but the efficacy of CAS relative to surgery is still a matter of debate [34].

One major concern related to CAS is the possible distal embolization potentially leading to stroke or other severe neurological complications. Embolization is due mainly to the plaque debris and thrombi generated during

the stenosis dilatation and stent apposition. Consequently, embolic protection devices (EPDs) have been developed to capture such released debris and appear to have a significant impact on the success of CAS [35, 36, 37, 38, 39]. EPDs can be classified in the following three categories [40]:

- distal balloon occlusion;
- proximal balloon occlusion;
- embolic protection filters (EPFs).

The balloon occlusion systems block the flow in the internal carotid artery (ICA) and emboli are aspirated before balloon deflation and catheter removal, whereas EPFs maintain blood flow while emboli are captured.

Such a class of filters most often consists of a metallic basket-like structure coated with a membrane made of polymeric material containing numerous pores. Filters are usually mounted on a 0.014 in. (0.036 mm) guidewire, generally 30 mm proximal to a flexible tip and are delivered through a very small profile catheter (<3 French, i.e. 1 mm). During a CAS procedure, before the lesion dilatation and the stent apposition, the filter is opened in the ICA lumen distal to the target lesion, by withdrawing the delivery sheath. At the end of the CAS procedure, a retrieval catheter is advanced onto the guidewire to capture and remove the filter [41].

EPFs have both advantages and disadvantages with respect to balloon occlusion procedures. On one hand, EPFs have the advantage of preserving cerebral flow throughout the procedure while capturing embolic debris allowing distal perfusion and angiography during the CAS procedure. On the other hand, filters have disadvantages ranging from difficulty in navigating severely stenosed or tortuous vessels to possible incorrect filter apposition against the vessel wall [42, 43]. Currently, several embolic filter designs are available on a fast growing dedicated market [42].

Because of the relevant differences in EPF designs, it is likely that there are situations in which individual EPFs may be better suited to avoid adverse events during CAS and, consequently, the investigation and the comparison of the performance of different EPFs can play a key role in the improvement of filtering outcomes and potentially on the complete CAS procedure.

Engineering investigation and computer models have shown the capability to provide useful information to understand the mechanics of cardiovascular devices, e.g. stents, and to improve device design [44, 45, 46, 47]. To

the best of our knowledge, the available comparative investigations about advantages or roles that specific EPDs may have in CAS are mainly based on in vitro, ex vivo, or clinical studies [43, 23, 48, 49, 50].

The purpose of this study is to use finite element analysis (FEA) in the design evaluation of basket-like embolic protection filters. In particular, we investigated the effects of sizing on circumferential basket-vessel wall apposition of a widely adopted embolic filter, i.e. the Angioguard XP™ (Cordis Endovascular, FL, USA). In order to achieve this purpose, we organized the study as follows:

- Using a script-based procedure, we created a 3D finite element model of the Angioguard XP™ taking into account several geometrical features (such as number of struts, strut diameter, filter length, filter diameter, etc.).
- To validate the model, we qualitatively compared the numerical prediction of a free filter expansion, i.e. as it exits out of the delivery sheath, with a micro-CT scan image of the real device deployment.
- To evaluate the circumferential basket-vessel wall apposition, we simulated the deployment of a 4 mm size Angioguard XP™ in a vessel having different sizes and shape.

2.2 Materials and Methods

2.2.1 Model geometry

The Angioguard XP™ consists of a 0.014 in. (0.036 mm) guidewire with a Nitinol basket frame enveloped by a porous polymeric membrane (see figure 2.1). The current Angioguard XP™ basket sizes range from 4 to 8 mm in diameter in order to deploy within vessels with diameters ranging from 3.0 to 7.5 mm [42, 51].

We used the in-house developed pyFormex software (version 0.6.5) [52] as a pre-processing tool to build a geometrical and finite element model of the Angioguard XP™.

The model includes the following parts:

- filter struts defining the basket frame;
- membrane;

- markers.

The mesh generation procedure was defined by four essential steps (see figure 2.2):

- creation of path reproducing the shape of one filter strut;
- sweeping of planar section along the defined path in order to create one 3D filter strut;
- replication and rotation of the filter strut around the filter axis in order to create the whole basket frame;
- definition of the whole model assembling the filter struts with the membrane and markers.

From a geometrical point of view, the model is defined by several parameters as depicted in figure 2.2 and reported in table 2.1. The pyFormex script-based mesh generation procedure allows the creation of a finite element model in a quick way facilitating parametrical finite element analyses; moreover, pyFormex generates a finite element mesh that can be easily imported into several commercial finite element solvers. In this study, we used Abaqus/Explicit 6.8 (Abaqus Inc., Providence, RI). In order to assess accurately the value of the defined geometrical parameters, a micro-CT scan of a real device in open configuration was performed and the image was analyzed by Materialise miniMagics version 12.0.5.1 (see table 2.1).

Material properties

The filter struts defining the basket frame are manufactured from Nitinol, a nickel-titanium-based alloy showing the so-called superelastic effect (SE). A typical superelastic Nitinol behavior is shown in figure 2.3 illustrating the ability to undergo large deformations (up to 6-8%) during loading and to fully recover such deformations during unloading. Clearly, the filter exploits this superelastic effect during both the delivery and retrieval phase, allowing the device to switch from a closed configuration to an open configuration and vice versa without experiencing plastic deformation.

In our simulations, Nitinol superelasticity is modeled as a predefined user material in the Abaqus/Explicit 6.8 solver.

The polymeric porous membrane covering the filter frame was assumed to be manufactured in a Nylon-based material and having 0.02 mm thickness

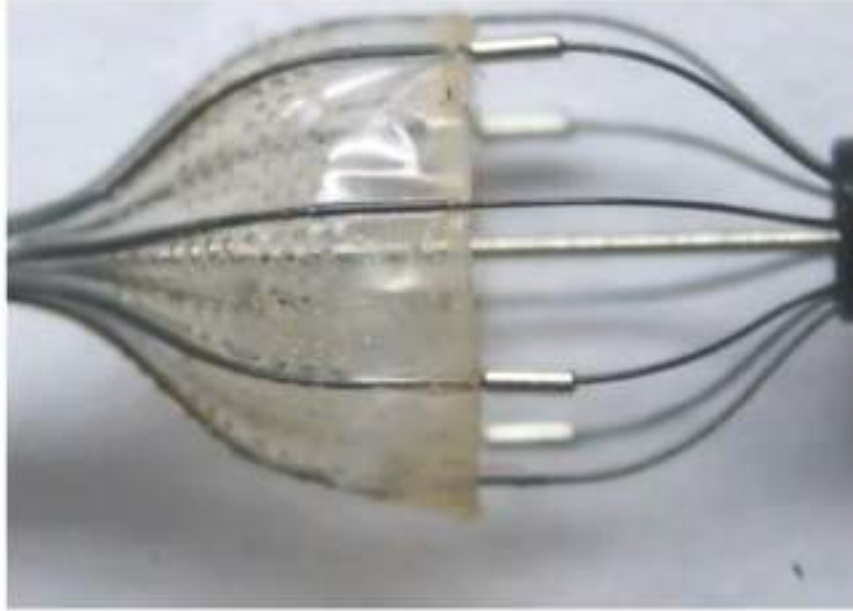


Figure 2.1: The Angioguard XP™ embolic protection device.

Table 2.1: Geometrical parameters of 4.0 mm filter model.

Symbol	Description	Value
N_{struts}	Number of struts	8
R_{axis}	Distance of strut centerline from filter axis	0.3 mm
R_1	Filter radius (part 1)	0.68 mm
R_2	Filter radius (part 2)	1.02 mm
$R_{strut} = (R_{axis} + R_1 + R_2)$	Filter radius	2 mm
L_1	Filter length (part 1)	1.49 mm
L_2	Filter length (part 2)	2.76 mm
$L_{strut} = 2 * (L_1 + L_2)$	Filter length	8.5 mm
D_{strut}	Strut diameter	0.08 mm
$Membrane_{coverage}$	Percentage of filter coverage	50%
$Membrane_{th}$	Membrane thickness	0.02 mm
L_{marker}	Marker length	0.8 mm
D_{marker}	Marker diameter	0.22 mm

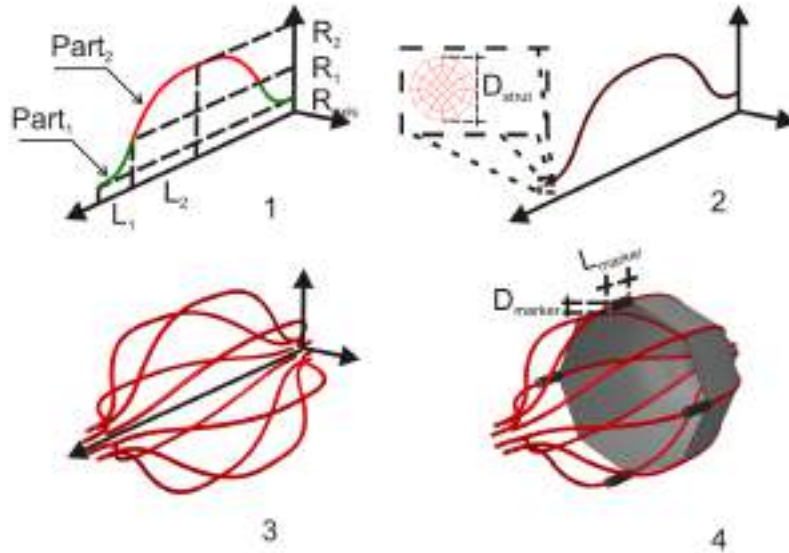


Figure 2.2: Example of filter model generation in four steps.

[45]. The holes in the membrane were neglected.

The markers, attached to the Nitinol frame to enhance filter radiopacity, were assumed to be manufactured by pure tantalum [54].

Table 2.2 reports the adopted material properties employed in the simulations.

2.2.2 Filter free expansion

To validate the developed finite element model, we simulate the filter-free expansion, i.e. as it exits out of the delivery sheath.

Consequently, the numerical analysis of this free expansion of filter is a non-linear problem involving large deformation and contact problems in the numerical analysis. For this purpose, large deformation analyses were performed using the Abaqus/Explicit solver, particularly quasi-static procedures were used assuming that inertia forces do not dominate/change the analysis. Kinetic energy was monitored to ensure that the ratio of kinetic energy to internal energy remains less than 10%. Moreover, a mass scaling

Table 2.2: Material properties used in the simulations.

Nitinol [53]		
E_A	Austenite Young's modulus	35877 MPa
ν_A	Austenite Poisson's ratio	0.33
E_M	Martensite Young's modulus	24462 MPa
ν_M	Martensite Poisson's ratio	0.33
ϵ^L	Transformation strain	0.0555
$\frac{d\sigma}{dT}_L$	Loading temperature derivative of stress	0 MPa/C°
σ_L^S	Loading start of transformation stress	489 MPa
σ_L^E	Loading end of transformation stress	572 MPa
T_0	Temperature	22 C°
$\frac{d\sigma}{dT}_U$	Unloading temperature derivative of stress	0 MPa/C°
σ_U^S	Unloading start of transformation stress	230 MPa
σ_U^E	Unloading end of transformation stress	147 MPa
ρ_{strut}	density ¹	6.5 g/cm ³
Nylon [45]		
E_{membr}	Modulus of elasticity	920 MPa
ν_{membr}	Poisson'ratio	0.4
ρ_{membr}	Density	1.1 g/cm ³
Tantalum [54]		
E_{marker}	Modulus of elasticity	179000 MPa
ν_{marker}	Poisson'ratio	0.35
ρ_{marker}	Density	16.6 g/cm ³

strategy was used to reduce computational cost. All finite element simulations were carried out on an in-house built low-cost, high-performance computing cluster [55].

The delivery sheath was assumed to be a straight rigid cylinder having a diameter equal to 1.06 mm and a length of 15 mm.

The parts defining filter/catheter systems (see figure 2.4) were modelled as follows:

- filter struts: 33,792 three-dimensional 8-node brick reduced-integration elements (C3D8R);
- membrane: 8320 three-dimensional 4-node quadrilateral membrane

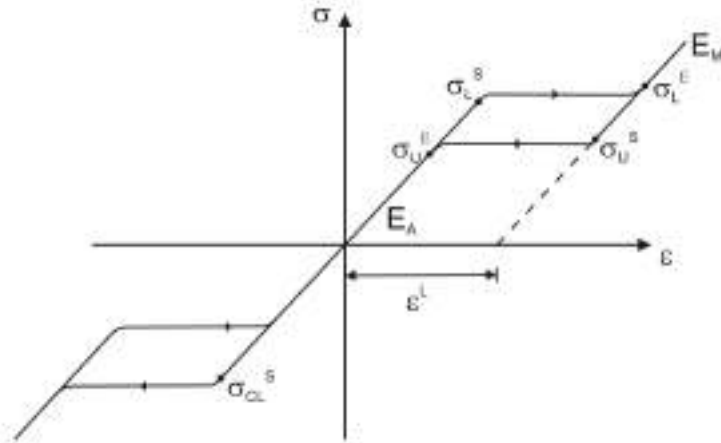


Figure 2.3: Typical superelastic nitinol behavior

elements with reduced integration (M3D4R);

- markers: 1296 three-dimensional 8-node brick reduced integration elements (C3D8R);
- catheter: 3806 three-dimensional 4-node bilinear quadrilateral rigid elements (R3D4).

Mesh tie constraints of type surface-to-surface were applied to tie the markers and the membrane to the filter struts. Furthermore, the filter frame struts are tied to marker bands defining the relative movement of the filter ends with respect to the guidewire [51], particularly the proximal marker band is fixed to the guidewire while the distal marker band is free to slip along the guidewire. Therefore, mesh tie constraints, type rigid body, are imposed between the nodes lying on each filter frame end and the predefined reference points. Boundary conditions are then applied to the reference points (RPs) to realistically simulate the movement of the marker bands. In particular, at the proximal end RP, all the degrees of freedom

were constrained; at the distal end RP, only displacement along filter axis and rotations were allowed. The analysis strategy assumes that the filter frame deformation during deployment is comparable to the deformation during the filter frame insertion into the delivery sheath. Consequently, a progressive rigid translation along the filter axis is imposed to the delivery sheath in order to induce the necessary filter deformation to switch from the open configuration (filter out of delivery sheath) to the closed configuration (filter within the delivery sheath).

A frictionless general contact algorithm has been used in order to handle the interactions between the filter frame and the deployment sheath. In this case, the membrane elements were excluded from the contact strategy in order to simplify the simulations assuming that it has a minor role in the overall filter deployment/retrieval mechanics.

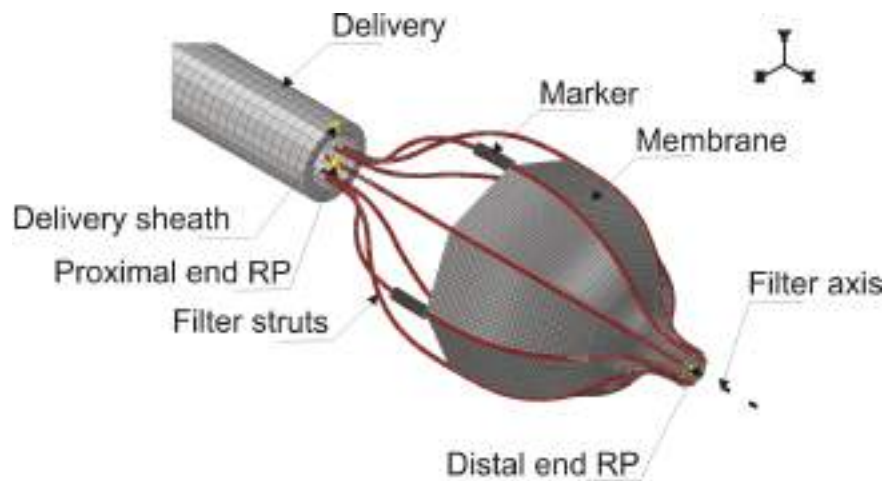


Figure 2.4: Finite element model of Angioguard XP™ and part of the delivery sheath

2.2.3 Circumferential basket-vessel wall apposition

In order to evaluate the circumferential basket-vessel wall apposition, we carried out the simulations of a filter deploying in a straight vessel modeled as a rigid cylinder having different sizes and shape. In particular, two

different scenarios were investigated: (i) filter expansion in three circular vessels having respectively 3.0, 3.25, and 3.5 mm diameter as suggested by the manufacturer for a 4 mm size filter [51]; (ii) filter expansion in two oval vessels having both 1.5 mm major semi axis and respectively an ovality² of 0.85 and 0.75.

Preliminary simulations showed that, in the analyzed case, final filter/vessel configuration is not influenced by the deploying mode and consequently the interaction between filter and sheath has not been taken into account.

We defined a two-step simulation strategy as follows: (i) filter diameter reduction is obtained by elongating the basket frame by appropriate axial displacement boundary conditions to the distal end RP, only self contact of membrane was included in this step; (ii) previous boundary conditions are deactivated allowing the filter re-expansion and a global contact algorithm was included allowing the filter/vessel interaction.

The effect of blood flow pressure acting on the filter membrane was included in the analyses applying a uniform pressure of 8.80 mmHg on the inner surface of the membrane [56].

Circumferential basket-vessel wall apposition was evaluated in terms of gap between the vessel lumen and the circumferential area covered by the filter. In order to keep the computational cost acceptable and to minimize the impact of the membrane mesh on the gap measurement, a final membrane mesh of M3D4R 24960 elements was chosen by a preliminary mesh sensibility analysis about filter deployment simulation in the 3 mm circular vessel (a finer membrane mesh - 29.120 elements - results in a 5.4% gap measurement differing 6% compared to the 5.7% gap obtained with the coarser mesh - 24.960 elements).

²Ovality being defined as the change in cross section roundness and defined as $O = b/a$, where a is cross section semi-major axis length and b is cross section semi-minor axis length.

2.3 Results

2.3.1 Filter free expansion

The simulation of the filter-free expansion showed that the basket-frame configuration experiences a severe change. The radial compression of the filter frame is accomplished by an axial elongation bringing the diameter to a final value of 0.96 mm when the filter is completely inserted into the sheath as shown in figure 2.5. Moreover, the filter frame experiences a radial deformation that is not uniform along the filter length, resulting in non-uniform adhesion between the strut and the delivery sheath wall.

Comparing the previously described adopted mesh to a finer one (i.e. 67.584, 33.024, and 2.592 elements respectively for filter struts, membrane, and markers) showed a negligible divergence (i.e. difference in maximum axial elongation less than 1%).

Moreover, figure 2.6 shows a good qualitative agreement between the numerical results and the micro-CT image of the partially deployed Angioguard XP™.

2.3.2 Circumferential basket-vessel wall apposition

Simulations of the filter deployment in the straight vessel showed that the filter is not able to completely cover the vessel lumen and gaps are present between the vessel wall and the membrane (see figure 2.7), confirming the experimental results recently reported by Siewiorek et al. [57].

As reported in table 2.3, the vessel size seems to have a minor impact on the circumferential basket-vessel wall apposition which is in contrast to the impact of the vessel shape. In fact, an increase in the vessel ovality dramatically influences the gap while a change in the vessel diameter does not significantly modify the gap area.

Consequently, the simulations of filter deployment in the straight rigid vessel suggest that, in this case, filter malapposition is caused by inability of the filter struts to accomplish the vessel asymmetry.

Table 2.3: Numerical results of filter/vessel wall apposition.

Filter size [mm] - Ovality	3.5 - 0.0	3.25 - 0.0	3.0 - 0.0	3.0 - 0.85	3.0 - 0.75
Gap (% of vessel lumen)	5.7	4.7	5.7	8.7	14.7

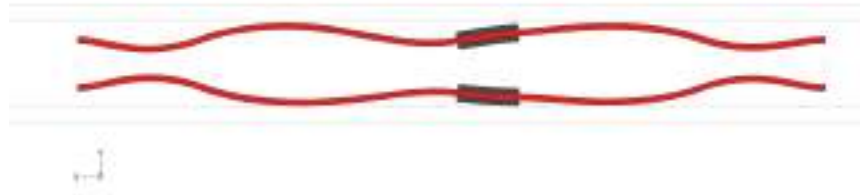


Figure 2.5: Longitudinal cut view of the filter frame in the delivery sheath



Figure 2.6: Partially deployed filter: micro-CT image (top panel); numerical simulation (bottom panel).

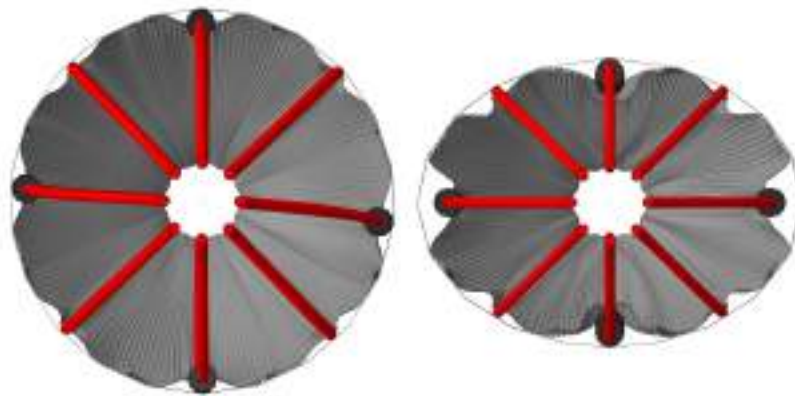


Figure 2.7: A 4 mm size filter deployed in a 3 mm circular vessel (on the left) and in 3 mm vessel having 0.75 ovality (on the right).

2.4 Limitations

The filter-free expansion simulation showed qualitative agreement with micro-CT images but limitations pertaining to the frictionless contact between the filter and the delivery sheath are present.

Clearly, the assumption of a uniform pressure distribution along the filter membrane should be improved using more accurate and realistic values achieved, for example, by experiments and computational fluid dynamics analyses.

Material properties of the filter components should also be derived from experimental data to define the mechanical properties more accurately. The major limitation of this study is the rigid body assumption for the vessel. In reality, the radial outward force of the filter is likely to reshape the vessel and this effect can consequently influence the filter-vessel wall apposition. However, modeling filter apposition in a realistic vessel (i.e. internal carotid artery) introduces substantial computational challenges, such as the incorporation of the variability of the constitution and mechanical properties of the diseased arterial wall, and should be accomplished by adequate experimental validation. This challenge is considered to be beyond the scope of this preliminary investigation.

2.5 Conclusions

In this study, we proposed and validated a finite element model in order to investigate the basket-like design of an embolic protection filter device. In particular, the circumferential filter/vessel wall apposition was numerically evaluated confirming the inability of the filter to completely adapt to asymmetric vessels. Clearly, this study needs to be considered as a preliminary proof of concept of the use of finite element based modeling strategies to investigate and understand the mechanics of embolic protection filters. The proposed model is a base to further investigate the impact of design parameters (filter length, diameter, number of struts, etc.) on filter mechanics (flexibility, radial strength, etc.) and the filter apposition in a more realistic tortuous anatomy taking also into account vessel wall material properties. Finally, we conclude that the proposed methodology could be useful to evaluate and to compare current or new EPDs in the early design phase as recently recommended by the FDA [58].

Chapter 3

Carotid artery stenting: from medical images to finite element analysis

3.1 Introduction

Atherosclerotic stenosis of the carotid artery (CA), narrowing the bifurcation neck, causes 20% of all ischemic strokes and transient ischemic attacks [59, 60].

Carotid endarterectomy (CEA) is considered the gold standard for severe CA stenosis [61] but carotid artery stenting (CAS) has emerged as a safe and cost-effective alternative to CEA [62, 63, 64]. However, the widespread acceptance of CAS and its effectiveness compared to CEA is still a matter of debate, especially in case of symptomatic patients [11].

The clinical experts underline that the success of CAS is strongly dependent on the operator ability and should be supported by a proper selection of patients and devices [15]. Many dedicated CAS devices (e.g. stents, embolic protection devices (EPDs), guidewires, etc.) are available on a rapidly growing market which, on the one hand, is enlarging the available interventional options but, on the other hand, is complicating the standardization of the treatment strategy. Moreover, it is evident that CAS outcomes are essentially related to anatomic considerations [27].

These aspects indicate a significant need to develop dedicated tools for both

procedure planning and device selection in order to relate the device features with the target vascular anatomy.

Although computational tools, as Finite Element Analysis (FEA), are largely used to investigate several aspects of coronary stenting, such as the evaluation of interventional technique options [65] or the impact of plaque composition on vessel wall stress [66], few FEA studies are available on CAS [67, 68, 69]. In the present study, we use FEA to evaluate the performance of three self-expandable¹ stent designs in the CA. The study is organized as follows:

- we generate a patient-specific CA model based on DICOM images of Computed Tomography Angiography (CTA);
- we generate six stent models considering three stent designs (laser-cut open-cell, laser-cut closed-cell, braided closed-cell) in different sizes and configurations (i.e. straight and tapered²);
- for each stent model, we simulate the deployment in the CA model;
- we analyze the simulation results with respect to vessel stress, comparing also the pre- and post-stenting vessel geometry to evaluate the lumen gain and vessel straightening.

¹With respect to deployment mechanics, stents can be classified as: i) balloon-expanding (BX) and ii) self-expanding (SX). BX stents are mounted on a balloon which is gradually inflated driving the stent deployment. SX stents are manufactured at the vessel diameter, then crimped and constrained in the delivery system; during the deployment the SX stent is gradually released from the catheter recovering the target diameter thanks to its mechanical properties [16].

²The distal diameter is smaller than the proximal one in order to set a conical shape to better take into account the diameter difference between the common carotid artery (CCA) and the internal carotid artery (ICA).

3.2 Materials and Methods

Although CAS is a complex procedure which takes place in several steps, we focus on the stent implantation therefore the following parts are included in the simulations:

- a patient-specific CA model;
- the stent;
- the catheter.

The numerical analysis is clearly non-linear, involving large deformation and contact; consequently we use Abaqus/Explicit as finite element solver (see section 3.2.3).

In the following we describe the generation of the CA model, the generation of the stent models, the FEA settings and the post-processing of the numerical results.

3.2.1 Patient-specific carotid artery model

We process the DICOM CTA images of a stenosed carotid bifurcation of a 83 years-old male patient using Mimics v.13 (Materialise, Leuven, Belgium) to: i) select the region of interest; ii) compute the vessel centerline; iii) remove secondary branches; iv) generate an STL file defining the lumen profile (see figure 3.1-a).

We use the open-source software pyFormex v.0.8 [52] to elaborate the obtained STL file to: i) analyze the lumen of common carotid artery (CCA), external carotid artery (ECA) and internal carotid artery (ICA) (see figure 3.1-b and table 3.1); ii) reconstruct the CA outer profile (see figure 3.1-c); iii) generate a high-quality, full hexahedral mesh with balanced resolution in each branch and minimal distortion for each element [70, 71] (see figure 3.1-d).

Since the medical images contain no information on the vessel wall thickness, we adopt a reconstruction strategy considering the wall thickness as a percentage (i.e., 30%) of the vessel radius in the non-diseased region as suggested by values reported by Sommer et al. [72]. At the location of the stenosis, we reconstruct the outer wall interpolating the profile of the distal and proximal region by means of Bezier splines.

The vessel tissue is modeled as an isotropic hyperelastic material as proposed by Lally et al. [46, 73]; despite the material parameters are calibrated on experimental data on human femoral artery and not on human CA, we believe that this model is appropriate for the purpose of the present study since it was successfully used for similar numerical analyses and based on accurate uni- and bi-axial tests on several tissue samples. The vessel density is assumed to be 1 g/cm^3 .

After a mesh sensitivity analysis (see Appendix 3.6.1), we choose a final vessel mesh of 12960 8-node linear brick, reduced integration elements with hourglass control (C3D8R).

We define ad hoc local cylindrical coordinate systems at the vessel ends to fix the corresponding nodes in the longitudinal and in the circumferential direction allowing consequently only radial displacements. Moreover, we assume no internal pressure on the vessel wall under the hypothesis that the geometry is based on measurements achieved at 80 mmHg.

Table 3.1: Geometrical measures of the branch sections highlighted in figure 3.1.

Branch	Sections	Mean radius \pm std [mm]	Area [mm^2]
CCA	1	3.67 ± 0.12	41.56
	2	3.39 ± 0.08	35.52
	3	3.37 ± 0.39	33.62
ECA	1	2.11 ± 0.24	13.37
	2	2.19 ± 0.13	14.77
	3	2.14 ± 0.04	14.14
ICA	1	2.43 ± 0.27	17.71
	2	2.75 ± 0.26	23.24
	3	2.66 ± 0.17	21.91

3.2.2 Stent models

We consider three self-expanding stent designs: laser-cut open-cell, laser-cut closed-cell, braided closed-cell labeled, respectively indicated in the following as *A, B, C* and resembling three commercially-available devices: the ACCULINK and the XACT (Abbott, Illinois, USA); the Wallstent (Boston Scientific Co., Natick, MA, USA).

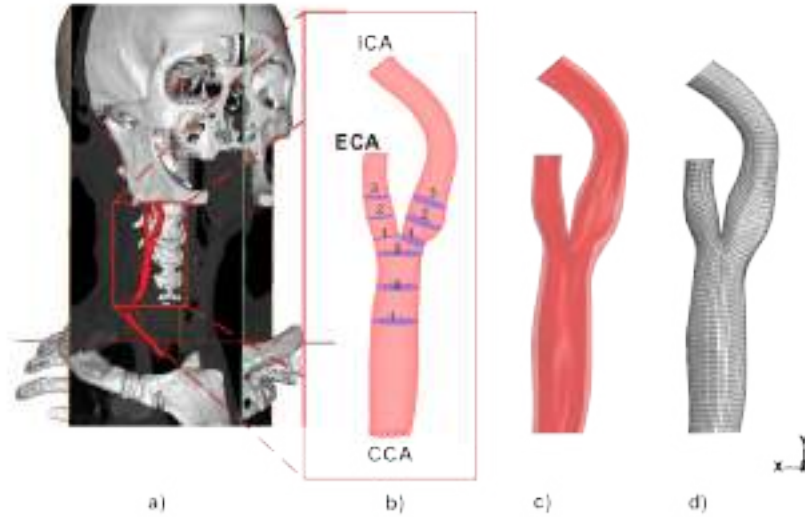


Figure 3.1: Patient-specific CA model: a) 3D reconstruction of cerebral vascular tree from CTA; b) lumen of CA main branches (CCA: common carotid artery; ICA: internal carotid artery; ECA: external carotid artery) with the related analyzed sections; c) CA lumen (dark red) and reconstructed outer vessel wall profile (light red); d) hexahedral mesh.

We define six stent models from the three designs as described in the following: the first two designs are considered both in a straight configuration (labeled as stent *A1* and *B1*) and in a tapered configuration (labeled as stent *A2* and *B2*); only one model (stent *C1*) of design *C* is considered since it is self-tapering; the sixth model (stent *B3*) is obtained oversizing stent *B2*. In figure 3.2, the stent models *A1*, *B1* and *C1* are depicted to highlight the three different designs under investigation, in their zero-stress state, while the details about size, configuration, number of nodes, number of elements for each model are reported in table 3.2. We assume the same thickness of 0.24 mm for both designs *A* and *B* in order to focus the comparison mainly on the design features and not on the specific commercial device.

In the braided closed-cell stent (model *C*), connectors elements (type JOIN)

are introduced at the positions where there is physical contact between the crossing wires, in order to model the contact between these wires. The wire sliding is not allowed as each connector restrains the relative displacement between the tied nodes but allows the relative rotation [74, 75].

While designs *A* and *B* are assumed to be manufactured in Nitinol, design *C* is assumed to be made in high strength Phynox, a cobalt-chromium alloy. The superelastic behavior of Nitinol is modeled using the Abaqus user material subroutine [76] originally proposed by Auricchio and Taylor [77, 78] and based on the concept of generalized plasticity [79]. The adopted Nitinol constitutive parameters are obtained from literature [80] and considered identical for all stents; the density is assumed to be 6.7 g/cm^3 . Phynox is modeled as an elasto-plastic material having an elastic modulus of 206000 MPa, Poisson’s ratio of 0.33 and yield strength of 2450 MPa [81].

Table 3.2: Geometrical and numerical details of the considered stent models.

Stent label	<i>A1</i>	<i>A2</i>	<i>B1</i>	<i>B2</i>	<i>B3</i>	<i>C1</i>
Configuration	Straight	Tapered	Straight	Tapered	Tapered	Self-tapering
Cell type	open-cell	open-cell	closed-cell	closed-cell	closed-cell	closed-cell
Manufacturing	laser-cut	laser-cut	laser-cut	laser-cut	laser-cut	braided
Outer diameter [mm]	8	8-6	8	8-6	9-7	8
Strut thickness [mm]	0.24	0.24	0.24	0.24	0.24	0.12
Initial Length [mm]	30	30	30	30	30	21
Number of nodes	159230	159230	171720	171720	171720	7705
Number of elements	85053	85053	93024	93024	93024	7680
Element type	C3D8R	C3D8R	C3D8R	C3D8R	C3D8R	B31
Material	Nitinol	Nitinol	Nitinol	Nitinol	Nitinol	Phynox

3.2.3 Finite element analysis of carotid artery stenting

The catheter is modeled as a rigid body defined by a surface obtained by sweeping a cylindrical section along the centerline of the vessel; we mesh it with 2760 three-dimensional, 4-node surface elements with reduced integration (SFM3D4R). In our simulation strategy, the stent deformation is imposed by the configuration change of the catheter, imposed by displacement boundary conditions (BCs) on its nodes; the BCs are determined as the difference between a starting and final catheter configuration for each simulation step. In particular the simulation consists of two steps:

1. stent crimping and bending: starting from a straight configuration

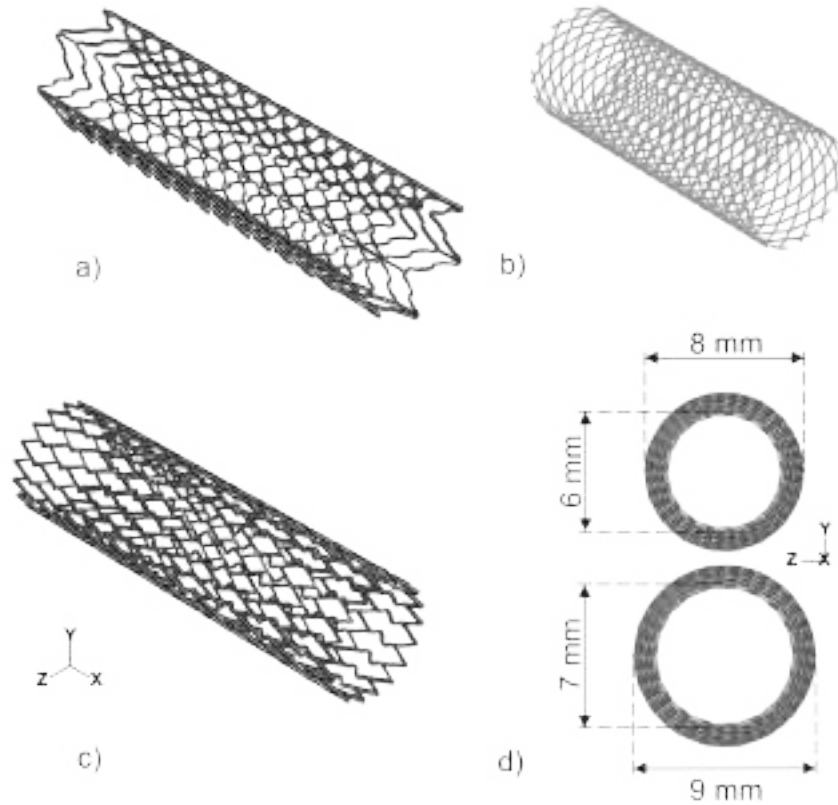


Figure 3.2: Stent designs under investigation: a) Design A (straight configuration): laser-cut open-cell; b) Design C: braided closed-cell; c) Design B (straight configuration): laser-cut closed-cell; d) Design B (tapered configuration): model B2 (8-6 mm) and the oversized version model B2 (9-7 mm).

the catheter is gradually bent and crimped accomplishing the vessel centerline and leading to the stent deformation; the contact between the stent and the vessel is deactivated in this step;

2. stent deployment: from the bent and crimped configuration, the catheter is re-enlarged and consequently the stent expands against the vessel wall; the contact between the stent and the vessel is activated in this

step.

Figure 3.4 depicts the whole finite element model configuration during the simulation. The numerical analysis is clearly non-linear, involving large deformations and contact; consequently we use Abaqus/Explicit as finite element solver since this code provides a stable general contact algorithm. We use a mass scaling strategy to increase the minimum stable time increment, reducing the computational cost but, at the same time, we monitor the kinetic energy of all components during the simulation, since we consider the stent deployment as a quasi-static phenomenon where inertial forces are negligible (see Appendix 3.6.2).

We use a general contact algorithm in order to handle the interactions between the parts: in particular, we set a frictionless contact between the stent and the catheter and a friction of 0.05 between the stent and the vessel surface [69].

3.2.4 Post-processing

We evaluate the impact of each stent model in the considered vessel focusing on the following aspects:

- von Mises stress distribution in the post-stenting vessel as a measure of potential injury induced by the stent apposition to the vessel wall. In fact, the supraphysiological stress state and the related vessel injury induced by the stent are important contributors for the complex process of restenosis [82]; consequently, the ideal stent should scaffold the vessel wall minimizing the induced stress;
- comparison of the pre- and post-stenting minimum lumen of the ICA as a measure of the lumen gain and of the stent capability to re-enlarge the stenosis;
- computation and comparison between the pre- and post-stenting vessel tortuosity as a measure of the vessel straightening induced by the stent insertion.

To neglect peak values of von Mises stress, due to local concentration, we consider the 99 percentile with respect to the pre-stenting vessel volume (i.e. only 1% of the volume has stress above this value). The pre- and post-stenting vessel tortuosity is measured as proposed by Thomas et al.

[83] (see figure 3.3). The lumen calculation is performed using pyFormex and based on the inner surface of the vessel.



Figure 3.3: Example of tortuosity computation (pre-stenting vessel): given the centerline, we quantify the vessel tortuosity computing the measure $(L/D-1)$ for the stented common carotid artery (CCA) and internal carotid artery (ICA) segment: L is the length of the centerline from the origin (point A) to the end of the stented region (point B) and D is the Euclidean distance between the two points; the tortuosity is therefore defined as the fractional increase in length of the tortuous vessel relative to a perfectly straight vessel.

3.3 Results

Figure 3.4 illustrates the vessel, stent and catheter configuration during the CAS simulation for stent *A1* while figure 3.5 depicts the final stent-vessel configuration for stent model *A1*, *B1* and *C1*, allowing the qualitative evaluation of the stent apposition with respect to the three designs. All the analyzed models are not able to fully adapt to the lumen profile as highlighted by the gap between the stent and vessel at the beginning of the ICA bulb (slightly above the bifurcation); in case of stent *A1*, the simulation reproduces the so-called *fish scaling*³ effect [20] of the open-cell design *A*.

3.3.1 von Mises stress in the post-stenting vessel wall

Figures 3.6 indicates that the maximum values of von Mises stress in the vessel wall are located near the bifurcation apex in all analyzed cases; this effect is related to the position of the stenosis which is also located at the beginning of the ICA bulb. The histograms depicted in figure 3.7 and the values reported in table 3.3 indicate that:

- design *A* induces the lowest level of stress;
- design *B* induces the highest level of stress;
- the stress induced by braided closed-cell stent (*C1*) is similar to the stress induced by the tapered configuration of the laser-cut closed-cell design (*B2*);
- for both designs *A* and *B*, the stress induced by the straight configuration is higher than the stress induced by the tapered configuration (stent *A1* versus stent *A2*, +63%; stent *B1* versus stent *B2*, +61%);
- in case of oversizing, i.e. stent *B3* versus stent *B2*, the stress increases by 52%.

3.3.2 Lumen gain

The histograms depicted in figure 3.8 (on the right) and the values reported in table 3.4 indicate that:

³When stent cells open on the concave surface of an angulated carotid bifurcation, they are prone to having prolapse and fish scaling on the open surface potentially resulting in intimal disruption.

- all the stents provide a high ICA lumen gain (>45%) corresponding to a small reduction of the ECA lumen;
- for both designs *A* and *B*, the lumen gain provided by the straight configuration is higher than the lumen gain provided by the tapered configuration (stent *A1* versus stent *A2* +10%; stent *B1* versus stent *B2*, +15%);
- in case of oversizing, i.e. stent *B3* versus stent *B2*, the lumen gain increases by 15%.

3.3.3 Pre- and post-stenting tortuosity

The histograms depicted in figure 3.8 (on the left) and the values reported in table 3.5 indicate that:

- all the stents straighten the vessel, reducing considerably the original stent tortuosity;
- stent design, configuration and size have a limited impact on the vessel straightening.

Table 3.3: Von Mises stress (99 percentile) for each stent model at the end of the simulation.

Stent Model	<i>A1</i>	<i>A2</i>	<i>B1</i>	<i>B2</i>	<i>B3</i>	<i>C1</i>
von Mises stress [MPa]	0.1533	0.0940	0.3090	0.1916	0.2924	0.2048

Table 3.4: Pre- and Post-stenting branch lumen and tortuosity.

Stent Model	Pre-stenting	Post-Stenting					
		<i>A1</i>	<i>A2</i>	<i>B1</i>	<i>B2</i>	<i>B3</i>	<i>C1</i>
ICA lumen [mm^2]	18.0	28.3	26.4	32.9	30.1	32.8	32.73
ICA gain [%]	–	57.1	46.5	82.7	67.0	82.3	81.8
ECA lumen [mm^2]	13.6	12.3	12.4	11.4	11.8	11.3	13.11
Tortuosity	0.029	0.014	0.013	0.013	0.011	0.010	0.010

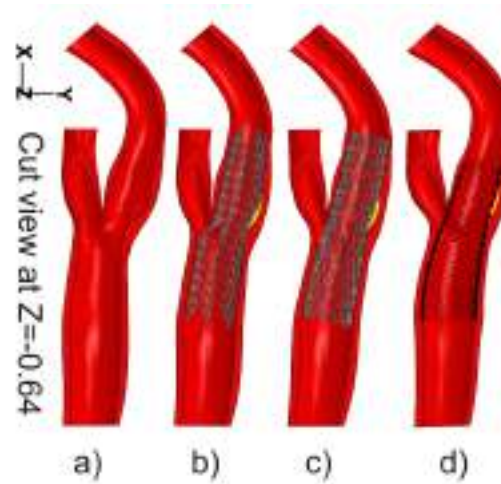


Figure 3.5: a) Pre-stenting carotid artery; Post-stenting carotid artery with b) stent A1, c) stent B1 and d) stent C1. The gap between the stent and the vessel is highlighted in yellow.

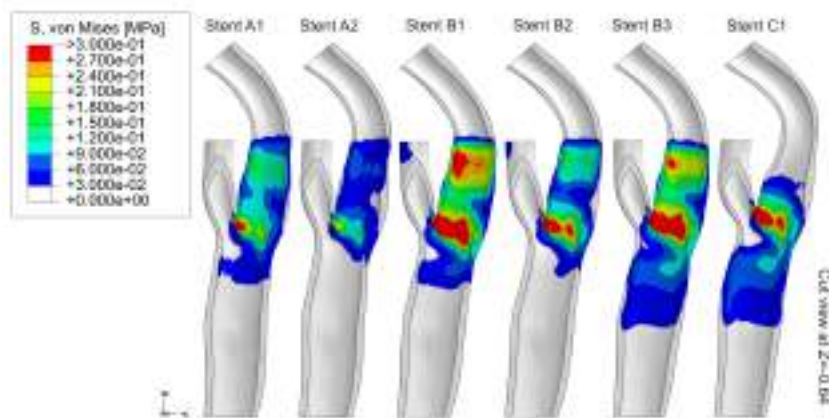


Figure 3.6: Contour plot of von Mises stress distribution (S, von MISES) in the post-stenting carotid artery with respect to the different stent models.

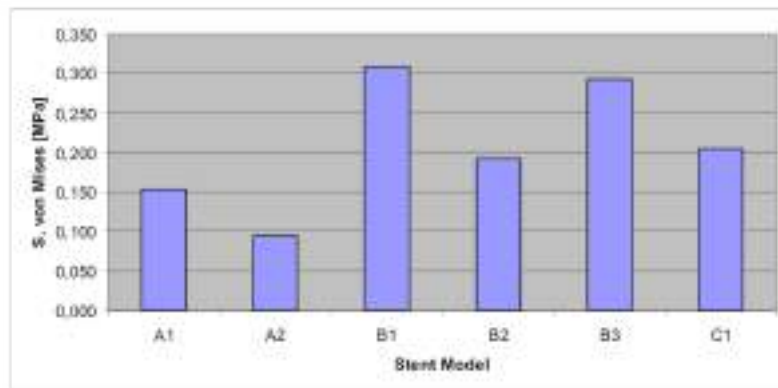


Figure 3.7: 99 percentile of von Mises stress (S, von MISES) in the post-stenting carotid artery with respect to different stent models.

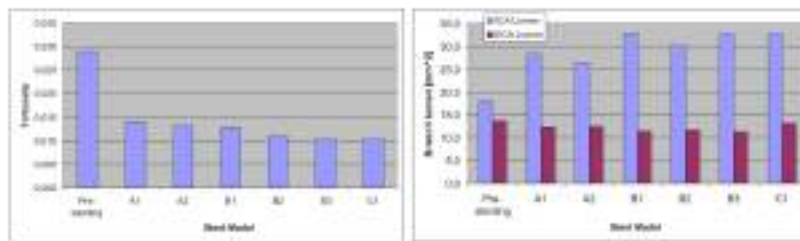


Figure 3.8: Pre- and post-stenting tortuosity (on the left) and lumen of internal carotid artery (ICA) and external carotid artery (ECA) (on the right).

3.4 Limitations

We developed the CA model from *in-vivo* CTA images discarding a distinction of the plaque from the surrounding tissue, which would have an effect on the stress distribution in the vessel wall, lumen gain and degree of straightening; however, we believe that the comparative nature of this study makes the obtained results still valid. In future work, we plan to further improve the model including the plaque components (i.e. calcifications, fibrous tissue, or lipid core) assessed by *in-vivo* CTA [84, 85] as proposed by a recent study [86]. Based on the NASCET method [87], the stenosis corresponds to a relative small vessel area reduction, i.e. 24%, which has no clinical indication for stenting [9]; future consideration of more severe degrees of stenosis would enforce the link between the presented simulations and the clinical practice.

We adopted an isotropic hyperelastic model for the vascular tissue as proposed by Lally et al. [46, 73] who calibrated the material parameters on experimental data on human femoral artery; we believe that this model is appropriate for the purpose of the present study since it was successfully used for similar numerical analyses and based on accurate uni- and bi-axial tests on several tissue samples. Moreover, although some studies [88, 89, 90] provide already experimental data on human carotid artery, only recently Sommer et al. [72] have systematically determined the biomechanical behaviour of human CCAs and ICAs; consequently we will use these data for further developments of the present study addressing anisotropic mechanical response of the CA tissue. Furthermore, we currently neglect axial pre-stretch, residual stresses and arterial blood pressure.

3.5 Conclusions

In the present study, we use FEA to evaluate the performance of three self-expandable stent designs, with different configurations and sizes, in a patient-specific CA model based on computed angiography tomography (CTA) images. We consider the stress induced to the vessel wall, the lumen gain and the vessel straightening as measures of stenting impact on the vessel anatomy.

For the considered vascular anatomy and stents, the results suggest that: i) the laser-cut closed-cell design provides a higher lumen gain; ii) the impact of the stent configuration and of stent oversizing is negligible with respect to lumen gain and relevant with respect to the stress induced to the vessel wall; iii) stent design, configuration and size have a limited impact on the vessel straightening.

Although the proposed numerical results refer to one specific vascular anatomy and three stent designs, we believe that the present study represents a first step towards a quantitative assessment of the relation between the complex mechanical features of a given carotid stent design and a given patient-specific CA anatomy, which could be useful for the procedure standardization. Clearly, due to the complexity of the system under investigation, the numerical results should be validated and embedded in a broader process accounting for clinical and biological considerations where the surgeon experience has a primary role.

3.6 Appendix

3.6.1 Mesh convergence analysis

We performed a mesh convergence analysis for the CA model discretization comparing the results of three different simulations (with three different vessel meshes) of CAS implant using stent *B2* (see table 3.5). We run all the simulation on 8 2.40 GHz cpus [55]. We focus on the following outputs obtained at the end of the simulation:

- displacement magnitude: we consider the maximum value - U MAGNITUDE (MAX) - in the vessel node set;
- von Mises stress: we consider both the maximum value - MISES (MAX) - in the vessel element set and 99 percentile - MISES (99PERC) - with respect to the pre-stenting vessel volume;
- maximum principal logarithmic strain: we consider both maximum value - MISES (MAX) - in the vessel element set and 99 percentile - MISES (99PERC) - with respect to the pre-stenting vessel volume.

The mesh convergence analysis (see figure 3.9) suggests that the mesh density increase has minor impact on the evaluated results; in particular only the maximum values of von Mises stress and strain (MISES (MAX), LE MAX PRINC (MAX)) are sensible to the mesh density; consequently, for the study purpose, we consider the respective 99 percentile values. Finally, we choose the MESH 1 since it has the lowest computational cost.

3.6.2 Kinetic-Internal energy ratio

We simulate CAS performing a quasi-static analysis using Abaqus/Explicit. In such analysis it is expedient to reduce the computational cost by either speeding up the simulation or by scaling the mass. In any case the kinetic energy (ALLKE) should be monitored to ensure that the ratio of kinetic energy to internal energy (ALLIE) does not get too large; we choose to use mass scaling adopting a treshold of 10% for energy ratio. We performed preliminary numerical tests (CAS implant using stent *B2*) to assess the impact of time step on such energy ratio and on computed values, varying the time step for step 2 form 0.03 s to 0.04 s. In figure 3.10, the ALLKE/ALLIE ratio for both cases is reported; two peaks of the energy ratio are present:

i) at beginning of the first step, due to the catheter/stent contact; ii) at the beginning of the second step, due to the stent/vessel contact. For the goal of our study, we don't consider transient/intermediate values but only the results obtained at the end of the simulation, consequently we suppose that both peaks of ALLKE/ALLIE ratio have a limited impact on the proposed results as also demonstrated by the values reported in table 3.6.

Table 3.5: Details on the meshes used for mesh convergence analysis.

Label	<i>MESH 1</i>	<i>MESH 2</i>	<i>MESH 3</i>
Number of nodes	17564	31100	60595
Number of elements	12960	23040	48000
Simulation time	22h 41m	24h 12m	27h 57m
U MAGNITUDE (MAX) [mm]	2.9457	3.0347	3.0295
MISES (MAX) [MPa]	0.530	0.5615	0.6273
MISES (99PERC) [MPa]	0.1916	0.1919	0.1990
LE MAX PRINC (MAX) [-]	0.3243	0.3368	0.3586
LE MAX PRINC (99PERC) [-]	0.2029	0.2025	0.2045

Table 3.6: Details on the meshes used for mesh convergence analysis.

Time [s] (Step 2)	0.03	0.04	Δ
Simulation time	22h 41m	29h 20m	-24%
U MAGNITUDE (MAX) [mm]	2.9457	2.7	+8%
MISES (MAX) [MPa]	0.530	0.50	+6%
MISES (99PERC) [MPa]	0.1916	0.1812	+5.7%

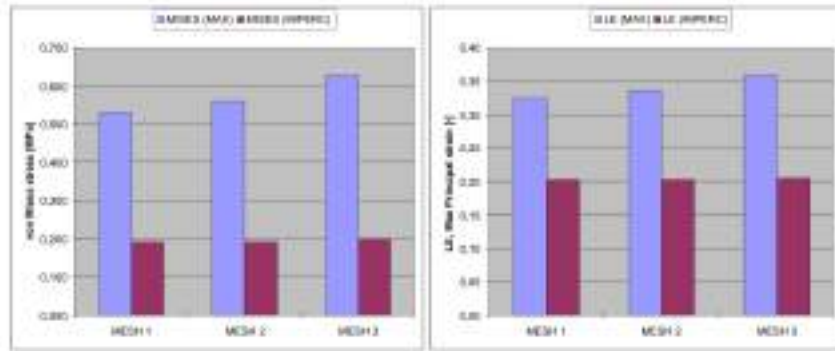


Figure 3.9: Histograms depicting the von Mises and strain values as function of mesh density.

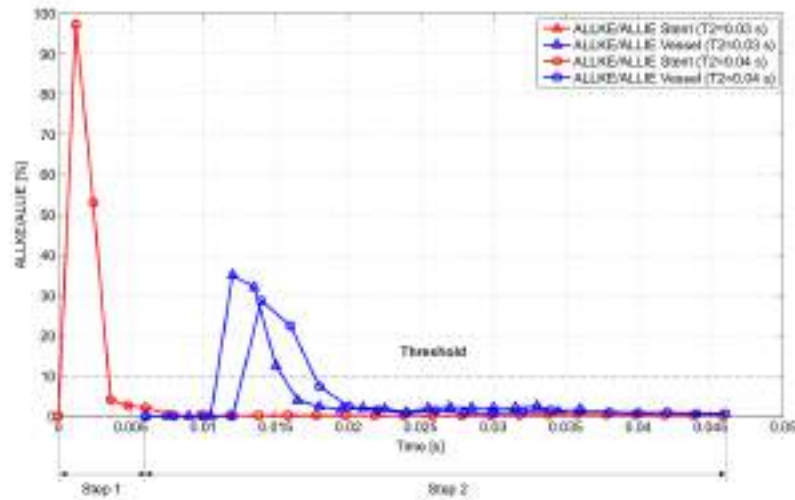


Figure 3.10: ALLKE/ALLIE ratio for both stent and vessel during the simulation.

Chapter 4

Patient-specific finite element analysis of carotid artery stenting: a focus on the vessel modeling

4.1 Introduction

Endovascular treatment of carotid artery (CA) stenosis with carotid artery stenting (CAS) has emerged as an acceptable counterpart of the surgical approach, i.e. carotid endarterectomy (CEA) [12]. However, the long-term efficacy of CAS is currently under clinical evaluation and, in particular, the role of in-stent restenosis (ISR) is not clear. ISR is a well-known drawback of stenting and consists of the post-stenting lumen re-narrowing due to neointimal hyperplasia; while such a problem is deeply investigated and treated with novel drug-eluting technology for coronary stenting [91], few and contrasting data are available for CAS as discussed in the following.

In 2005, Gröschel et al. [92] stated that the assessment of ISR rate of CAS is challenging; in fact they performed a systematic meta-analysis of all current peer-reviewed studies reporting on CAS ISR, concluding that a wide range of ISR rate (from 0.6% [93] to 20.8 % [94]) is reported in literature. The authors also highlighted that such a variability could be due to a poor

study standardization of the ISR rate computation, which indeed depends on several issues such as the adopted restenosis threshold, follow-up term, study design, etc.

In the same year, Bosiers et al. [95] reported CAS data, collected in five years from four high-volume European centers (ELOCAS registry), indicating a restenosis rate of 1%, 2% and 3.4% after 1, 3 and 5 years respectively. In 2008 De Donato et al. [96] carried out a retrospective investigation on 3179 CAS procedures, performed from 1998 to 2006, aiming at evaluating the long-term CAS outcomes; with respect to ISR, the data indicate a rate of 1.6%, 3.9% and 6% after 1, 3 and 5 years respectively; consequently the authors concluded that ISR for CAS appears to be acceptable and unrelated to device characteristics.

In the same year, Steinbauer et al. [97] analyzed the results of a prospective, randomized, single-center study revealing a high incidence (18.75%) of relevant ISR ($\geq 70\%$), but, in this case, it is necessary to underline that only one type of stent, i.e. Wallstent (Boston Scientific Co., Natick, MA, USA), was used. A high rate of ISR also appears from the data reported in the same period by Harrer et al. [98] and more recently by Nolz et al. [99]. Although we are not reporting all the available studies and literature reviews, it is evident that the clinical relevance of CAS ISR is still a matter of debate and it could become increasingly prevalent due to the exponential growth of CAS use. Consequently, more data and dedicated studies are necessary to elucidate the mechanisms of ISR and their relation with the novel technologies, which are rapidly emerging in the CAS procedure.

In this contest, computational biomechanics can play a key role investigating the relation between biomechanical factors and the development of ISR. In fact, starting from the experimental evidence that restenosis and neointimal hyperplasia are related to vessel wall injury [82, 100, 101], many studies have analysed the impact of stent deployment or angioplasty on vessel wall stress distribution through finite element analysis (FEA), just to name a few [44, 46, 102, 103, 102]. However the major part of these studies dealt with coronary stenting and only few focus on CAS [68, 69, 104].

In 2007 Wu et al. [69] have proposed a FEA strategy to simulate the delivery of a Nitinol stent design in an idealized carotid geometry in order to evaluate some biomechanical properties of two stent designs having different strut units; such a work can be considered as a first step toward a virtual investigation of CAS even when using idealized geometries for both

the vessel and the stent. More recently Auricchio et al. [104] exploited FEA to compare the performance three different stent designs, with different size and configuration, in a single patient-specific CA model with respect to different CAS outcomes as lumen gain and vessel straightening. Both studies neglect a realistic description of the plaque morphology and adopt a simplified constitutive model (i.e. hyperelastic isotropic) for the CA vessel wall. Based on the above mentioned considerations about CAS ISR and with the aim of improving the state-of-art of CAS simulations, in the present study we investigate the impact of carotid stent apposition on the vessel wall stress distribution through patient-specific finite element analysis (FEA). In particular, we focus on the influence of constitutive vessel modeling on the predicted tensional state over the CA wall.

For this purpose, we organize the study in several steps: we firstly generate a patient-specific model of CA based on CTA DICOM images including the plaque; we then consider two constitutive models, i.e. hyperelastic isotropic and hyperelastic anisotropic, for the CA vessel wall; we finally perform the FEA of CAS to assess the impact of the adopted CA constitutive model on the computed vessel wall stress state.

4.2 Material and Methods

4.2.1 Carotid artery model

Patient-based geometry

We base the CA model on DICOM images of a neck-head Computed Tomography Angiography (CTA) performed on a 70 years-old female patient. The CTA scan is performed at IRCCS San Matteo in Pavia, Italy, using a Somatom Sensation Dual Energy scanner (Siemens Medical Solutions, Forchheim, Germany). The scan data are characterized by the following features: slice thickness, 1 mm; slice width x height, 512 x 512 pixels; pixel spacing, 0.33 mm.

We elaborate the images using OsiriX [105] (see figure 4.1-a); in particular we focus on the left CA and, exploiting the thresholding of the Hounsfield unit (HU) scale, we highlight both the bifurcation lumen and the plaque as shown in figure 4.1-b. We then export the 3D surfaces of both lumen and plaque geometry in stereolithography (STL) format, i.e. as set of connected triangles (see figure 4.2-a).

To create the CA finite element mesh, we implement in Matlab (The Mathworks Inc., Natick, MA, USA) a procedure characterized by four main steps:

1. definition of vessel wall inner profile elaborating the STL surface of the lumen;
2. definition of vessel wall outer profile modifying, in an appropriate way, the inner profile;
3. generation of the mesh between the inner and outer profile;
4. identification of a subset of vessel wall elements defining the plaque.

In the first step we define the vessel wall inner profile from the point cloud, derived from the STL of the CA lumen (see figure 4.2-a), which is processed in order to define a given number of closed lines representing the cross-sectional profile of each CA bifurcation branch (i.e. common carotid artery - CCA, internal carotid artery - ICA, external carotid artery - ECA) as shown in figure 4.2-b.

In the second step since no information on vessel wall thickness is obtainable from CTA images, we reconstruct the vessel wall outer profile (see figure 4.2-c) enlarging appropriately the inner sections in order to maintain the plaque enclosed between the inner and outer profile; representative examples of this procedure are depicted and described in figure 4.3 while in table 4.1 we report the wall thickness, which varies along the CA model.

In the third step, once both inner and outer sections are defined, we interpolate both of them in the longitudinal direction with natural cubic splines defining thus the inner and outer boundary of the model; we finally connect such boundaries to define hexahedral-element mesh (see figure 4.2-d).

In the final step we define the plaque as a subset of elements including vessel wall elements which are enclosed within the 3D STL surface of the plaque; consequently, it is possible to divide the whole element set of the CA model in two subsets of elements representing respectively the CA wall and the plaque, as depicted in figure 4.4.

In order to determine the optimal CA mesh density, as a trade-off between computational cost and accuracy of results, we performed a preliminary mesh-convergence analysis which indicated a mesh having 59346 elements and 66560 nodes (see Appendix 4.7.1). With respect to a given vessel wall section, the mesh corresponds to a discretization having 42 elements in cir-

cumferential direction and 9 layers along the thickness.

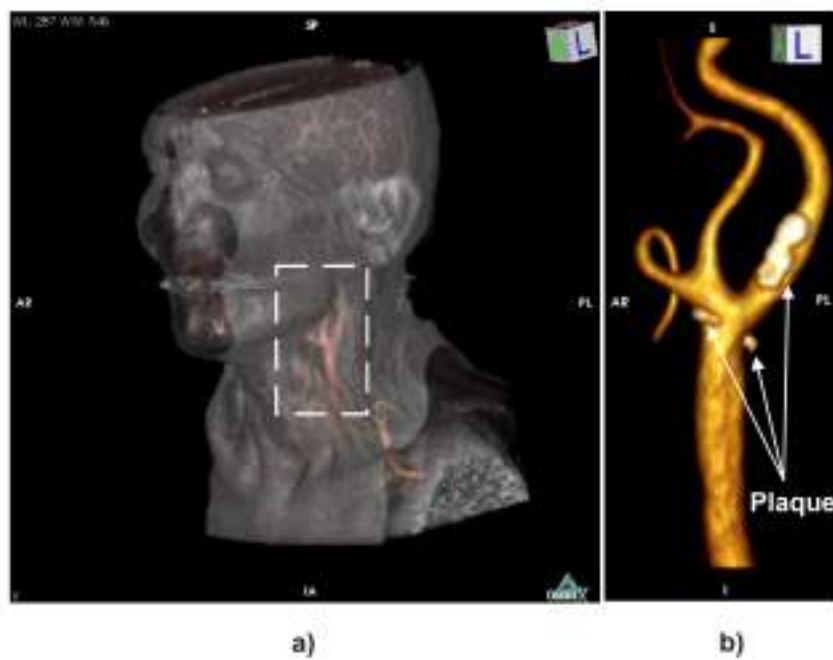


Figure 4.1: Elaboration of Computed Tomography Angiography (CTA) images: a) whole 3D reconstruction of neck-head district highlighting the region of interest; b) 3D reconstruction of both lumen of left CA bifurcation and plaque (depicted in white).

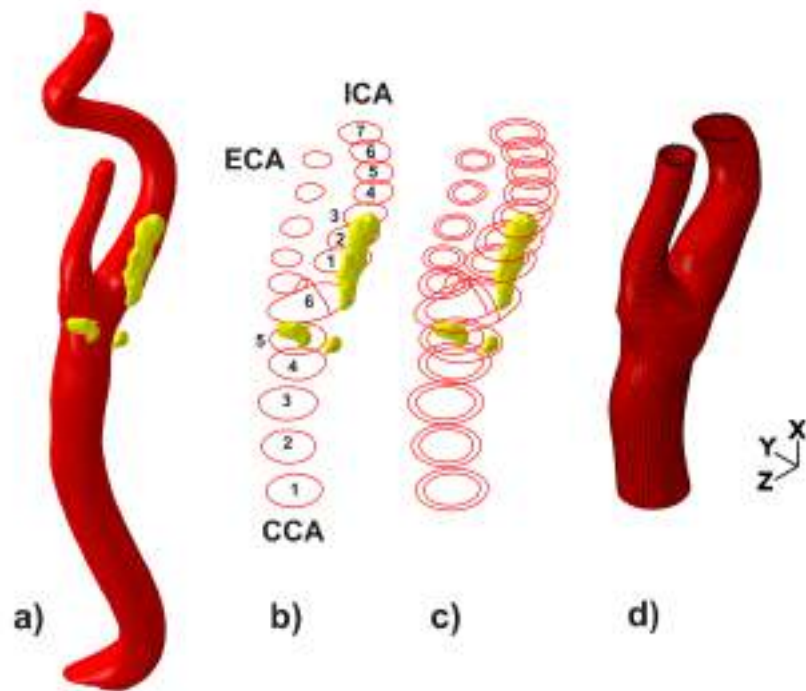


Figure 4.2: Generation of carotid aretry wall mesh: a) 3D reconstruction of vessel lumen and plaque; b) closed lines representing the inner cross-sectional profile; c) closed lines representing the inner and outer cross-sectional profiles; d) carotid artery wall mesh.

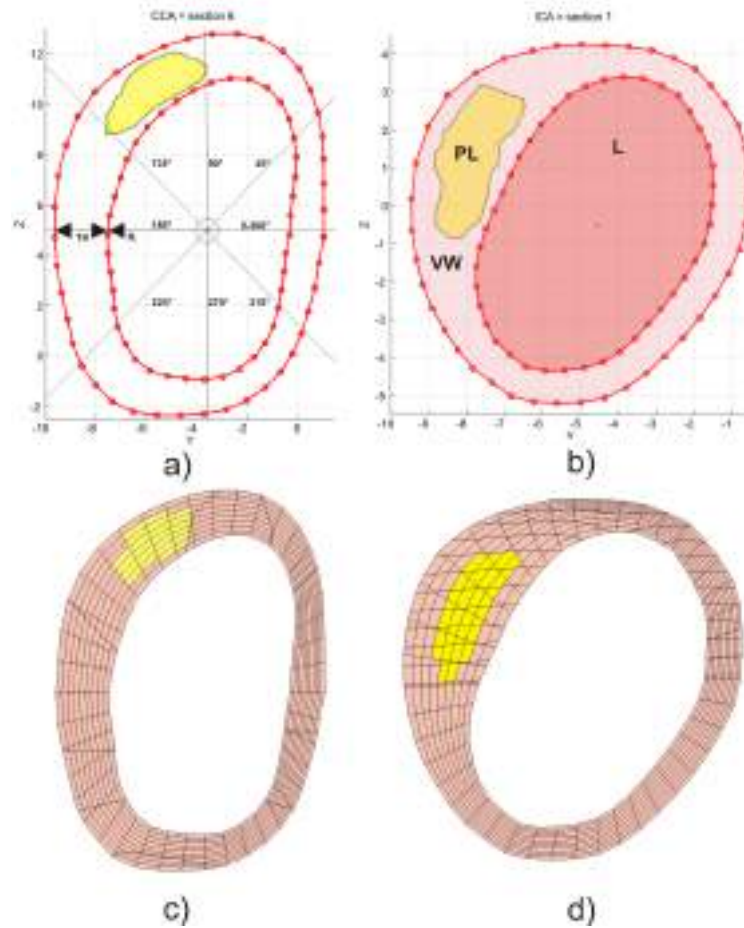


Figure 4.3: Representative examples of the definition of outer vessel wall profile: a) for each section, we define a local cylindrical coordinate system, which has the origin in the section center of mass; then, for each section point, we impose a radial displacement corresponding to the vessel wall thickness, which is defined as a percentage of radius (i.e. 28.19% for CCA and 32.31% for internal carotid artery (ICA) and external carotid artery (ECA) as suggested by values reported by Sommer et al. [72]) for the regions where there is no plaque, and appropriately increased for the regions where there is the plaque; b) obtained lumen (L), vessel wall (VW) and plaque (PL) respectively highlighted in red, pink and yellow; c-d) cut-view of the obtained mesh.

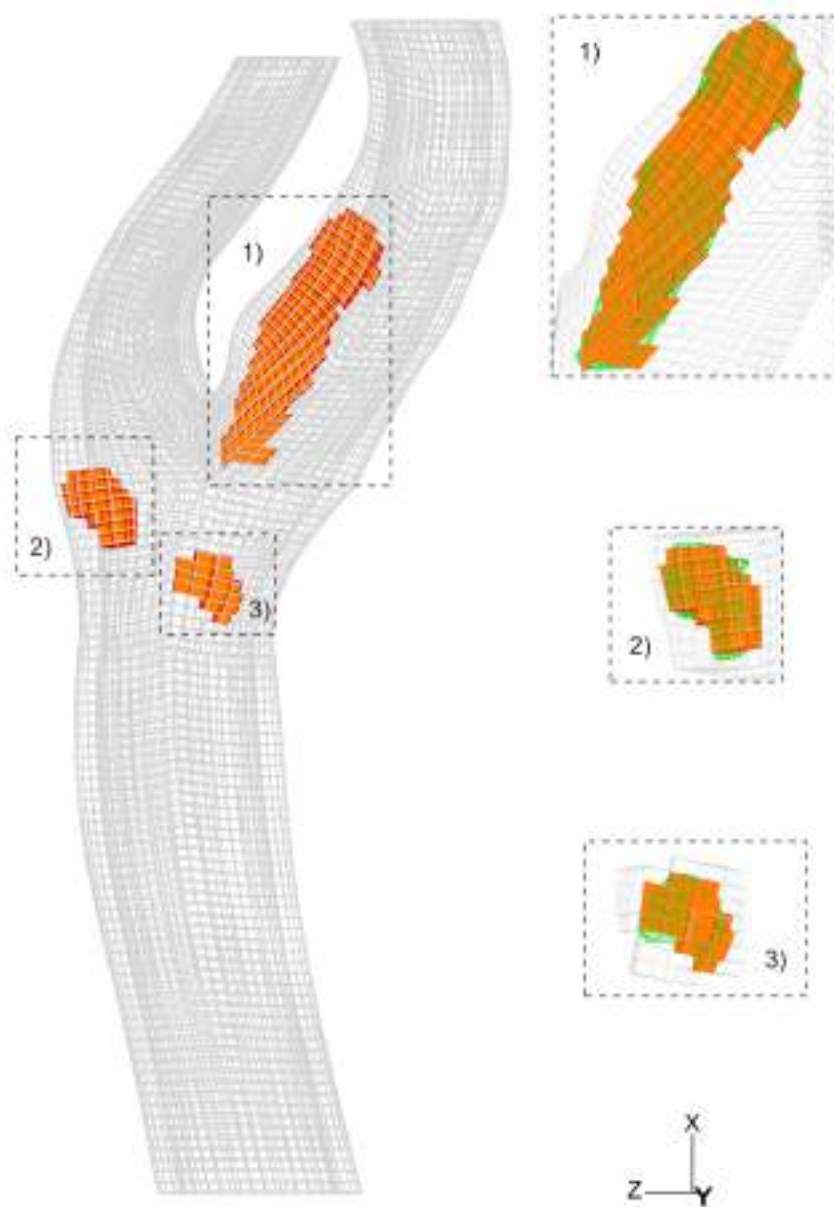


Figure 4.4: Inclusion of the plaque in the CA vessel model; the plaque (in orange) is defined assessing the elements of the vessel wall mesh (in grey) enclosed within 3D STL surface (in green) representing the plaque morphology.

Table 4.1: Lumen radius and wall thickness for the internal carotid artery (ICA) and common carotid artery (CCA) section highlighted in figure 4.2. The values are reported for each section as mean \pm standard deviation.

Section ID	ICA		CCA	
	Radius [mm]	Thickness [mm]	Radius [mm]	Thickness [mm]
1	3.4 ± 0.5	1.2 ± 0.6	3.9 ± 0.3	1.1 ± 0.0
2	3.3 ± 0.6	1.5 ± 0.7	3.8 ± 0.2	1.1 ± 0.0
3	2.8 ± 0.5	1.5 ± 0.7	4.0 ± 0.3	1.1 ± 0.0
4	2.8 ± 0.1	1.2 ± 0.5	3.9 ± 0.3	1.1 ± 0.0
5	2.7 ± 0.2	0.9 ± 0.0	3.9 ± 0.6	1.5 ± 0.7
6	2.8 ± 0.2	0.9 ± 0.0	4.8 ± 1.0	1.7 ± 0.5
7	2.8 ± 0.3	0.9 ± 0.0		

Constitutive modeling

With kinematics and equilibrium, constitutive modeling is one of the fundamental ingredients of the (continuum) solid mechanics; constitutive relations have to take into account the physical and phenomenological nature of the body and generally relate internal forces (equilibrium) and measures of configuration change of the body (kinematics); as for any other model, the constitutive equations are usually the result of a trade-off between complexity, accuracy and desired goal.

Constitutive modeling of arterial tissue is not a trivial task due to its biological complexity; it can be considered as a composite material defined by three-layers (i.e. intima - I, media - M and adventitia - ADV); moreover, anisotropic components (i.e. stiff collagen fibers with a given orientation and dispersion) are immersed in an isotropic matrix where highly distensible elastin is predominant. Such structural complexity results in a complex mechanical behavior which can be described by the following main aspects: i) high non-linear response; ii) anisotropy; iii) small hysteresis iv) non linear stiffening, especially at high levels of strain, due to the progressive recruitment of collagen fibers. If we consider *in-vivo* condition, the arterial wall is pre-stretched (due to blood pressure loading) and in an activated state (due nervous stimuli acting on the smooth muscle cells); moreover, the arterial load-free configuration is characterized by residual stresses, both in circumferential and axial direction.

Several constitutive models of arterial tissue, with different degree of complexity, are available in literature; they are usually based on the continuum theory of large deformation elasticity and described by a strain energy function (SEF), which defines the strain energy stored in the material as a function of the deformation. Once the SEF is defined, it is necessary to calibrate its parameters on experimental data obtained from tissue samples, but, since experimental data of the mechanical properties of arterial tissue are not easy to achieve, the constitutive model calibration is, in most cases, complex. This issue is particularly evident if we analyze the SEFs, and the related calibration data, adopted by the numerical investigations of the CA district available in literature.

In a pioneeristic study, on 1997, Delfino et al. [90] exploited FEA to evaluate the impact of residual strain on the stress distribution along the CA wall; in this study, the authors used an isotropic SEF calibrated on pressure-radius measurements at different values of axial stretch, obtained from experimen-

tal tests on eight relatively disease-free human CCAs [106]. The experimental data of Delfino et al. have been reused, ten years later, by Hariton et al. [107] to calibrate an anisotropic SEF [108, 109] within a study highlighting the role of loading conditions on the collagen morphology of the CA bifurcation.

In 2008, Gao et al. [110] evaluated the impact of lipid core volume and fibrous cap thickness on stress distribution in CA plaques; they used a second-order polynomial SEF for the vessel wall model referring to the study of Tang et al. [89] for the choice of the model parameters. In the cited study, Tang and colleagues propose a stress-strain curve for the vessel material which cannot be clearly referred to human CA.

In 2009, Tang et al. [28] performed a fluid-structure interaction (FSI) study, based on realistic anatomical modeling of the CA, to investigate the role of stress in the carotid plaque on possible sites of rupture. With respect to the vessel wall model, the authors proposed a Mooney-Rivlin SEF referring, for the parameter calibration, to previous works [111, 112] which also refer to literature data [113, 114].

More recently, Creane et al. [86] proposed a study aiming at evaluating the plaque vulnerability by FEA; in this study, the authors derived the material model constants of the plaque from mechanical testing of excised carotid plaque reported by Maher et al. [115] while they refer to the studies of Gao et al. [110] and Tang et al. [89] for the CA wall material model constants. In this contest, an excellent investigation of the human CA mechanical response has been carried out very recently by Sommer et al. [72, 116], who have systematically determined the biaxial mechanical properties of human CCAs and ICAs, in intact and layer-dissected status, by quasi-static extension-inflation tests at different axial stretches. The data obtained by Sommer and colleagues are particularly suited to calibrate the anisotropic SEF for fiber-reinforced material proposed by Holzapfel et al. [108] and Gasser et al. [117], representing somehow the state-of-art of arterial wall modeling.

We think it is worth to include in this brief literature review also the work of Prendergast et al. [73], despite it is not dealing with CA; in fact, in this study the authors adopted an isotropic hyperelastic model for the vascular tissue calibrating the material parameters on experimental data related based on human femoral arterial tissue; we believe that this model is appropriate for the purpose of the present study since it was successfully used

for FEA of stenting [46, 118] and it is based on accurate uni- and bi-axial tests performed on several tissue samples.

Consistently with the presented literature survey, since we aim at investigating the role of vessel wall constitutive modeling with respect to post-stenting stress distribution over the CA wall, we choose to deal with two constitutive models, i.e. isotropic and anisotropic hyperelastic.

For the isotropic model, we use a polynomial SEF:

$$U_I = \sum_{i+j=1}^N C_{ij} (\bar{I}_1 - 3)^i (\bar{I}_2 - 3)^j + \sum_{i=1}^N \frac{1}{D_i} (J^{el} - 1)^{2i} \quad (4.1)$$

where N , C_{ij} and D_i are material parameters; \bar{I}_1 and \bar{I}_2 are respectively the first and second deviatoric strain invariants; J^{el} is the elastic volume ratio.

For the anisotropic model, we use the SEF proposed by Holzapfel et al. [108] and Gasser et al. [117]:

$$U_A = C_{10}(\bar{I}_1 - 3) + \frac{1}{D} \left(\frac{(J^{el})^2 - 1}{2} - \ln(J^{el}) \right) + \frac{k_1}{2k_2} \sum_{\alpha=1}^N \left\{ \exp \left[k_2 \langle \bar{E}_\alpha \rangle^2 \right] - 1 \right\} \quad (4.2)$$

where

$$\bar{E}_\alpha \equiv k(\bar{I}_1 - 3) + (1 - 3k)(\bar{I}_{4(\alpha\alpha)} - 1) \quad (4.3)$$

and C_{10}, D, k_1, k_2 are material coefficients, while N is the number of families of fibers, in our case $N = 2$; \bar{I}_1 and $\bar{I}_{4(\alpha\alpha)}$ are invariants defined as specified in literature [108, 117, 119]. The parameter k describes the dispersion of a given fiber family, with a value ranging from 0 to 1/3; in particular $k = 0$ implies that there is no dispersion and the fibers are perfectly aligned, vice versa $k = 1/3$ implies that the fibers are randomly distributed and the material is thus isotropic; the parameter k can be derived from histological measurements or considered as a parameter to include in the material calibration process; in the present study, we assume $k = 0$ to simplify the model calibration.

Starting from the above described two SEFs, we consider the following five variants of CA material model:

1. model HI_1 : U_I with the coefficients reported by Creane et al. [86] ;
2. model HI_2 : U_I with the coefficients reported by Lally et al. [118];

3. model HA_1 : U_A calibrated on data reported by Delfino et al. [90];
4. model HA_{21} : U_A calibrated on data reported by Sommer et al. [72] for the intact wall;
5. model HA_{22} : U_A calibrated on data reported by Sommer et al. [72] for the CCA/ICA media-intima (MI) and adventitia (ADV).

Consequently we perform five different simulations, one for each considered CA model. We report in table 4.2 the adopted coefficients for each model, indicating also the corresponding references. It is worth to note that, with respect to model HA_1, HA_{21}, HA_{22} , the coefficients are obtained by appropriate fitting of the anisotropic SEF U_A on the adopted experimental data, derived from extension-inflation tests. The calibration is carried out through standard minimization technique defining the objective function χ^2 as the squared sum of the residuals, i.e., the difference between the experimental measurements and the corresponding calculated variables:

$$\chi^2(\kappa) = \sum_{\mathbf{a}}^{\mathbf{N}} \left[\frac{\mathbf{1}}{\mathbf{w}_1^2} (\mathbf{p}_i^{\Psi} - \mathbf{p}_i^{\text{exp}})_{\mathbf{a}}^2 + \frac{\mathbf{1}}{\mathbf{w}_2^2} (\mathbf{F}_z^{\Psi} - \mathbf{F}_z^{\text{exp}})_{\mathbf{a}}^2 \right] \quad (4.4)$$

where p_i, F_z are respectively the inner pressure and axial force with superscripts Ψ, exp standing respectively for model prediction and experimental measurement. The results of the fitting procedure are illustrated in figures 4.5-4.8.

Both SEFs are already available in the material library of Abaqus v. 6.9 (Simulia, Dassault Systèmes, Providence, RI, USA), the software we adopt as FEA solver; the implementation of U_A requires the assignment of local reference system for each element in order to define the relative fiber orientation; consequently we develop a dedicated subroutine in Matlab which is described in Appendix 4.7.2.

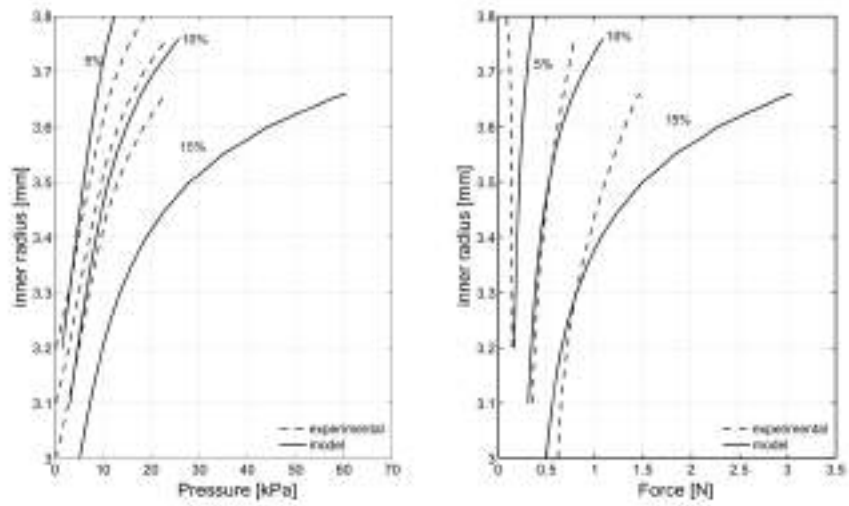


Figure 4.5: Constitutive models and data fitting: model prediction using SEF U_A fit to experimental data reported by Delfino et al. [90].

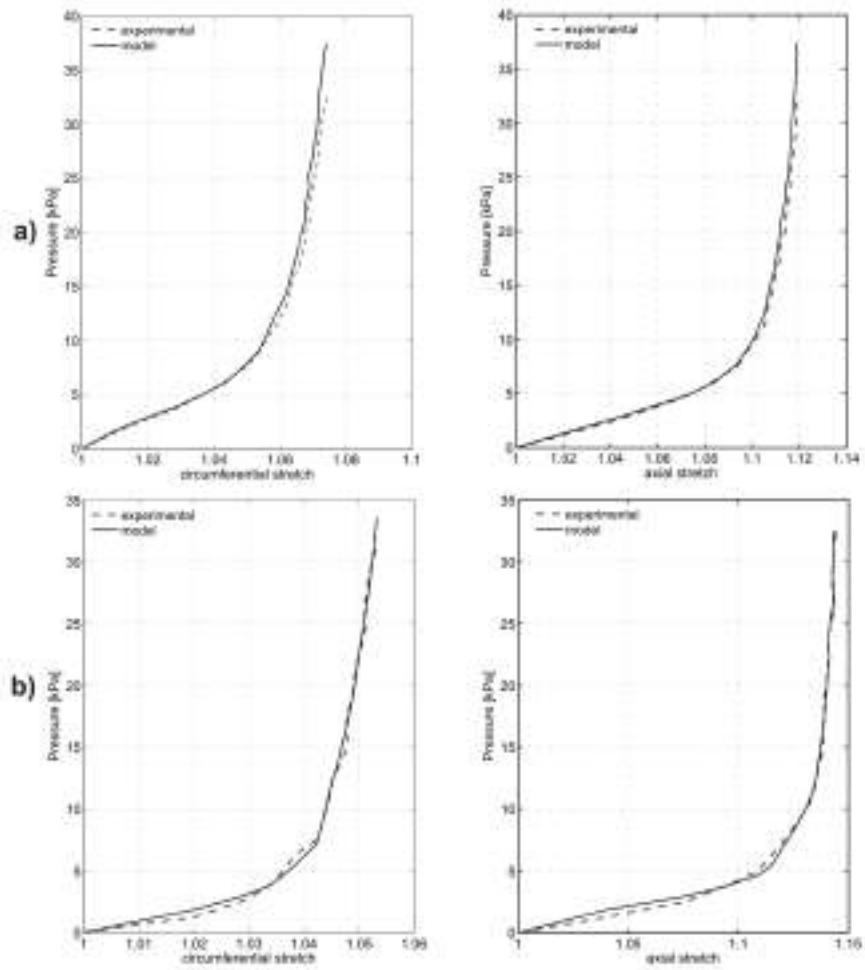


Figure 4.6: Constitutive models and data fitting: model prediction using SEF U_A fit to experimental data reported by Sommer et al. [72] about a) ICA and b) CCA intact wall.

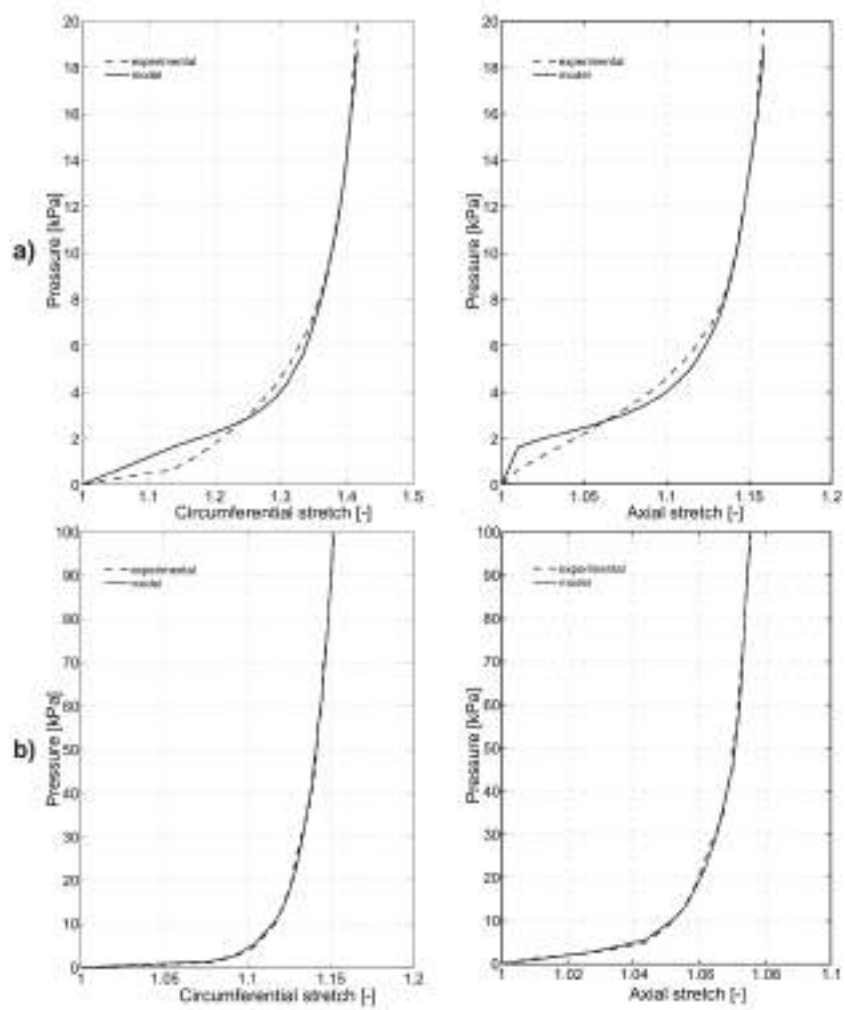


Figure 4.7: Constitutive models and data fitting: model prediction using SEF U_A fit to experimental data reported by Sommer et al. [72] about CCA a) media-intima (MI) and b) adventitia (ADV).

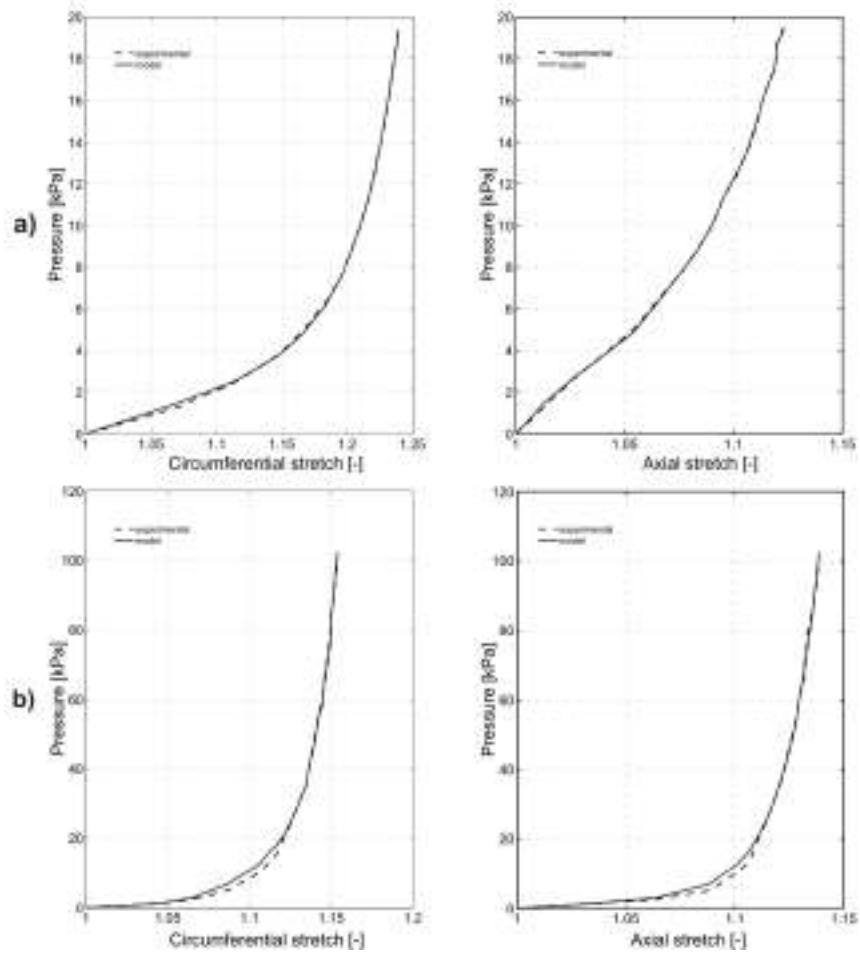


Figure 4.8: Constitutive models and data fitting: model prediction using SEF U_A fit to experimental data reported by Sommer et al. [72] about ICA a) media-intima (MI) and b) adventitia (ADV).

Table 4.2: Constitutive parameters of the adopted SEFs in the five model variants.

Model label	Vessel		Plaque	
HI_1	$C_{10}=50.45$ kPa $C_{01}=30.49$ kPa $C_{20}=40$ kPa $C_{11}=120$ kPa $C_{02}=10$ kPa	Reference: Creane et al. [86] SEF: U_I (2nd order)	$C_{10}=4.8$ kPa $C_{01}=60$ kPa $C_{20}=240$ kPa $C_{11}=377$ kPa $C_{02}=781$ kPa	Reference: Creane et al. [86] SEF: U_I (2nd order)
HI_2	$C_{10}=18.90$ kPa $C_{01}=2.75$ kPa $C_{20}=590.43$ kPa $C_{11}=85.72$ kPa	Reference: Lally et al. [118] SEF: U_I (2nd order)	$C_{10}=-495.96$ kPa $C_{01}=506.61$ kPa $C_{20}=3637.8$ kPa $C_{11}=1193.53$ kPa $C_{30}=4737.25$ kPa	Reference: Lally et al. [118] SEF: U_I (3rd order)
HA_1	$C_{10}=20.38$ kPa $k_1=17.56$ kPa $k_2=16.92$ $\gamma=47.15^\circ$	Reference: Delfino et al. [106] SEF: U_A	see model HI_1	
HA_{21}	CCA - Wall $C_{10}=24.43$ kPa $k_1=1.66$ kPa $k_2=111.4$ $\gamma=47.89^\circ$	ICA - Wall $C_{10}=13.72$ kPa $k_1=0.52$ kPa $k_2=195.32$ $\gamma=33.78^\circ$	see model HI_1	
Reference: Sommer et al. [72]; SEF: U_A				
HA_{22}	CCA - MI $C_{10}=7.6$ kPa $k_1=5.36$ kPa $k_2=11.23$ $\gamma=57.11^\circ$	ICA - MI $C_{10}=4.96$ kPa $k_1=5.5$ kPa $k_2=10.19$ $\gamma=31.35^\circ$	see model HI_1	
	CCA - ADV $C_{10}=0.83$ kPa $k_1=6.1$ kPa $k_2=68.29$ $\gamma=41.37^\circ$	ICA - ADV $C_{10}=0.1$ kPa $k_1=22.11$ kPa $k_2=34.57$ $\gamma=29.76^\circ$		
Reference: Sommer et al. [72]; SEF: U_A				

4.2.2 Stent finite element model

With respect to the stent design, we consider a 9mm Bard ViVEXX Carotid Stent (C. R. Bard Angiomed GmbH & Co., Germany), an *open-cell* self-expanding Nitinol stent with a straight configuration. The model is based on micro-CT scans of the real device; more details are provided in section 5.2.1.

4.2.3 Finite element analysis of carotid artery stenting

The simulation of CAS is performed assembling the following parts:

- a patient-specific CA model;
- the stent;
- the catheter.

The catheter is modeled as a rigid body defined by a surface obtained by sweeping a cylindrical section along the centerline of the vessel; we mesh it with 2760 three-dimensional, 4-node surface elements with reduced integration (SFM3D4R). In our simulation strategy, the stent deformation is imposed by the configuration change of the catheter, imposed by displacement boundary conditions (BCs) on its nodes; the BCs are determined as the difference between a starting and final catheter configuration for each simulation step. In particular the simulation consists of two steps:

1. stent crimping and bending: starting from a straight configuration the catheter is gradually bent and crimped accomplishing the vessel centerline and leading to the stent deformation; the contact between the stent and the vessel is deactivated in this step;
2. stent deployment: from the bent and crimped configuration, the catheter is re-enlarged and consequently the stent expands against the vessel wall; the contact between the stent and the vessel is activated in this step.

The simulation is performed using Abaqus/Explicit v. 6.9 as finite element solver since the numerical analysis is characterised by non-linearity due to the material properties, large deformations and complex contact problems. With respect to the vessel ends, we define ad hoc local cylindrical coordinate systems to fix the corresponding nodes in the longitudinal and in the

circumferential direction allowing consequently only radial displacements. With respect to the stent, the longitudinal displacement of the nodes lying at the proximal end of the stent are restrained in order to maintain the longitudinal position of the stent equal for all the simulations.

We assume no internal pressure on the vessel wall under the hypothesis that the geometry is based on measurements achieved at 80 mmHg. A general contact algorithm is used to handle the interactions between all model components; in particular a frictionless contact between the stent and the vessel inner surface is assumed. For more details please refer to section 3.2.3.

4.2.4 Post-processing

We elaborate the results of the simulations in order to highlight the impact of the adopted CA models on the tensional state of the post-stenting vessel wall; the tensional state is investigated either from the quantitative and qualitative point of view assuming the von Mises stress σ_M ¹ as stress measure. From a quantitative point of view, we elaborate σ_M to define the three following indices:

- σ_M^{Max} : the maximum value of σ_M with respect to all CA elements;
- σ_M^{99P} : this index corresponds to the cut-off σ_M value at 99% of the cumulative histogram with respect to pre-stenting vessel volume (i.e. only 1% of the volume has σ_{Mises} above σ_M^{99P});
- σ_M^{Mean} : this index is defined as $\sigma_M^{Mean} = \sum_{i=1}^N \sigma_{M_i} V_i / \sum_{i=1}^N V_i$ where V_i is the element volume and N is the number of elements whose σ_M is above 0.1 kPa.

From a qualitative point of view, we evaluate the contour plot of σ_M indicating the stress distribution over the vessel wall; as we want to verify whether the position of the more stressed regions with respect to CA anatomy is independent from the material model. Therefore, we refer to pre-stenting configuration and, for each CA model, we rescale the contour legend with respect to corresponding σ_M^{99P} .

¹The von Mises stress σ_M (or Equivalent stress) is a scalar quantity resuming the tensional state represented by the second-order stress tensor $\boldsymbol{\sigma}$; in Abaqus, $\sigma_M = \sqrt{\frac{3}{2} \mathbf{S} : \mathbf{S}}$, where \mathbf{S} is the deviatoric stress tensor, defined as $\mathbf{S} = \boldsymbol{\sigma} - p\mathbf{I}$, where $p = tr(\boldsymbol{\sigma})$ is the pressure stress. In FEA regarding vascular structures [30, 110] this quantity σ_M is often used as a stress measure, i.e. as an index of vessel wall tensional state.

4.3 Results

Five different simulations were performed, one for each considered CA model and, as an example of the performed simulations, we report in figure 4.9 the vessel, the stent and the catheter configuration during CAS simulation for model HA_1 , while figure 4.10 depicts the contour plot of σ_M with respect of the pre-stenting vessel wall for the five CA models.

The three stress indices, i.e. σ_M^{Max} , σ_M^{99P} and σ_M^{Mean} for both CA wall and plaque as function of CA models are reported in table 4.3 and depicted in figure 4.11.

With respect to CA wall, the results indicate that:

- the three stress indices do not provide a similar trend;
- the maximum value of each index corresponds to different models (model HA_1 for σ_M^{Max} , model HI_2 for σ_M^{99P} , model HI_1 for σ_M^{Mean});
- the minimum value of each index corresponds to model HA_{22} ;
- if we consider the average value of each index, σ_M^{Max} is almost twice than σ_M^{99P} , i.e. 152.6 kPa vs 79,8 kPa, and σ_M^{Mean} is notably lower, i.e. 11.6 kPa, than other two indices.

With respect to plaque, σ_M^{99P} and σ_M^{Mean} have the same trend providing higher value for model HA_1 .

Table 4.4 and figure 4.12-top detail the stress indices of ICA and CCA obtained with model HA_{21} while table 4.5 and figure 4.12-bottom detail the stress indices for the layers (MI and ADV) of CCA and ICA obtained with model HA_{22} ; the results indicate that:

- for model HA_{21} σ_M^{Max} and σ_M^{99P} are higher in CCA when compared to ICA, but this indication is not confirmed by σ_M^{Mean} ;
- for model HA_{22} all the indices indicate ICA MI and CCA ADV respectively as the layer with higher and lower tensional state.

From a qualitative point of view, the analysis of the contour plots of figure 4.10 indicates that:

- for all the models, the region experiencing the higher tensional state is the distal part of the ICA;

- with respect to the CCA, the model HA_{22} predicts a lower tensional state when compared to the other four models which instead indicate a concentration of stress in the proximal part.

Table 4.3: Stress indices for CA wall and plaque as function of CA models.

CA Wall					
Model Label	HI_1	HI_2	HA_1	HA_{21}	HA_{22}
σ_M^{Max}	152.4	193.6	236	91.3	89.8
σ_M^{99P}	95.7	116.3	86.2	68.5	32.3
σ_M^{Mean}	15.7	13.9	12.1	11.1	5.4
Plaque					
Model Label	HI_1	HI_2	HA_1	HA_{21}	HA_{22}
σ_M^{Max}	46.9	96.2	92.3	61.9	49.6
σ_M^{99P}	46.3	74.2	81.5	56.5	49.6
σ_M^{Mean}	15.5	19.9	23.1	18.9	11.8

Table 4.4: Stress indices for CA wall, ICA and CCA in case of model HA_{21} .

Model HA_{21}	Wall	ICA	CCA
σ_M^{Max}	91.3	79.5	91.3
σ_M^{99P}	68.5	58.5	70.9
σ_M^{Mean}	11.1	15.4	9.0

Table 4.5: Stress indices for CA wall, ICA and CCA layers (i.e. MI and ADV) in case of model HA_{22} .

Model HA_{22}	Wall	ICA (MI)	ICA (ADV)	CCA (MI)	CCA (ADV)
σ_M^{Max}	89.8	89.8	21.7	12.9	9.9
σ_M^{99P}	32.3	54.1	18.8	8.6	5.8
σ_M^{Mean}	5.4	8.5	5.3	3.0	2.3

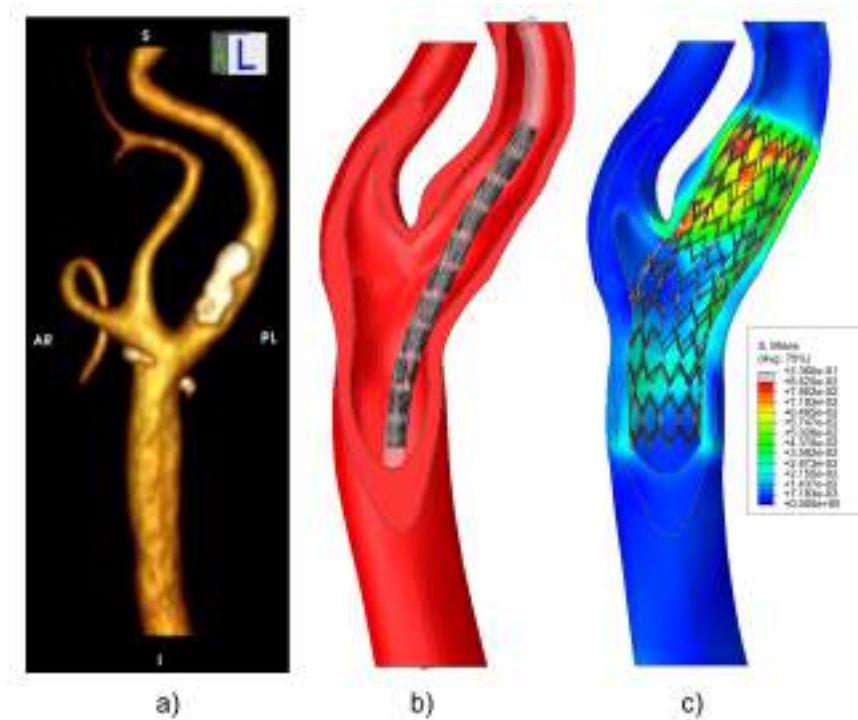


Figure 4.9: FEA of CAS: a) 3D reconstruction of CA lumen from CTA images; b) stent crimped in the delivery system during the simulation; c) contour plot depicting the post-stenting stress distribution over the vessel wall (model HA_1) at the end of the simulation, the cut-view option is used for the vessel and MPa is the unit of measure for stress.

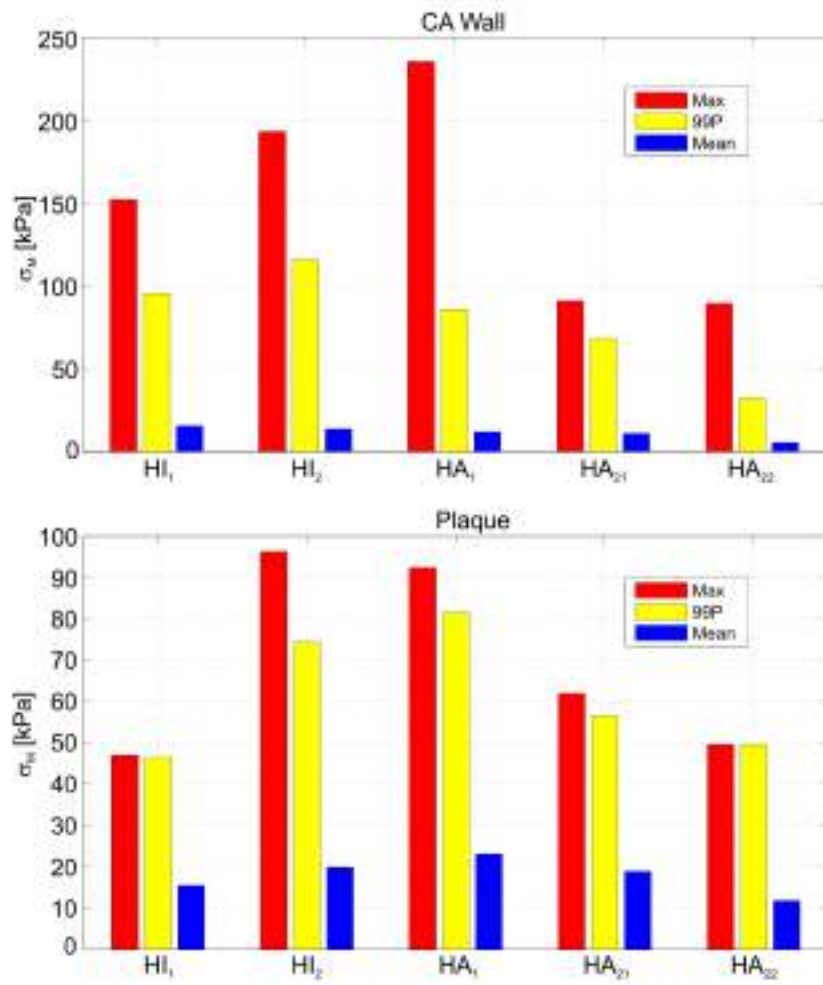


Figure 4.11: Stress indices for the CA wall and plaque for the considered CA models.

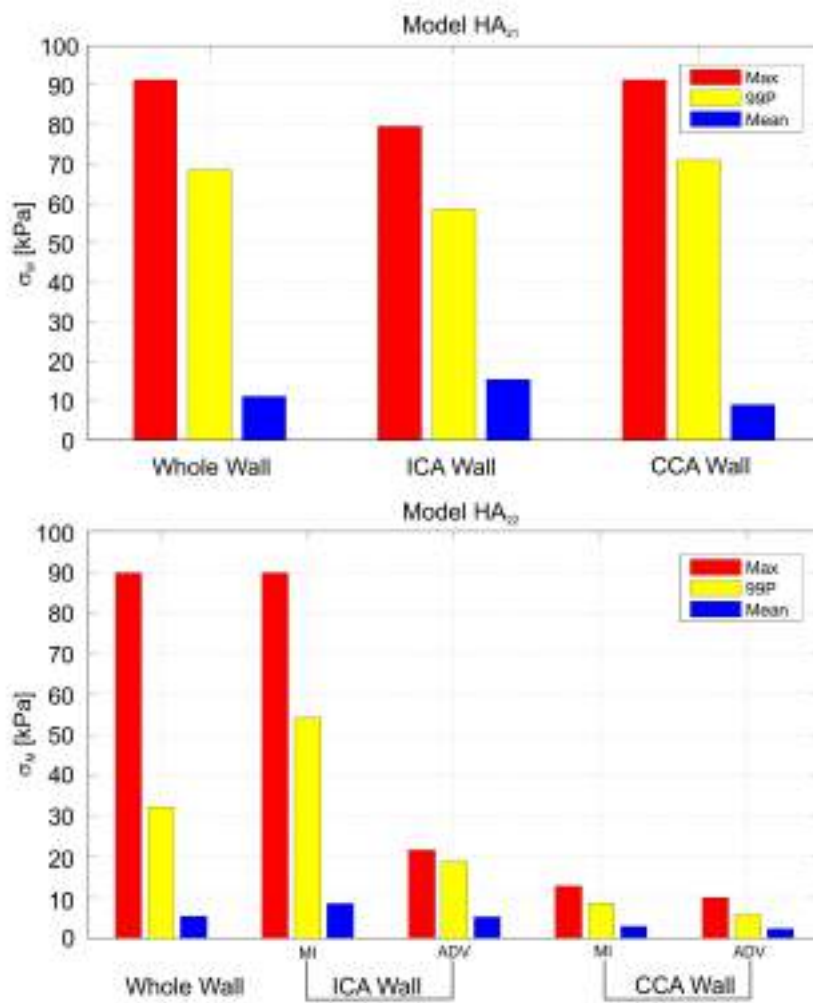


Figure 4.12: Stress indices for CA wall, ICA and CCA in case of model HA_{21} (on top); Stress indices for CA wall, ICA and CCA layers in case of model HA_{22} (on bottom)

4.4 Discussion

The clinical relevance of in-stent restenosis (ISR) for carotid artery stenting (CAS) is still a matter of debate and it could become increasingly prevalent due to the exponential growth of performed CAS procedures; moreover, novel CAS technologies and carotid stent designs are rapidly appearing, thus leading to a need of procedure standardization and to a deeper insight into ISR mechanisms.

In this scenario, computational biomechanics can play a key role investigating the relation between biomechanical factors and the development of ISR. Nowadays, finite element analysis (FEA) is a consolidated numerical technique in computational biomechanics, and in particular FEA of stenting is exploited to predict the tensional state induced by the stent apposition over the vessel wall as a measure of vessel injury, which can potentially drive ISR. Several studies about FEA of coronary stenting are available in literature, while the numerical simulations of CAS are rather limited. A realistic simulation of CAS is not a trivial task as it consists of several ingredients ranging from an accurate modeling of stent and CA anatomy to an appropriate modeling of vessel tissue mechanical behavior. The state-of-art of vessel modeling is based on patient-specific geometrical information derived from advanced medical imaging, but the patient-specific vessel modeling is still confined to the anatomical features as the patient-specific characterization of the vessel mechanical behavior is still a challenge of the (computational) biomechanics; for this reason, we refer to data test from excised human CA tissue available in literature. Moreover, several constitutive models have been proposed to describe the complex mechanical behavior of arterial tissue.

Based on the above considerations, in this study, we investigate the impact of carotid stenting on CA wall stress distribution through patient-specific FEA; in particular, we focus on the influence of constitutive vessel modeling on the predicted tensional state of the CA wall. For this purpose we consider one stent design, one patient-specific CA model and five CA material models obtained by combining the data derived from different mechanical tests on excised human arterial tissue reported in literature with two main constitutive models, i.e. hyperelastic isotropic vs hyperelastic anisotropic. We perform five different CAS simulations, one for each considered CA model, post-processing the simulation results to compute three stress indices (i.e. σ_M^{Max} , σ_M^{99P} and σ_M^{Mean}) representing the post-stenting tensional

state of the CA wall.

The analysis of the stress indices does not provide a clear trend between the considered models: if we exclude σ_M^{Max} which can be due to local stress concentrations, the range of σ_M^{99P} is 116.3-32.3 kPa, while the range of σ_M^{Mean} is 15.7-5.4 kPa. Such values fall within the stress ranges reported by similar numerical studies on CA available in literature, but such a comparison is not trivial as material models, stress indices and loading conditions differ. Delfino et al. [90] demonstrate that in the model of the CA bifurcation with residual strain, the distribution of maximum principal stress along the inner wall and the circumferential stress throughout the wall is much more uniform than in the model without residual strain; for example, they compute principal stresses, at the center of the bifurcation apex, ranging from 132 to 221 kPa with residual strain and from 236 to 655 kPa without residual strain.

Hariton et al. [107], proposing a stress-driven model for the relation between the collagen morphology and the loading conditions in arterial walls, compute a maximum value of 189 kPa for the first principal stress (i.e. for circumferential direction) located at the inner layer of the artery. Gao et al. [110] analyze 13 CA bifurcations through one-way FSI simulation to investigate the impact of fibrous cap thickness and lipid core volume to the wall tensile stress value; they report maximum von Mises stress ranging from 387 to 122 kPa, while the corresponding cut-off value of 90% in cumulative histogram ranges from 130 kPa to 72 kPa.

Kiousis et al. [120] propose a FEA-based methodology to analyze the effect of changes in the lipid core and calcification on the wall stresses, reporting a maximum principal stress up to 150 kPa.

Tang et al. [28] in a recent work perform FSI analysis to confirm the hypothesized that high structural stress in CA bifurcations with atherosclerotic plaques at critical sites may contribute to plaque disruption; with respect to the CA wall, they report a mean value of stress equal to 66.8 kPa. Moreover in a recent study, Auricchio et al. [104] simulate CAS through FEA, using different stent designs in one patient-specific anatomy reporting values of σ_M^{99P} ranging from 309 kPa to 94 kPa and highlighting the dependency of post-stenting vessel wall stress on the stent design and configuration.

It is evident that the five proposed CA models have different modeling features and it is possible to classify them in four different levels of complexity:

- level 1 - homogeneous, single-layer, isotropic model (models HI_1, HI_2):

it does not differentiate the mechanical behavior of the CA branches (i.e. CCA and ICA/ECA) and does not take into account the layered structure of the vessel wall and its anisotropic mechanical behavior;

- level 2 - homogeneous, single-layer, anisotropic model (model HA_1): it improves level 1 accounting for the anisotropic behavior of the vessel wall;
- level 3 - non-homogeneous, single-layer, anisotropic model (model HA_{21}): it improves level 2 differentiating the mechanical response of CCA and ICA/ECA branches;
- level 4 - non-homogeneous, multi-layer, anisotropic model (model HA_{22}): it improves level 3 distinguishing two layers (i.e. media-intima - MI - and adventitia - ADV) of the vessel wall;

Based on these considerations, if we assume model HA_{22} as the most complex model and so the reference model, the deviation² between the stress computed using the other models and the reference model ranges from 112% to 260% for σ_M^{99P} and from 103% to 189% for σ_M^{Mean} . Such results confirms the data reported by Holzapfel et al. [121] in an excellent study assessing the impact of balloon angioplasty on vessel wall stress through FEA, exploiting accurate artery modeling based on MRI imaging; in fact, the authors conclude that vessel model simplifications as neglecting axial *in-situ* prestretch, assuming plain strain state or isotropic material response can lead to maximum stress deviations up to 600% with respect to the reference simulation.

4.5 Limitations

The main novelties of the present study are to: i) consider realistic CA vessel anatomy; ii) include the plaque in CA model; iii) consider different level of complexity with respect to constitutive modeling of CA tissue. Despite these modeling features, this study has still different limitations which can be addressed in future developments.

²In order to quantify the stress differences between the reference model, i.e. model HA_{22} , and the other models, the stress deviation is calculated according to $100 * \frac{|r-s|}{r}$, where s denotes as a stress value from a given model and r the corresponding value from the reference model [121].

We consider a carotid artery which does not show a significant stenosis, despite the presence of plaque, as the vessel wall experiences positive remodeling (i.e. the vessel wall counteracts the plaque growth by outward enlargement to avoid lumen narrowing). In clinical practice, this case would not be considered for stenting [9] but, given the comparative nature of the present study, we consider this approach reasonable.

Even though a realistic morphology of the plaque is included in the CA model, we do not distinguish its components (e.g. lipid pool, necrotic core, calcific nodule, fibrous cap etc.) to simplify the analysis. It is worth to note that in literature several numerical studies include plaque components in the CA model [28, 110, 120] starting from high-resolution MRI images; however, we base our CA model on CTA as this imaging technique is currently used in the clinical practice in our hospital institution, IRCCS San Matteo (Pavia, Italy) to plan the CAS³. While CTA can offer a high spacial resolution when compared to MRI, its drawback is that healthy wall thickness cannot be assessed and plaque characterization requires dedicated CT machine settings and reconstruction algorithms [5, 84, 85]. Consequently, since the outer boundary of the CA can not be assessed by CTA, we reconstruct it by appropriate hypotheses (see section 4.2.1) imposing a variable wall thickness along the CA model; as reported in table 4.1, the average wall thickness ranges from 1.5 mm to 0.9 mm for the ICA from 1.7 mm to 1.1 mm for CCA, these values are congruent with the data reported by Astor et al. [123] who conclude that: i) atherosclerotic thickening in the ICA appears to be accommodated for vessels with a maximum wall thickness of less than 1.5 mm; ii) beyond this threshold, a greater thickness is associated with a smaller lumen; iii) the CCA appears to accommodate a wall thickness of less than 2.0 mm.

With respect to the constitutive modeling of the vessel tissue, it is worth to highlight that we base our model on fitting the data reported by Sommer et al. [72] on a single set of data (i.e. 0% axial stretch) for each test case (i.e. CCA/ICA wall and CCA/ICA MI/ADV), clearly the consideration of a wider number of datasets and different levels of axial pre-stretch can influence the model fitting process providing thus different model coefficients [116]. A number of other aspects were also neglected, such as luminal blood pressure, prestretch and residual stresses. An additional limitation of our

³For an overview on the role of medical imaging for diagnosis and treatment of CA stenosis, the reader should refer to [5, 122]

model is the absence of any rupture mechanism in the arterial components. All these simplifications could of course influence the results.

4.6 Conclusions

In the present study, we investigate the impact of carotid stenting on the CA wall stress distribution through patient-specific FEA; in particular, we focus on the influence of the constitutive vessel modeling on the predicted tensional state of the CA wall. The results highlight the wide variability of the computed stress with respect to adopted constitutive models underlying so the role of an appropriate vessel modeling with respect to the deductions drawn from numerical simulation of stenting.

From a more general point of view, since FEA is nowadays a well-assessed technique to investigate the impact of stenting on the vessel wall and given the rapid evolution of both medical imaging techniques and computational methods, the challenge of using FEA of CAS as a procedure planning tool supporting the clinical practice seems feasible. Following this idea, keeping the highlighted limitations in mind, the present study represents a further step towards a realistic simulation environment for CAS.

4.7 Appendix

4.7.1 Mesh convergence analysis

We performed a preliminary mesh-convergence analysis in order to assess the impact of the mesh density considering the following output variables: 1) capability of the mesh generation procedure to capture the plaque morphology; 2) predicted values of vessel wall stress. Consequently, we created different CA models, with different mesh densities, by varying the number of elements along the wall thickness (EL_{th}) and cross-sectional circumference (EL_{circum}). We chose a final mesh defined by $EL_{th} = 9$ and $EL_{circum} = 42$ as it represents a good trade-off with respect to the considered output variables, which are detailed in the following sections.

Plaque morphology

The mesh-convergence analysis with respect to the plaque volume is purely geometrical as we refer to the difference (Δ_{vol}) between the plaque volume predicted by the element set "plaque" and the volume enclosed into the STL surface derived from CTA scans. The results of the analysis are reported in table 4.6 and table 4.7; it is possible to note that Δ_{vol} converges to 10% (i.e. plaque volume of about 60 mm^3) for $EL_{th} > 3$ and is minimally influenced by the increase of EL_{circum} . Since refining the mesh further would increase the computational costs dramatically without improving sensibly Δ_{vol} , further developments of the strategy proposed in section 4.7.1 should modify the approach to improve its accuracy.

Predicted vessel wall stress

The mesh-convergence analysis with respect to the vessel wall stress is performed computing σ_M^{99P} by a FEA of the CA inflation under an inner pressure ramping from 0 to 0.01 MPa using Abaqus/Standard as FEA solver. The results of the analysis are reported in tables 4.8-4.9; it is possible to note that both parameters have a limited impact on the computed stress.

Table 4.6: Mesh-convergence analysis with respect to plaque volume varying EL_{th} .

Reference volume	66.7 mm ³			
EL_{th}	3	6	9	12
Number of plaque elements	190	460	680	900
Plaque volume [mm ³]	49.61	60.16	58.79	58.76
Δ_{vol}	-25.6%	-9.8%	-11.9%	-11.9

Table 4.7: Mesh-convergence analysis with respect to plaque volume varying EL_{circum} .

Reference volume	66.7 mm ³			
$EL_{th} = 9$				
EL_{circum}	42	50	62	70
Number of plaque elements	680	814	991	1125
Plaque volume [mm ³]	58.79	58.94	58.16	58.58
Δ_{vol}	-11.9%	-11.7%	-12.8%	-12.2
$EL_{th} = 6$				
EL_{circum}	42	50	62	70
Number of plaque elements	460	559	679	768
Plaque volume [mm ³]	60.19	60.7	59.41	59.79
Δ_{vol}	-9.8%	-9.0%	-10.9%	-10.4

Table 4.8: Mesh-convergence analysis with respect to vessel wall stress varying EL_{th} .

EL_{th}	3	6	9	12
Number of CA wall elements	19592	39104	58666	78228
σ_M^{99P} [kPa]	121.4	119.2	117.8	117.1

Table 4.9: Mesh-convergence analysis with respect to vessel wall stress varying EL_{circum} .

$EL_{circum}(EL_{th} = 6)$	42	50	62
Number of CA wall elements	39104	46541	57725
σ_M^{99P} [kPa]	119.2	118.5	118.5

4.7.2 Assigning local coordinate system for fiber orientation

In the following we describe the adopted procedure to assign an appropriate local coordinate system to each element of the vessel mesh as required for the implementation of the anisotropic hyperelastic model available in Abaqus.

If we consider the artery as a cylindrical tube, its geometry can be described by using a cylindrical coordinate system defined by three unit vectors e_1, e_2, e_3 which represent radial, circumferential and axial direction, respectively. Under this idealization, collagen fibers are supposed to be symmetrically helically disposed with respect to the circumferential direction [108, 124]: in the undeformed configuration, the fiber orientations are locally defined by two unit vectors a_{01} and a_{02} lying in the plane tangent to the cylindrical surface which contains the circumferential and the axial directions, e_2 and e_3 . In this plane, the unit vectors a_{01} and a_{02} form constant angles $\pm\gamma$ with the circumferential direction. For this particular case, the components of the unit vectors a_{01} and a_{02} with respect to the cylindrical coordinate system (e_1, e_2, e_3) are:

$$a_{01} = (0, \cos \gamma, \sin \gamma), \quad a_{02} = (0, \cos \gamma, -\sin \gamma). \quad (4.5)$$

Therefore, the definition of the fiber orientation is related to the definition of the local coordinate system e_1, e_2, e_3 and γ .

Let's now generalize the previous discussion to more complex geometries as a bifurcated vessel (see 4.13-a), where the centerline is defined as a sequence of segments (see 4.13-b); we consider, in our approach, each *segment* k of the centerline as the local axial axis (e_3) of a corresponding set of the elements, *element set* k , assessed by the following steps:

1. for each *segment* k of the centerline find the middle point M_k ;
2. for each *element* i of the mesh find the barycenter G_i ;
3. for each *element* i of the mesh compute the distance $\overline{G_i M_k}$;
4. assign *element* i to *element set* k which corresponds to the minimum of $\overline{G_i M_k}$.

Then, for each *element* i of *element set* k , the local basis e_1, e_2, e_3 is defined as follows:

- axial axis, e_3 : this vector has the same orientation of the *segment* k defined by the points a_k and b_k of the centerline;
- radial axis, e_1 : this vector lies in the plane defined by points G_i, a_k, b_k and is perpendicular to e_3 ; thus, e_1 has the direction of the segment $\overline{G_i H_k}$;
- tangential axis, e_2 : this vector is obtained by computing the vector product $e_2 \times e_3$.

Clearly, the three vectors e_1, e_2, e_3 are defined orthogonal and then normalized. Finally, the basis e_1, e_2, e_3 is properly rotated according the orientation of the element (see 4.13-c); this procedure is iteratively applied to identify a local cylindrical coordinate system for each element of the mesh (see 4.13-d). Given the local basis, the fiber orientation for each element is given by Eq.4.5. We implement the procedure for brick-like elements or 4-nodes planar elements but it can easily be adapted to triangular or tetrahedral meshes.

Other procedures to automatically define the distribution of collagen fibers for models of vascular structures have been reported by Hariton et al. [125], Kioussis et al [120] and Mortier et al. [30].

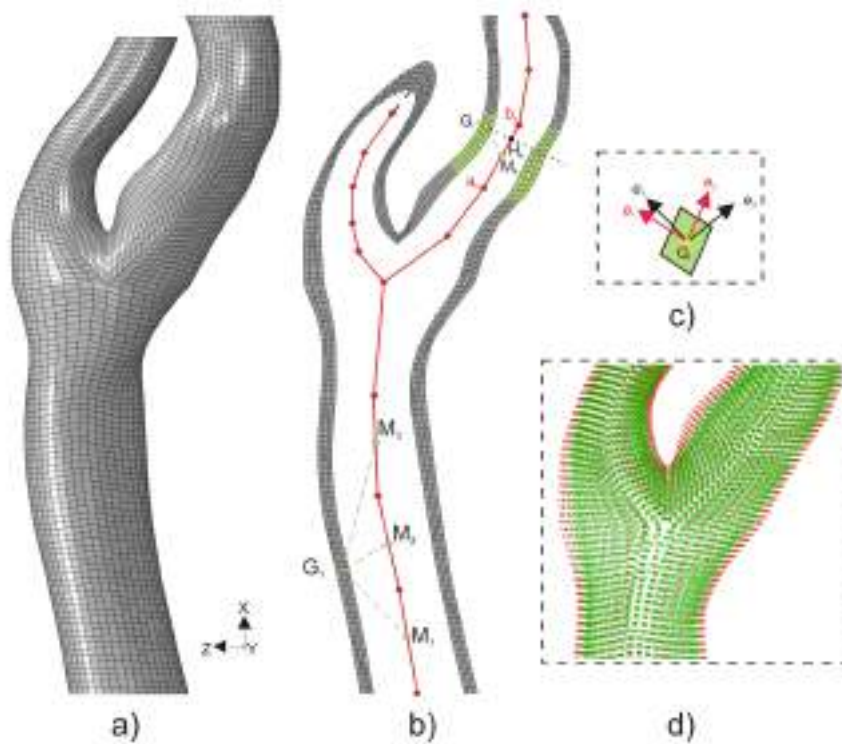


Figure 4.13: a) Mesh of the CA model; b) example of local coordinate system definition; c) local cylindrical coordinate system rotation to accomplish element orientation; d) obtained collagen fiber distribution at bifurcation for MI layer (green crosses) and ADV layer (red crosses).

Chapter 5

Impact of carotid stent cell design on vessel scaffolding: a case study comparing experimental investigation and numerical simulations

5.1 Introduction

A recent statistic report of the American Heart Association [1] highlights the huge social and economical cost due to stroke; in this scenario, carotid artery (CA) stenosis has 2%-8% prevalence, representing a relevant portion of the 6.400.000 strokes that occur each year.

Treatment of carotid stenosis is aimed at the prevention of ischemic events caused either by direct hemodynamic impairment or, more commonly, by embolization of thromboembolic material. Currently two main treatment options are available: i) carotid endarterectomy (CEA); ii) carotid artery stenting (CAS). CEA is a surgical procedure which removes the atherosclerotic plaque, accumulated inside the internal carotid artery (ICA); CAS is a minimally-invasive intervention, aiming to restore the vessel patency performing an angioplasty followed by stent apposition, hence leaving the

plaque contained between the stent and the vessel wall.

Despite CEA is still considered the golden standard to treat carotid stenosis, CAS has emerged as a safe and cost-effective alternative to CEA, however, especially for symptomatic¹ patients, the results of randomized clinical trials about its efficacy are conflicting [36, 126, 127], as also confirmed by systematic review of clinical trials comparing CAS and CEA performed by Brahmanandam et al. [64]. Moreover, very recently, the results of CREST clinical trial [12] indicate that for both patients with symptomatic or asymptomatic carotid stenosis, the risk of the composite² primary outcome of stroke, myocardial infarction, or death did not differ significantly in the group undergoing CAS and the group undergoing CEA; it seems plausible that an important clinical debate will arise after this study [13].

Several studies [95, 129, 130, 131, 132] support the use of CAS, but, at the same time, they underline the importance of technical skills, patient selection and use of dedicated devices (i.e. guidewires, stents and embolic protection devices - EPDs) to improve the CAS outcomes; in fact many different designs of both stents and EPDs, available on the rapidly growing dedicated market, are enlarging the interventional options complicating the standardization of the treatment strategy, relating thus the CAS success to the ability of the operator [15].

In particular with respect to carotid stent design, the importance of stent cell design (i.e. *closed* versus *open*) and vessel scaffolding³ for CAS clinical outcomes is a matter of debate [24, 133, 134, 135, 136].

In 2006, Hart et al. [136] performed a retrospective study based on a dual-center CAS database to identify patient and procedural parameters, which have a negative impact on the 30-day post-procedure complications (i.e.

¹Symptomatic patients are usually defined as individuals with transient ischemic attacks (TIAs), unilateral transient monocular blindness (amaurosis fugax), or non-disabling stroke on the same side as the carotid artery stenosis

²An interesting paper on the impact of using composite outcomes in clinical trials with a focus in cardiovascular area is provided by Lim et al. [128]

³Vessel scaffolding is the stent capability to support the vessel wall after stenting; in particular, the mesh structure of the stent has to guarantee that no debris is dislodged through its interstices. Usually the amount of vessel scaffolding is determined by the free cell area and a common way to relate the free cell area with the stent design is to classify it as *open-* and *closed-cell* design; such a classification is based on the number and arrangement of bridge connectors: in *closed-cell* stents, adjacent ring segments are connected at every possible junction; in *open-cell* stents not all of the junction points are interconnected. With respect to the same pattern, a *closed-cell* stent design has a smaller cell area than its correspondent *open-cell* counterpart.

stroke, death and transient ischemic attack - TIA). The analysis indicated that: i) TIA should be taken into account to achieve statistical significance; ii) patient treated with *closed-cell* stents have a lower risk to experience post-procedure adverse events, when compared with the patients treated with *open-cell* design. The authors speculated that, since TIA is related to small particles passing through the stent mesh, the positive outcomes obtained using *closed-cell* stents are due to their smaller free cell area and thus to their intrinsically higher capability to scaffold the emboligenic CAS lesion.

With a similar goal, one year later, Bosiers et al. [24] performed a retrospective analysis of a CAS database resulting from four clinical centers; in particular, the authors focused on the influence of stent free cell area. The results confirmed the conclusions proposed by Hart et al. [136], showing that post-procedural complication rates are higher for the *open-cell* stent types, especially for symptomatic patients, and increase with larger free cell area. Consequently, the authors speculated that stents with a smaller free cell area contain better the plaque material behind the struts, resulting in significant differences in event rates compared to stents with large free cell areas [26].

The previous indications are somehow in contrast with the data provided by Schillinger et al. [135], who investigated the impact of *closed-* versus *open-cell* stent design on neurologic adverse events and mortality, through a retrospective analysis of CAS database from ten European clinical centers; in fact, the results indicated no superiority of a specific carotid stent cell design with respect to neurologic complications, stroke, and mortality risk. The contradiction between the cited studies and the different approaches used for data analysis have been further discussed [133, 134], highlighting the need of dedicated clinical studies and of stent design optimization.

Besides the cited clinical investigations, few studies are available on the role of stent cell design on CAS or more generally on stent mechanics itself. Tanaka et al. [137] evaluated five different types of self-expanding carotid stents implanted into simplified pulsatile perfused silicone models of a carotid bifurcation, highlighting the superior conformability⁴ of the

⁴Stent conformability is the stent ability to adapt to the vessel tortuosity and it is clearly related to the stent flexibility, which is an intrinsic property of the design. With respect to flexibility, *open-cell* stents are more flexible than their *closed-cell* counterparts since in the *closed-cell* stent there is a large quantity of connections between adjacent ring segments and, therefore, the degree of flexibility between these segments is limited.

laser-cut *open-cell* designs with respect to braided *closed-cell* design. More recently, Müller-Hülsbeck et al. [138] have examined and compared different carotid stent designs with regard to flexibility, conformability to the vessel, and scaffolding to reduce plaque prolapse and embolization; the authors stressed the benefits of combining the properties of cell variants in an hybrid stent design having the flexibility of an *open-cell* structure and the resistance to particle penetration of *closed-cell* structures. In another experimental study, Carnelli et al. [22] have measured bending and radial stiffness of six carotid *open-cell* self-expandable stents showing very different geometrical features and mechanical properties despite similar material and a common *open-cell* structure. Sieworek et al. [139] have underlined, in a review paper, the clinical significance and technical assessment of stent cell geometry for CAS.

All the above cited studies indicate the need of dedicated tools to quantitatively evaluate the impact of carotid stent cell design on the vessel scaffolding; for this reason, in the present study, we propose the use of patient-specific finite element analysis (FEA) of CAS to virtually evaluate the impact of stent cell design on the vessel scaffolding.

We organize the study in two main steps, as described in the following:

1. Validation of patient-specific FEA of CAS
 - generation of a compliant silicon patient-specific CA mock artery based on CTA medical images;
 - micro-CT scanning of silicon mock artery and generation of the corresponding finite element mesh;
 - micro-CT scanning of the *open-cell* stent and generation of the related finite element mesh;
 - micro-CT scanning of the *open-cell* stent deployed in the silicon mock artery and 3D reconstruction of the final stent/artery configuration;
 - performance of numerical simulation of the *open-cell* stent deployment in the artery model;
 - comparison of the experimental and numerical results;
2. Vessel scaffolding evaluation
 - performance of numerical simulation of the *closed-cell* stent deployment in the artery model;

- evaluation of the cell design impact on the stent strut distribution in different vessel cross-sections as a measure of scaffolding.

5.2 Materials and Methods

5.2.1 Validation of patient-specific finite element analysis of carotid artery stenting

From Computed Tomography Angiography to CA silicon model

Silicon mock arteries are used in medical device testing to evaluate performance of vascular devices [140, 141, 142] and clinician training [143] without performing animal or human clinical studies. With respect to CAS, several in-vitro studies [23, 43, 48, 49, 50, 57, 139, 144] use CA silicon models to evaluate the EPD efficacy while a very limited number of works dealt with CA stent apposition itself: in addition to the study of Tanaka et al. [137], previously described, Suzuki et al. [145] proposed the use of silicon CA models, based on the images of clinical case, to simulate the endovascular procedure for interventional training.

Given the goal of our study, we want to reproduce a realistic carotid artery anatomy and consequently we base the generation of the silicon mock artery on computed tomography angiography (CTA) images. We process the images as previously described in previous chapter using Mimics v.13 (Materialise, Leuven, Belgium) obtaining a stereolithographic (STL) description of the artery lumen as shown in figure 5.1. The obtained STL is used to fabricate an anatomically accurate silicon CA (Advanced Vascular Models, Seaside, CA, USA); the model has variable wall thickness (see figure 5.1-c) to ensure a 5% radial compliance during a diastolic-systolic pressure cycle in the stenting region as suggested by the standard Dynatek delta [146].

Carotid artery finite element model

As the silicon mock artery has a variable wall thickness, we base the generation of finite element model of the vessel on micro-CT scan of the sole silicon model, performed before the stent deployment. Using Mimics, we firstly imported the scan images, we then performed a segmentation limiting the size of the model considering a portion with a length of 41.94 mm (see figure 5.2-a); we finally create a finite element mesh defined by 73322

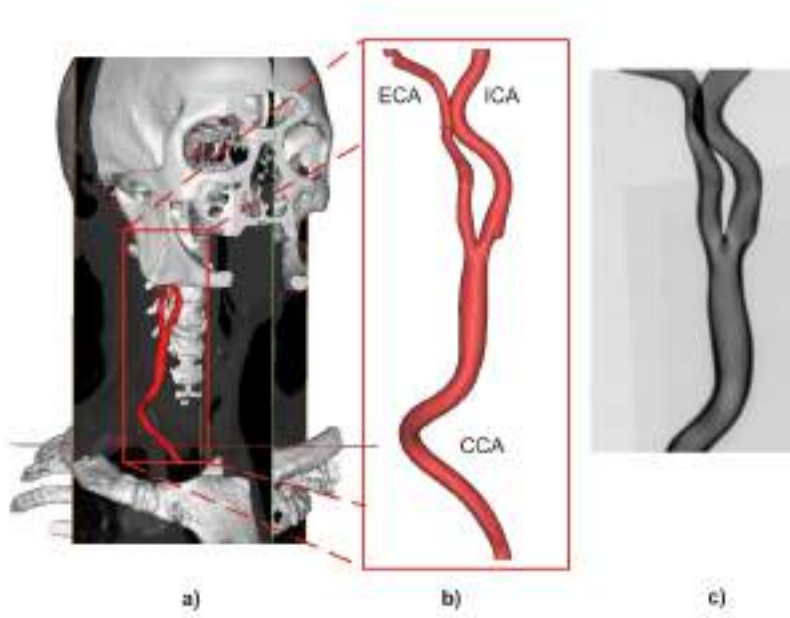


Figure 5.1: CA model: a) 3D reconstruction of cerebral vascular tree from CTA; b) surface describing the CA lumen used to create the silicon artery; c) radiography of the silicon artery highlighting the non-uniform wall thickness.

10-node modified tetrahedron, with hourglass control (C3D10M) elements and 134092 nodes using the available remeshing capabilities of Mimics.

We model the silicon as an hyperelastic material using a second order polynomial strain energy potential U defined as:

$$U = \sum_{i+j=1}^2 C_{ij} (\bar{I}_1 - 3)^i (\bar{I}_2 - 3)^j + \sum_{i=1}^2 \frac{1}{D_i} (J^{el} - 1)^{2i} \quad (5.1)$$

where C_{ij} and D_i are material parameters; \bar{I}_1 and \bar{I}_2 are respectively the first and second deviatoric strain invariants. To calibrate the material model, we fit the stress-strain data (see figure 5.2-b), obtained by ISO 37:2005 test on silicone sample, obtaining the following non-null coefficients: $C_{10} = -2.40301$ MPa; $C_{01} = 3.02354$ MPa; $C_{20} = 0.456287$ MPa; $C_{11} = -1.72892$ MPa; $C_{02} = 2.73598$ MPa.

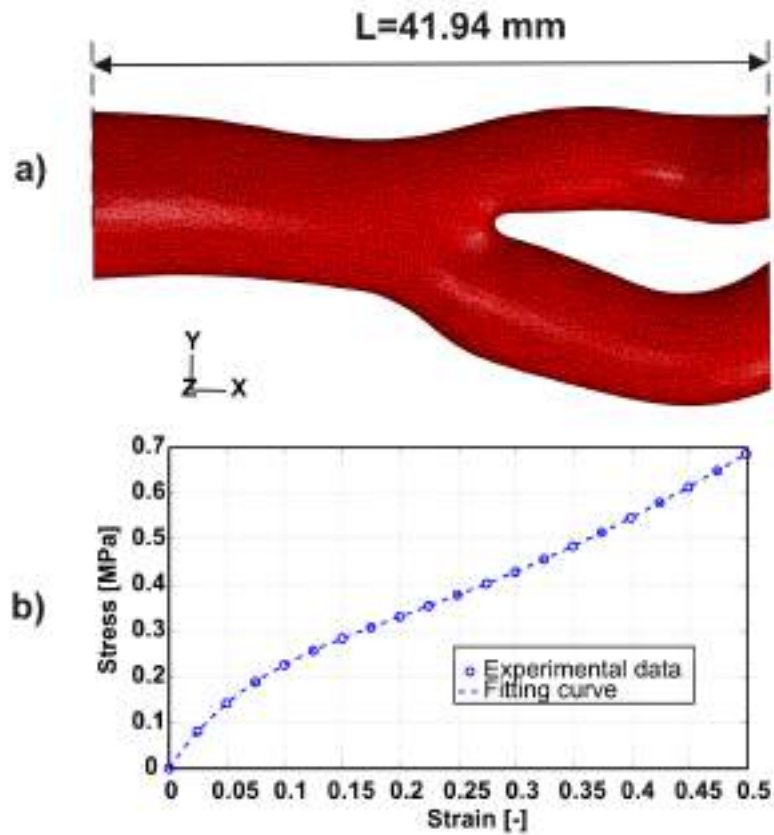


Figure 5.2: a) 3D reconstruction (triangulated surface) of pre-stenting silicon artery; b) adopted stress-strain curve for silicon material and related data fitting curve.)

Stent finite element model

For the experimental stent deployment in the silicon CA we use a 9mm Bard ViVEXX Carotid Stent (C. R. Bard Angiomed GmbH & Co., Germany), an *open-cell* self-expanding nitinol stent with a straight configuration.

An effective simulation of the self-expanding stent deployment has to take into account an accurate representation of the actual stent geometry which

is the result of several steps along the manufacturing process [147, 148, 149] which can be resumed as follows:

- *laser-cutting*: the stent design is laser-cut from a low profile Nitinol tube;
- *shape-setting*: the laser-cut configuration is expanded by the insertion of a rigid expander;
- *annealing*: the new expanded geometry is thermically treated in order to set the superelastic properties;
- *crimping and deployment*: the superelastic expanded stent is crimped into the delivery system and subsequently released in the artery.

Given the previous considerations, we generate the stent finite element model as follows:

- we create the mesh of the stent as it appears after the *laser-cutting*; since no data are available from the manufacturer, the mesh is based on the micro-CT of stent crimped in the delivery, under the hypothesis that these two configurations are similar;
- we use this mesh to perform FEA of *shape-setting*, leading from the laser-cut to the expanded configuration, using Abaqus/Explicit v. 6.9 (Dassault Systèmes, Providence, RI, USA) as finite element solver.

We perform two micro-CT scans of the stent in the delivery system to assess the actual geometry of the stent: i) a low resolution scan, i.e. 20 μm , of the whole stent; ii) an high-resolution scan, i.e. 5 μm , of a stent part (see figure 5.3-a). We then import the planar slices obtained from the micro-CT scans in Mimics v.13 (Materialise, Leuven, Belgium) to reconstruct the 3D configuration of crimped stent (in STL format). The STL file is then imported in pyformex [52] and virtually unrolled, serving as a reference for the generation of the planar mesh of the stent; through appropriate geometrical transformations, the planar mesh leads to the final *laser-cut* stent mesh [150]. The stent has diameter of 1.25 mm and a strut thickness of 0.190 mm; these values are measured on high-resolution micro-CT scan images using ImageJ (<http://rsbweb.nih.gov/ij/>). The finite element model of the *laser-cut* stent model consists in 44460 8-node linear brick, reduced integration with hourglass control (C3D8R) elements and 82890 nodes.

We simulate the *shape-setting* process assuming that the stent diameter enlargement is driven by a rigid expander having an initial cylindrical shape (0.775 mm initial diameter and 33 mm length). The expander mesh consists of 800 three-dimensional, 4-node surface elements with reduced integration (SFM3D4R). We perform the FEA controlling the expander by appropriate boundary conditions on its nodes imposing a radial displacement of 3.91 mm in order to obtain an outer stent diameter of 9 mm. Prior to annealing, the mechanical behavior of cold-worked Nitinol is similar to metals like aluminum or classic steel; consequently for these simulations we model Nitinol as an elasto-plastic material using the material parameters based on the work of Thériault et al. [148]. We use a frictionless general contact algorithm in order to handle the interactions between the rigid cylinder and the stent. The result of *shape-setting* simulation is reported in figure 5.3-b.

The use of finite element modeling, and in particular of pyformex as pre-processing tool, facilitates the performance of parametric analyses [47]; in this study, we exploit such a capability modifying original *open-cell* design (figure 5.4-a) by increasing the original number of connectors from 5 to 15 in order to define the *closed-cell* counterpart (figure 5.4-b).

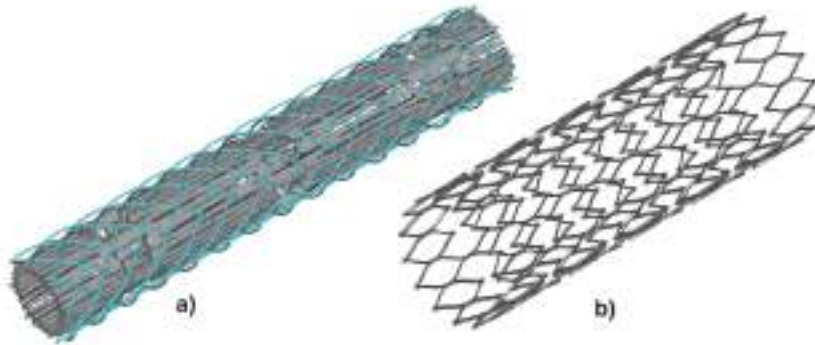


Figure 5.3: a) 3D reconstruction of part, i.e. 8.45 mm, of the stent (in grey) within the catheter (in blue); b) finite element model of *open-cell* stent after *shape-setting* simulation.

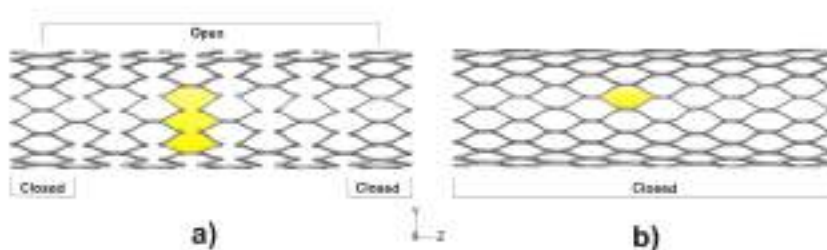


Figure 5.4: Details about the cell arrangement for the a) *open-* and b) *closed-cell* design under investigation (the standard free cell area is highlighted in yellow).

Stent deployment: experimental test

We fix the silicon artery on a support stitching the branch ends (see figure 5.5-a). We perform a preliminary micro-CT of the sole silicon artery with a resolution of 0.053 mm to get an accurate representation of the pre-stenting artery model. We then introduce the stent delivery system, previously lubricated to avoid friction during the apposition, taking radiographic images during the step-by-step deployment process (see figure 5.5(b-c)). Nitinol self-expanding stents are designed to work in an isothermal environment at 37 °C but we perform the test at room temperature, i.e. about 22 °C, thus we use a local heating, through air fan, to induce the full recovery of the expanded stent configuration and its complete deployment. Finally we perform another micro-CT scan with a resolution of 0.053 mm to get an accurate representation of the post-stenting artery/stent configuration. We process initial and final micro-CT scan images of silicon artery using Mimics obtaining 3D reconstructions depicted in figure 5.5-d.

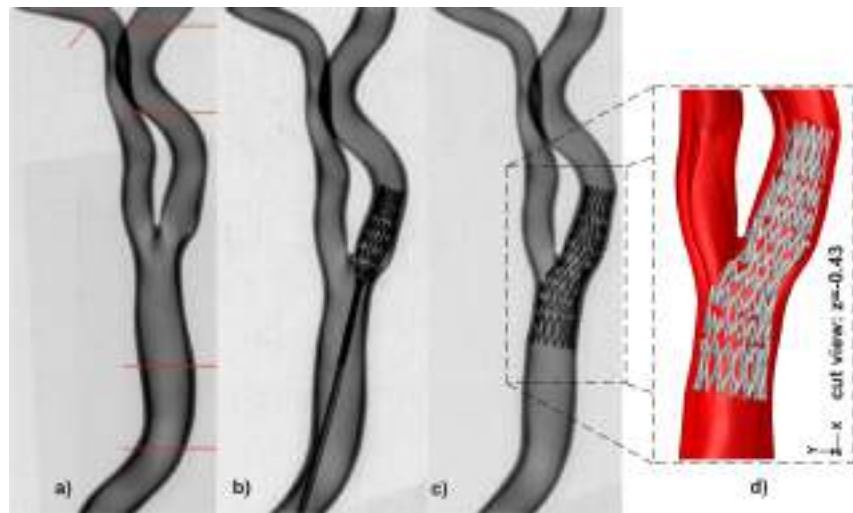


Figure 5.5: a) silicon artery, red lines indicate the location of restraints; b) silicon artery and partially-deployed stent; c) silicon artery and fully-deployed stent.

Stent deployment: numerical simulation

To simulate the stent deployment in the silicon artery, we use the approach already described in the previous chapter (see section 3.2.3).

Post-processing

In order to validate the numerical simulation of stent deployment in the patient-specific CA anatomy, by the qualitative point of view, we compare the stent/vessel configuration, obtained at the end of simulation, with the 3D reconstruction of the experimental counterpart.

By quantitative point of view, we compare the circumferential distribution of the stent struts along three defined vessel cross-sections (i.e. one at common carotid artery - CCA, one at the bifurcation, one at internal carotid artery - ICA) measuring the inter-strut angle⁵, enclosed between adjacent struts as depicted in figure 5.6.

5.2.2 Vessel scaffolding evaluation

The ability of a certain stent design to scaffold the vessel wall after stenting depends by several inter-related factors but, clearly, the design itself has a primary role. The vessel scaffolding is not a trivial measure neither to standardize nor to measure. Usually the amount of vessel scaffolding is determined computing by the free cell area of the free-expanded stent [138], despite such approach is useful to compare different designs, it does not provide the actual scaffolding measure of the implanted stent. In this study we decide to use the inter-strut angle at different vessel cross-sections as a measure of scaffolding as this method is closer to the actual clinical evaluation criteria [151]. Consequently, performing the post-processing of the numerical simulations for both *open-cell* and *closed-cell* design, we measure the maximum inter-struts angle in five different vessel cross-sections of the CA, as depicted in figure 5.8.

⁵Inter-strut angle is defined as the angle created between two lines passing from the centre of gravity of the bounding-box of the stent cross-section, to the clockwise side of two consecutive struts.

5.3 Results

5.3.1 Validation of patient-specific finite element analysis of carotid artery stenting

In figure 5.6 the stent/vessel configuration in the case of *open-cell* design for both experimental test and numerical analysis is depicted⁶; while in table 5.1, the inter-strut angle for the section close to the CA bifurcation is reported.

The qualitative comparison between the 3D reconstruction obtained from the micro-CT images and the numerical results provides a good agreement, which is also confirmed by the substantial match between the inter-strut angles reported in table 5.1.

Figure 5.6 shows also the so-called *fish-scaling* effect: the stent cell opening, related to the bending due to the angulated CA bifurcation, causes a misalignment and protrusion of the stent struts on the open surface, which can result in intimal disruption with contrast die extending to the adventitia [139]; whether the interaction of the stent struts with the vessel wall can predispose to restenosis or stent fracture is a still matter of concern [152].

Table 5.1: FEA of CAS validation: inter-strut angles for the section 2 depicted in figure 5.6.

Angles [°]	θ_1	θ_2	θ_3
Experimental test	72.3	28.8	26.3
Numerical analysis	82.8	29.6	32.9
$\Delta\theta$ [°]	+10.5	+0.8	+6.6

⁶The figure highlights the strut position at three section (sec. 1: x=10 mm; sec. 2: x=19 mm; sec. 3: x=30 mm) and the deformation of stent cells from a virtual view through the ECA. Note that the apparent mismatch of the stent strut thickness between the experimental and numerical results is only due to blooming artifacts in the microCT images.

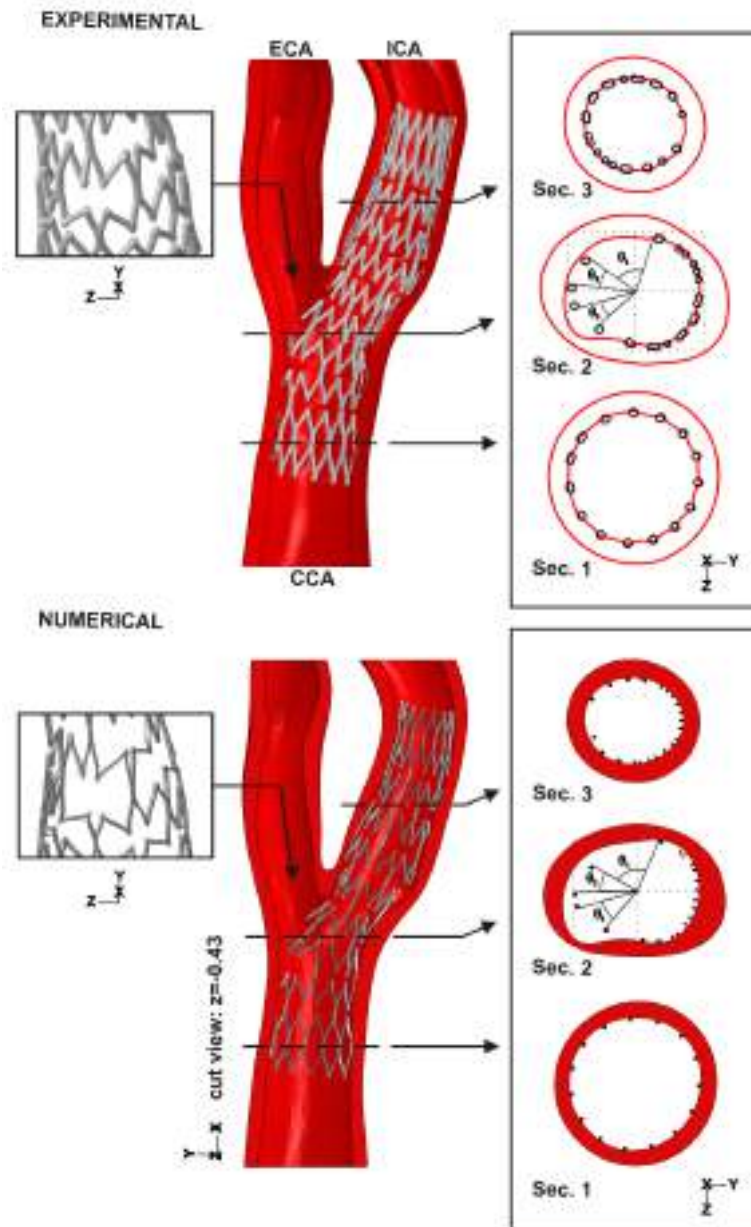


Figure 5.6: Comparison between experimental (on top) and numerical (on bottom) stent/vessel configuration.

5.3.2 Vessel scaffolding evaluation

In figure 5.7 the stent/vessel configuration obtained by the numerical analysis, for both *open-cell* and *closed-cell* design, is illustrated. It is possible to notice that in the *closed-cell* case the full connection between the rings, on the one hand, allows the maintenance of the tubular shape, while, on the other hand, restricts the stent capability to accomplish the irregular eccentric profile of the vessel cross-section above the stenosis as highlighted in figure 5.7-5.8.

The measurement of inter-strut angles reported in table 5.2 and the strut distribution depicted in figure 5.8 suggest that:

- *open-cell* design provides the higher maximum value, in every section, when compared to the *closed-cell* design; this effect is particularly evident in the first three sections, corresponding to the vessel segment above the bifurcation when the bending angle is higher and the vessel cross-section irregular;
- *open-cell* design provides the higher standard deviation, in every section, when compared to the *closed-cell* design, which thus ensures a more uniform circumferential distribution of the struts.

Table 5.2: *Open-cell vs closed-cell:* inter-strut angles for the sections depicted in figure 5.8.

Cell Design	<i>Open-cell</i>		<i>Closed-cell</i>	
	Max	Mean±STD	Max	Mean±STD
Section 1	74	46.3±28.2	23.9	19.6±2.1
Section 2	69	43±24	26.5	19.5±3.3
Section 3	67.3	24.7±14.7	25.2	19.5±3.6
Section 4	25.8	17.8±4.5	25.1	18.7±3.6
Section 5	36.5	18.3±5.2	24.3	18.5±2.7

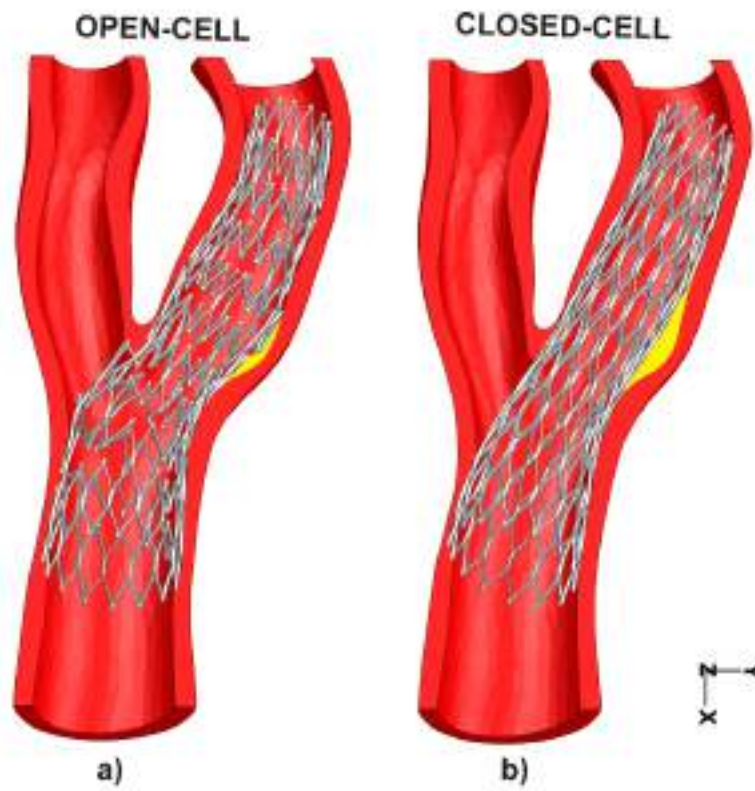


Figure 5.7: Stent/vessel configuration obtained by FEA of CAS: a) *open-cell* design; b) *closed-cell* design. The gap between the stent and the vessel wall is highlighted in yellow.

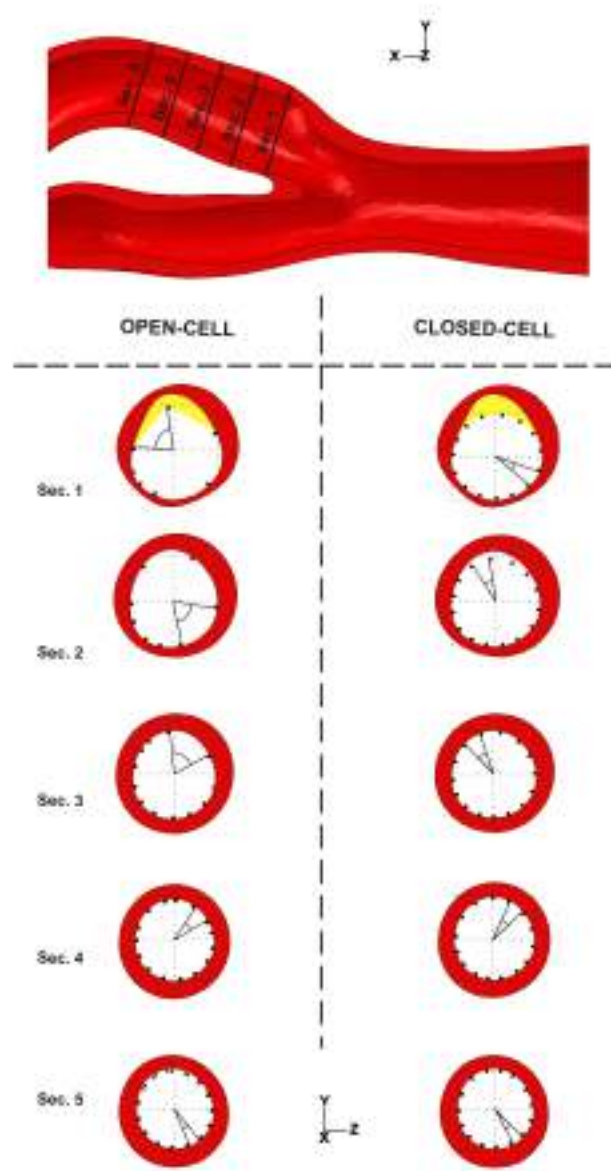


Figure 5.8: Cut views of five different vessel cross-sections for both *open-cell* design (on left) and *closed-cell* design (on right). The section position is illustrated with respect to pre-stenting vessel (on top) and for each section the maximum inter-strut angle is depicted. Moreover the gap between the stent and the vessel wall is highlighted in yellow.

5.4 Limitations

Despite we validate our numerical results performing also the experimental deployment of a real carotid stent in an accurate CA anatomy model, some limitations affects the present study and are related to the following items: i) two variants of only one stent are taken into account; ii) the inter-strut angle is measured at five given sections. To generalize the results other several devices should be tested also with respect to other CA anatomies.

5.5 Conclusions

In most cases, CAS post-procedural complications are related to late emboli through the stent struts; for this reason, clinicians' concerns is now turned on the capability of a certain stent design to provide sufficient vessel scaffolding in order to avoid the plaque protrusion and the related embolization through the stent struts, as underlined by the clinical debate on the role of the stent cell design on the post-procedural adverse events. Usually the vessel scaffolding is quantified calculating the maximum free cell area of a given stent design in free expanded configuration; despite this measure is appropriate for comparison purpose, a more accurate measure should take into account the actual current configuration of the stent implanted in the tortuous CA bifurcation. In this study we exploit FEA to perform the simulation of CAS for two design variants, i.e. *open-cell* and *closed-cell*, of the same stent and compute the inter-strut angle in different vessel cross-sections as a measure of scaffolding. Moreover we validate the results of the CAS simulation comparing the numerical results with the micro-CT images of the stent implanted in a patient-specific silicone mock artery. The results indicate that *closed-cell* design provides a more uniform circumferential strut distribution in every section of the stented segment when compared to *open-cell* counterpart, which experiences also the so called *fish-scaling* effect due to the CA bifurcation bending. As expected the *closed-cell* design seems to ensure a superior vessel scaffolding, but it is necessary to highlight that its full strut interconnection reduces the stent ability to accomplish irregular eccentric profile of the vessel cross-section, leading to a gap between the stent surface a vessel wall.

Bearing in mind the discussed limitations, the present study provides a quantitative approach to assess the vessel scaffolding of a given stent design

Chapter 5. Impact of carotid stent cell design on vessel scaffolding: a case study comparing experimental investigation and numerical simulations

in a patient-specific CA anatomy, confirming the capability of dedicated FEA to predict non-invasively differences in scaffolding by open-cell and closed-cell stents typically used for CAS.

Chapter 6

Final remarks

The research activity described in this dissertation can be collocated in the area of computational biomechanics, as it exploits methods of computational mechanics, i.e. finite element analysis (FEA), to investigate several aspects of carotid artery stenting (CAS), a minimally invasive clinical procedure.

The application of such multidisciplinary approach has highlighted the usefulness of using the simulations for both device evaluation and procedure planning. In this chapter we briefly resume the obtained results to finally discuss the corresponding further developments.

6.1 Conclusions

Chapter 2 - Nitinol embolic protection filters: design investigation by finite element analysis

The study highlights the role of filter design on its capability to adapt to the vessel wall; in fact, these devices appear to have a significant impact on the success of CAS but, unfortunately, some drawbacks, such as filtering failure, inability to cross tortuous high-grade stenoses, malpositioning and vessel injury, still remain and require design improvement. We first develop a parametrical computer-aided design model of an embolic filter based on micro-CT scans of the Angioguard XP (Cordis Endovascular, FL) EPD by means of the open source pyFormex software. Subsequently, we used the

finite element method to simulate the deployment of the Nitinol filter as it exits the delivery sheath. Comparison of the simulations with micro-CT images of the real device exiting the catheter showed excellent correspondence with our simulations. Finally, we evaluated circumferential basket-vessel wall apposition of a 4 mm size filter in a straight vessel of different sizes and shape. We conclude that the proposed methodology offers a useful tool to evaluate and to compare current or new designs of embolic protection filters.

Chapter 3 - Carotid artery stenting simulation: from patient-specific images to finite element analysis

The study aims to evaluate the impact of different stent designs on a single vessel anatomy. Accordingly in this study, we use finite element analysis to evaluate the performance of three self-expanding stent designs (laser-cut open-cell, laser-cut closed-cell, braided closed-cell) in a carotid artery (CA). We define six stent models considering the three designs in different sizes and configurations (i.e. straight and tapered), evaluating the stress induced in the vessel wall, the lumen gain and the vessel straightening in a patient-specific CA model based on computed angiography tomography (CTA) images. For the considered vascular anatomy and stents, the results suggest that: i) the laser-cut closed-cell design provides a higher lumen gain; ii) the impact of the stent configuration and of the stent oversizing is negligible with respect to the lumen gain and relevant with respect to the stress induced in the vessel wall; iii) stent design, configuration and size have a limited impact on the vessel straightening. The presented numerical model represents a first step towards a quantitative assessment of the relation between a given carotid stent design and a given patient-specific CA anatomy.

Chapter 4 - Patient-specific finite element analysis of carotid artery stenting: a focus on the vessel modeling

The study investigates the impact of carotid stent apposition on CA wall stress distribution through patient-specific finite element analysis; in particular, we focus on the influence of constitutive vessel modeling on the predicted tensional state over the CA wall. The results highlight the wide variability of the computed stress with respect to adopted constitutive models underlying so the role of an appropriate vessel modeling with respect to

the deductions drawn from numerical simulation of stenting. From a more general point of view, since FEA is nowadays a well-assessed technique to investigate the impact of stenting on vessel wall and given the rapid progression of both medical imaging techniques and computational methods, the challenge of using FEA of CAS as procedure planning tool supporting the clinical practice can be tackled. Following this idea, although the highlighted limitations, the present study represents a further step toward a realistic simulation of CAS.

Chapter 5 - Impact of carotid stent cell design on vessel scaffolding: a case study comparing experimental investigation and numerical simulations

The study proposes the use of FEA combined with image-based patient-specific modelling to assess the impact of stent cell type (open vs closed) on vessel scaffolding in a realistic case of carotid artery stenting (CAS). In a first step, a methodological validation of FEA of CAS is carried out against experimental data. An open-cell stent is deployed both in a patient-specific silicon mock artery (physical model) and in a patient-specific finite element model (virtual model). The post-implantation 3D geometry of the physical model is then imaged with a micro-CT scanner and compared to the deformed configuration predicted by the virtual model. This validated methodology is then applied to quantify the vessel scaffolding obtained with the same stent design in open- and closed-cell configuration, using the cross-sectional stent strut distribution (inter-strut angle) as term for comparison. The virtual model matches the physical model both qualitatively (vessel shape) and quantitatively (inter-strut angles), supporting the reliability of the FEA for CAS simulation. The numerical analysis predicts that the cell type influences the outcomes of CAS with respect to vessel scaffolding: i) the closed-cell stent provides a more uniform circumferential stent-strut distribution in each cross-section of the stented region; ii) the open-cell stent experiences the fish-scaling effect, due to bending in the bifurcation region; iii) the closed-cell stent fails to accomplish the vessel cross-section in case of irregular eccentric profile, leading to gaps between the stent surface a vessel wall. Although the investigation is limited to a single vessel/stent combination, the proposed methodology represents a validated tool to query the vessel scaffolding of CAS, and may be used as objective clinical image-based

evaluation for optimal prosthesis selection.

In conclusion, the main achievements of the research activities described in this dissertation are: i) the development of realistic simulation strategies allowing to study complex CAS devices and their interaction with the vessel; ii) the new insights into the performance and on the shortcomings of currently applied techniques; iii) the objective comparison of existing stent designs; iv) the application of patient-specific modelling (morphological and constitutive) in the field of carotid artery stenting. The investigation approach discussed in this dissertation is certainly multidisciplinary, as it based on computational methods applied to clinical issues, and consequently also the evaluation criterion of the reported results should be multidisciplinary. From an engineering point of view, FEA is already a well-assessed simulation tool while, from medical point of view, the operator skills and experience guide the choice of a certain treatment for a certain patient, since human body is a complex system and as system it should be considered. If we move from such considerations the discussed research activities can be considered as accurate engineering simulations or the quantitative confirmation of the clinical evidence; instead, bearing in mind the multidisciplinary nature of the proposed studies, each of the previous chapters can be considered as a contribution to integration process between the computational tools and clinical practice, in order to support the procedure standardization.

6.2 Future works

The findings and methods proposed in dissertation can be used as a starting point for further research developments; in particular, in the following we will briefly discuss the open issues in the challenge of using patient-specific simulation of CAS as procedure planning tool in clinical practice.

A patient-specific simulation of CAS which can be exploited in the daily clinical routine should be fast, reliable and open to a clinical operator; such requirements can be satisfied only limiting the amount of time required by:

- pre-processing: generation of vascular model from medical images, assigning material properties, assembling the FE model, etc.;
- simulation: performance of the numerical analysis through an appro-

priate numerical solver;

- post-processing: elaboration of the simulation outputs extracting few scalar values representing the clinical information required by the operator.

With respect to pre-processing, current medical imaging and related elaboration softwares can provide accurate tridimensional reconstructions of the vascular anatomies [2], which can be further elaborated with (semi)automatic procedure to create patient-specific computational grid [70, 71, 153, 154], consequently patient-specific vascular modeling can be considered feasible and applied to populations of subjects.

Unfortunately, patient-specific modeling is still confined to the anatomical features as the patient-specific characterization of the vessel mechanical behavior is still far to be addressed; few studies in literature are dealing with in-vivo measurements of mechanical properties and further effort is required to obtain accurate indication on the patient-specific mechanical properties. A possible solution is to combine each anatomy with multiple sets of material data, defining thus a number of variants in order to get an indication on the interval of confidence of the numerical outputs, as suggested in chapter 3. Once the patient-specific geometry model is defined and the material properties assigned, the assembling of final finite element model including the self-expanding stent and catheter model can be approached as suggested in chapter 3. In this stage the input of the operator would be only related to: i) evaluation and approval of the vascular model obtained by automatic medical image elaboration; ii) selection from a predefined stent “library” of the stent designs to evaluate.

Given the FE model, the analysis performance requires a stable solver able to manage large models; this is not a real issue since FEA is a well-established step of the industrial design process and consequently several commercial (or open-source) FEA solvers are nowadays available; moreover most of them are already suited for multi-processing, which is the basic requirements to manage large models. The real bottle-neck appears to be the computational cost of the analysis itself; in fact, our experience suggests to consider the simulation of CAS as a quasi-static analysis approached by explicit integration scheme. This approach, on the one hand, allows to manage the non linearities due to contact, material modeling and large deformations but, on the other hand, has a drawback related to both computational time

and inertial forces. In fact, the stable time increment, Δt , of the integration scheme is dependent on both the smallest characteristic mesh dimension and the dilatational wave speed; Δt is often very small when compared to the total simulation time and this aspect for large models can lead to very high computational cost. Both reduction of the time step or scaling the system mass can be a solution to reduce the computational cost with such an explicit dynamic procedure, but inertial forces can arise. Consequently the optimal solution is a trade-off between computational cost and analysis accuracy; for our experience, the amount of time required to perform a CAS simulation is still high even if exploiting high-performance computer and process parallelization. A promising option to overcome such issue is a new numerical technique, the so-called isogeometric analysis (IGA) [155], as it reduces the computational cost providing accurate results using less degree of freedom when compared to classical FEA. Moreover IGA, thanks to integration between CAD and numerical analysis, can speed-up the pre-processing step.

Once the simulation is done, the numerical results should be elaborated to provide a set of scalar quantities representing the information desired from the clinical operator, as discussed in chapter 3.

Finally, in our opinion the integration between computational biomechanics and clinical practice can become reality, but this challenge can be approached only if a close interaction between surgeons, radiologists and engineers will be further promoted.

List of Figures

1.1	Representations of carotid artery vascular anatomy: a) illustrative scheme and b) 3D reconstruction from Computed Tomographic Angiography (CTA) of a normal aortic arch and its great vessels and branches (adapted from [2]); c) anatomical illustration of the head vascular tree (adapted from [3]); d) Anterior view of carotid artery anatomy reconstructed from CTA: carotid bulb (white asterisk), <i>A</i> : Right brachiocephalic artery, <i>B</i> : Right subclavian artery, <i>C</i> : Right common carotid artery (CCA), <i>D</i> : Right internal carotid artery (ICA), <i>E</i> : Right external carotid artery (ECA), <i>F</i> : Right vertebral artery.	3
1.2	Illustrative representation of the main steps of atherosclerosis disease progression. Adapted from [4].	5
1.3	Schematic illustration of carotid artery bifurcation with internal carotid artery (ICA) stenosis illustrating the three different measurement methods.	8
1.4	Carotid endarterectomy (CEA): a) the plaque has been separated from the outer wall of the common carotid artery (CCA) and external carotid artery (ECA) and is now being removed from the internal carotid artery; b) Arteriotomy closure; sutures are placed at the distal end of the arteriotomy with particular attention to suture both intimal and wall layers on both sides. Adapted from [5].	10

1.5	Carotid angioplasty and stenting. a) Guide catheter (not shown) is placed in the CCA proximal to the stenosis. Through this catheter, a filter wire is used to cross the stenosis and deploy an embolic protection filter (EPF) in the ICA distal to the plaque. The filter captures emboli dislodged during the procedure. b) pre-dilation of the plaque is performed with an angioplasty balloon, followed by c) stent deployment; occasionally, angioplasty may be necessary after stenting to further dilate residual stenosis. d) the filter is withdrawn into the guide catheter. The procedure is done with full heparinization. Patients receive maintenance dual antiplatelet therapy, usually aspirin plus clopidogrel, for at least 4 to 6 weeks. Adapted from [25].	14
1.6	Work-flow of the virtual framework to assess the stent performance in a given patient-specific carotid artery anatomy: starting from medical images, we develop the patient-specific CA model; we combine the vessel model with a given stent model available within a predefined stent design library to perform a simulation of CAS through FEA; the results are elaborated to assess clinically relevant parameters of stenting performance (e.g. lumen gain or vessel straightening). The framework allows to investigate virtual scenarios and to perform an evaluation loop aiming at supporting the CAS procedure planning.	17
2.1	The Angioguard XP™ embolic protection device.	23
2.2	Example of filter model generation in four steps.	24
2.3	Typical superelastic nitinol behavior	26
2.4	Finite element model of Angioguard XP™ and part of the delivery sheath	27
2.5	Longitudinal cut view of the filter frame in the delivery sheath	30
2.6	Partially deployed filter: micro-CT image (top panel); numerical simulation (bottom panel).	30
2.7	A 4 mm size filter deployed in a 3 mm circular vessel (on the left) and in 3 mm vessel having 0.75 ovality (on the right). . .	31

3.1 Patient-specific CA model: a) 3D reconstruction of cerebral vascular tree from CTA; b) lumen of CA main branches (CCA: common carotid artery; ICA: internal carotid artery; ECA: external carotid artery) with the related analyzed sections; c) CA lumen (dark red) and reconstructed outer vessel wall profile (light red); d) hexahedral mesh.	37
3.2 Stent designs under investigation: a) Design A (straight configuration): laser-cut open-cell; b) Design C: braided closed-cell; c) Design B(straight configuration): laser-cut closed-cell; d) Design B(tapered configuration): model B2 (8-6 mm) and the oversized version model B2 (9-7 mm).	39
3.3 Example of tortuosity computation (pre-stenting vessel): given the centerline, we quantify the vessel tortuosity computing the measure $(L/D - 1)$ for the stented common carotid artery (CCA) and internal carotid artery (ICA) segment: L is the length of the centerline from the origin (point A) to the end of the stented region (point B) and D is the Euclidean distance between the two points; the tortuosity is therefore defined as the fractional increase in length of the tortuous vessel relative to a perfectly straight vessel.	41
3.4 Simulation of stent implantation for stent A1: a) starting configuration of the whole finite element model; b) stent crimped in the delivery system; c) stent deployed in the vessel.	44
3.5 a) Pre-stenting carotid artery; Post-stenting carotid artery with b) stent A1, c) stent B1 and d) stent C1. The gap between the stent and the vessel is highlighted in yellow. . . .	45
3.6 Contour plot of von Mises stress distribution (S, von MISES) in the post-stenting carotid artery with respect to the different stent models.	45
3.7 99 percentile of von Mises stress (S, von MISES) in the post-stenting carotid artery with respect to different stent models.	46
3.8 Pre- and post-stenting tortuosity (on the left) and lumen of internal carotid artery (ICA) and external carotid artery (ECA) (on the right).	46
3.9 Histograms depicting the von Mises and strain values as function of mesh density.	51

3.10 ALLKE/ALLIE ratio for both stent and vessel during the simulation.	51
4.1 Elaboration of Computed Tomography Angiography (CTA) images: a) whole 3D reconstruction of neck-head district highlighting the region of interest; b) 3D reconstruction of both lumen of left CA bifurcation and plaque (depicted in white).	57
4.2 Generation of carotid artery wall mesh: a) 3D reconstruction of vessel lumen and plaque; b) closed lines representing the inner cross-sectional profile; c) closed lines representing the inner and outer cross-sectional profiles; d) carotid artery wall mesh.	58
4.3 Representative examples of the definition of outer vessel wall profile: a) for each section, we define a local cylindrical coordinate system, which has the origin in the section center of mass; then, for each section point, we impose a radial displacement corresponding to the vessel wall thickness, which is defined as a percentage of radius (i.e. 28.19% for CCA and 32.31% for internal carotid artery (ICA) and external carotid artery (ECA) as suggested by values reported by Sommer et al. [72]) for the regions where there is no plaque, and appropriately increased for the regions where there is the plaque; b) obtained lumen (L), vessel wall (VW) and plaque (PL) respectively highlighted in red, pink and yellow; c-d) cut-view of the obtained mesh.	59
4.4 Inclusion of the plaque in the CA vessel model; the plaque (in orange) is defined assessing the elements of the vessel wall mesh (in grey) enclosed within 3D STL surface (in green) representing the plaque morphology.	60
4.5 Constitutive models and data fitting: model prediction using SEF U_A fit to experimental data reported by Delfino et al. [90].	66
4.6 Constitutive models and data fitting: model prediction using SEF U_A fit to experimental data reported by Sommer et al. [72] about a) ICA and b) CCA intact wall.	67

4.7	Constitutive models and data fitting; model prediction using SEF U_A fit to experimental data reported by Sommer et al. [72] about CCA a) media-intima (MI) and b) adventitia (ADV).	68
4.8	Constitutive models and data fitting; model prediction using SEF U_A fit to experimental data reported by Sommer et al. [72] about ICA a) media-intima (MI) and b) adventitia (ADV).	69
4.9	FEA of CAS: a) 3D reconstruction of CA lumen from CTA images; b) stent crimped in the delivery system during the simulation; c) contour plot depicting the post-stenting stress distribution over the vessel wall (model HA_1) at the end of the simulation, the cut-view option is used for the vessel and MPa is the unit of measure for stress.	75
4.10	Vessel wall stress distribution for the five considered CA models; different views of the pre-stenting configuration are shown. View 2 and view 4 are cut-views and MPa is the unit of measure for stress.	76
4.11	Stress indices for the CA wall and plaque for the considered CA models.	77
4.12	Stress indices for CA wall, ICA and CCA in case of model HA_{21} (on top); Stress indices for CA wall, ICA and CCA layers in case of model HA_{22} (on bottom)	78
4.13	a) Mesh of the CA model; b) example of local coordinate system definition; c) local cylindrical coordinate system rotation to accomplish element orientation; d) obtained collagen fiber distribution at bifurcation for MI layer (green crosses) and ADV layer (red crosses).	88
5.1	CA model: a) 3D reconstruction of cerebral vascular tree from CTA; b) surface describing the CA lumen used to create the silicon artery; c) radiography of the silicon artery highlighting the non-uniform wall thickness.	94
5.2	a) 3D reconstruction (triangulated surface) of pre-stenting silicon artery; b) adopted stress-strain curve for silicon material and related data fitting curve.)	95
5.3	a) 3D reconstruction of part, i.e. 8.45 mm, of the stent (in grey) within the catheter (in blue); b) finite element model of <i>open-cell</i> stent after <i>shape-setting</i> simulation.	97

5.4	Details about the cell arrangement for the a) <i>open-</i> and b) <i>closed-cell</i> design under investigation (the standard free cell area is highlighted in yellow).	98
5.5	a) silicon artery, red lines indicate the location of restraints; b) silicon artery and partially-deployed stent; c) silicon artery and fully-deployed stent.	99
5.6	Comparison between experimental (on top) and numerical (on bottom) stent/vessel configuration.	102
5.7	Stent/vessel configuration obtained by FEA of CAS: a) <i>open-cell</i> design; b) <i>closed-cell</i> design. The gap between the stent and the vessel wall is highlighted in yellow.	104
5.8	Cut views of five different vessel cross-sections for both <i>open-cell</i> design (on left) and <i>closed-cell</i> design (on right). The section position is illustrated with respect to pre-stenting vessel (on top) and for each section the maximum inter-strut angle is depicted. Moreover the gap between the stent and the vessel wall is highlighted in yellow.	105

List of Tables

2.1	Geometrical parameters of 4.0 mm filter model.	23
2.2	Material properties used in the simulations.	25
2.3	Numerical results of filter/vessel wall apposition.	29
3.1	Geometrical measures of the branch sections highlighted in figure 3.1.	36
3.2	Geometrical and numerical details of the considered stent models.	38
3.3	Von Mises stress (99 percentile) for each stent model at the end of the simulation.	43
3.4	Pre- and Post-stenting branch lumen and tortuosity.	43
3.5	Details on the meshes used for mesh convergence analysis.	50
3.6	Details on the meshes used for mesh convergence analysis.	50
4.1	Lumen radius and wall thickness for the internal carotid artery (ICA) and common carotid artery (CCA) section highlighted in figure 4.2. The values are reported for each section as mean \pm standard deviation.	61
4.2	Constitutive parameters of the adopted SEFs in the five model variants.	70
4.3	Stress indices for CA wall and plaque as function of CA models.	74
4.4	Stress indices for CA wall, ICA and CCA in case of model HA_{21}	74
4.5	Stress indices for CA wall, ICA and CCA layers (i.e. MI and ADV) in case of model HA_{22}	74
4.6	Mesh-convergence analysis with respect to plaque volume varying EL_{th}	85

4.7	Mesh-convergence analysis with respect to plaque volume varying EL_{circum}	85
4.8	Mesh-convergence analysis with respect to vessel wall stress varying EL_{th}	85
4.9	Mesh-convergence analysis with respect to vessel wall stress varying EL_{circum}	85
5.1	FEA of CAS validation: inter-strut angles for the section 2 depicted in figure 5.6.	101
5.2	<i>Open-cell</i> vs <i>closed-cell</i> : inter-strut angles for the sections depicted in figure 5.8.	103

Bibliography

- [1] AHA committee. Heart disease and stroke statistics 2010 update: A report from the american heart association. *Circulation*, 121:e46–e215, 2010.
- [2] R. Pelberg and W. Mazur. *Vascular CT Angiography Manual*. Springer, 2010.
- [3] F. H. Netter. *Atlas of Human Anatomy*. Saunder Elsevier, 2010.
- [4] S.J George and J. Johnson. *Atherosclerosis: Molecular and Cellular Mechanisms*. Wiley-VCK, 2010.
- [5] J. Gillard, M. Graves, T. Hatsukami, and C. Yuan. *Carotid Disease, The Role of Imaging in Diagnosis and Management*. Cambridge University Press, 2007.
- [6] NASCET trial collaborators. Beneficial effect of carotid endarterectomy in symptomatic patients with high-grade carotid stenosis. *New England Journal of Medicine*, 325:445–453, 1991.
- [7] P. M. Rothwell, C. P. Warlow, and ECST Collaborators. Prediction of benefit from carotid endarterectomy in individual patients: A risk-modelling study. *Lancet*, 353:2105–2110, 1999.
- [8] P. M. Rothwell, R.J. Gibson, J. Slattery, R.J. Sellar, and ECST Collaborators. Equivalence of measurements of carotid stenosis: a comparison of three methods on 1001 angiograms. *Stroke*, 25:2435–2439, 1994.
- [9] E.R. Bates. ACCF/SCAI/SVMB/SIR/ASITN 2007 Clinical expert Consensus Document on Carotid Stenting. *Journal of the American College of Cardiology*, 49:126–170, 2007.

- [10] Hasan Yilmaz, Vitor Mendes Pereira, Ana-Paula Narata, Roman Sztajzel, and Karl-Olof Lovblad. Carotid artery stenting: Rationale, technique, and current concepts. *European Journal of Radiology*, 75(1):12 – 22, 2010.
- [11] K.I. Paraskevas, D.P. Mikhailidis, and F.J. Veith. Mechanisms to explain the poor results of carotid artery stenting (cas) in symptomatic patients to date and options to improve cas outcomes. *Journal of Vascular Surgery*, 52(5):1367–1375, 2010.
- [12] CREST committee. Stenting versus endarterectomy for treatment of carotid-artery stenosis. *New England Journal of Medicine*, 363:11–24, 2010.
- [13] S. Davis and A. Donnan. Carotid-artery stenting in stroke prevention. *New England Journal of Medicine*, 363:80–82, 2010.
- [14] R.K. Malik, A. Vouyouka, A. Salloum, M.L. Marin, and P.L. Faries. Tips and techniques in carotid artery stenting. *Journal of Vascular Surgery*, 50:216–220, 2009.
- [15] L. Stockx. Techniques in carotid artery stenting. *European Journal of Radiology*, 60:11–13, 2006.
- [16] T.W. Duerig and M. Wholey. A comparison of balloon- and self-expanding stents. *Minimally Invasive Therapy and Allied Technologies*, 11:173–178, 2002.
- [17] M.H. Wholey, M.H. Wholey, C.R. Jarmolowski, G. Eles, D. Levy, and J. Buecthel. Endovascular stents for carotid artery occlusive disease. *Journal of Endovascular Surgery*, 4:326–338, 1997.
- [18] Stephen P. Johnson, Roy M. Fujitani, John R. Leyendecker, and Frederic B. Joseph. Stent deformation and intimal hyperplasia complicating treatment of a post- carotid endarterectomy intimal flap with a palmaz stent. *Journal of Vascular Surgery*, 25(4):764 – 768, 1997.
- [19] A. Mathur, G. Dorros, S.S. Iyer, J.J. Vitek, S.S. Yadav, and G.S. Roubin. Palmaz stent compression in patients following carotid artery stenting. *Catheterization and Cardiovascular Diagnosis*, 41:137–140, 1997.

- [20] M.H. Wholey and E.A. Finol. Designing the Ideal Stent. *Endovascular Today*, 6:25–34, 2007.
- [21] G.M. Siewiorek, E.A. Finol, and M.H. Wholey. Clinical significance and technical assessment of stent cell geometry in carotid artery stenting. *Journal of Endovascular Therapy*, 16:178–188, 2009.
- [22] D. Carnelli, G. Pennati, T. Villa, L. Baglioni, B. Reimers, and F. Migliavacca. Mechanical properties of open-cell, self-expandable shape memory alloy carotid stents. *Artificial Organs*, 35(1):74–80, 2011.
- [23] S. Müller-Hülsbeck, P. Stolzmann, C. Liess, J. Hedderich, F. Paulsen, T. Jahnke, and M. Heller. Vessel wall damage caused by cerebral protection devices: Ex vivo evaluation in porcine carotid arteries. *Radiology*, 235:454–460, 2005.
- [24] M. Bosiers, G. de Donato, K. Deloose, J. Verbist, P. Peeters, F. Castriota, A. Cremonesi, and C. Setacci. Does Free Cell Area Influence the Outcome in Carotid Artery Stenting? *European Journal of Vascular and Endovascular Surgery*, 33:135–141, 2007.
- [25] G. Lanzino, A.A. Rabinstein, and Brown R.B. Treatment of carotid artery stenosis: Medical therapy, surgery, or stenting? *Mayo clinic proceedings*, 84(4):362–368, 2009.
- [26] M. Bosiers, K. Deloose, J. Verbist, and P. Peeters. What Practical Factors Guide the Choice of Stent and Protection Device during Carotid Angioplasty? *European Journal of Vascular and Endovascular Surgery*, 35:637–643, 2008.
- [27] S. Sayeed, S.F. Stanziale, M.H. Wholey, and M.S. Makaroun. Angiographic lesion characteristics can predict adverse outcomes after carotid artery stenting. *Journal of Vascular Surgery*, 47:81–87, 2008.
- [28] D. Tang, Z. Teng, G. Canton, C. Yang, M. Ferguson, X. Huang, J. Zheng, P. Woodard, and C. Yuan. Sites of Rupture in Human Atherosclerotic Carotid Plaques Are Associated With High Structural Stresses: An In Vivo MRI-Based 3D Fluid-Structure Interaction Study. *Stroke*, 40:3258–3263, 2009.

- [29] J. Egger, S. Grobkopf, and B. Freisleben. Virtual stenting for carotid stenosis with elastic artery wall modeling. *ECIFMBE 2008, IFMBE Proceedings*, 22:2499–2502, 2008.
- [30] P. Mortier, G.A. Holzapfel, M. De Beule, D. Van Loo, Y. Taeymans, P. Segers, P. Verdonck, and B. Verhegghe. A novel simulation strategy for stent insertion and deployment in curved coronary bifurcations: comparison of three drug-eluting stents. *Annals of Biomedical Engineering*, 38:88–99, 2010.
- [31] D. Gastaldi, S. Morlacchi, R. Nichetti, C. Capelli, G. Dubini, L. Petrini, and F. Migliavacca. Modelling of the provisional side-branch stenting approach for the treatment of atherosclerotic coronary bifurcations: effects of stent positioning. *Biomechanics and Modeling in Mechanobiology*, 9(5):551–561, 2010.
- [32] S. Petersen, V. Peto, M. Rayner, J. Leal, R. Luengo-Fernandez, and A. Gray. *European cardiovascular disease statistics*. BHF London, 2005.
- [33] M.H. Wholey, N. Al-Mubarek, and M.H. Wholey. Updated review of the global carotid artery stent registry. *Catheterization and Cardiovascular Interventions*, 60:259–266, 2003.
- [34] A.J. Furlan. Carotid Artery Stenting - Case Open or Closed? *New England Journal of Medicine*, 355:1726–1729, 2006.
- [35] N. Al-Mubarak, A. Colombo, and P. Gaines et al. Multicenter evaluation of carotid artery stenting with a filter protection system. *Journal of the American College of Cardiology*, 39:841–846, 2002.
- [36] J.S. Yadav, M.H. Wholey, R.E. Juntz, P. Fayad, B.T. Katzen, G.J. Mishkel, T.K. Bajwa, P. Whitlow, N.E. Strickman, M.R. Jaff, J.J. Popma, D.B. Snead, D.E. Cutlip, B.G. Firth, and K. Ouriel. Protected carotid artery stenting versus endarterectomy in high-risk patients. *New England Journal of Medicine*, 351:1493–1501, 2004.
- [37] P.P. Goodney, M.L. Schermerhorn, and R.J. Powell. Current status of carotid artery stenting. *Journal of Vascular Surgery*, 43:406–411, 2006.

- [38] CaRESS Steering Committee. Carotid revascularization using endarterectomy or stenting systems (caress) phase i clinical trial: 1-year results. *Journal of Vascular Surgery*, 42:213–219, 2005.
- [39] M.H. Yen, D.S. Lee, S. Kapadia, R. Sachar, D.L. Bhatt, C.T. Bajzer, and J.S. Yadav. Symptomatic patients have similar outcomes compared with asymptomatic patients after carotid artery stenting with emboli protection. *American Journal of Cardiology*, 95:297–300, 2005.
- [40] M.K. Eskandari, S.F. Najjar, J.S. Matsumura, M.R. Kibbe, and M.D. Morasch. Symptomatic patients have similar outcomes compared with asymptomatic patients after carotid artery stenting with emboli protection. *Annals of Vascular Surgery*, 21:403–407, 2007.
- [41] F. Fanelli, M. Bezzi, E. Boatta, and R. Passariello. Techniques in cerebral protection. *European Journal of Radiology*, 60:26–36, 2006.
- [42] K. Kasirajan, P.A. Schneider, and K.C. Kent. Filter devices for cerebral protection during carotid angioplasty and stenting. *Journal of Endovascular Therapy*, 10:1039–1045, 2003.
- [43] G.M. Siewiorek, M.H. Wholey, and E.A. Finol. Performance assessment of distal protection devices for carotid artery stenting: Effect of physiological anatomy on vascular resistance. *Journal of Endovascular Therapy*, 14:712–724, 2007.
- [44] F. Auricchio, M. Di Loreto, and E. Sacco. Finite element analysis of a stenotic artery revascularization through stent insertion. *Computer Methods in Biomechanics and Biomedical Engineering*, 4:249–263, 2001.
- [45] M. De Beule, P. Mortier, S.G. Carlier, B. Verhegghe, R. Van Impe, and P. Verdonck. Realistic finite element-based stent design: the impact of balloon folding. *Journal of Biomechanics*, 41:383–389, 2008.
- [46] C. Lally, F. Dolan, and P. Prendergast. Cardiovascular Stent Design and Vessel Stresses: a Finite Element Analysis. *Journal of Biomechanics*, 38:1574–1581, 2005.
- [47] P. Mortier, M. De Beule, S.G. Carlier, R. Van Impe, B. Verhegghe, and P. Verdonck. Numerical Study of the Uniformity of Balloon-

- Expandable Stent Deployment. *Journal of Biomechanical Engineering*, 130:021018, 2008.
- [48] S. Müller-Hülsbeck, T. Jahnke, C. Liess, C. Glass, J. Grimm, and M. Heller. Comparison of various cerebral protection devices used for carotid artery stent placement: An in vitro experiment. *Journal of Vascular and Interventional Radiology*, 14:613–620, 2003.
- [49] S. Müller-Hülsbeck, J. Grimm, C. Liess, J. Hedderich, M. Bergmeyer, and M. Heller. Comparison and modification of two cerebral protection devices used for carotid angioplasty: In vitro experiment. *Radiology*, 225:289–294, 2002.
- [50] S. Müller-Hülsbeck, T. Jahnke, C. Liess, C. Glass, F. Paulsen, J. Grimm, and M. Heller. In vitro comparison of four cerebral protection filters for preventing human plaque embolization during carotid interventions. *Journal of Endovascular Therapy*, 9:793–802, 2002.
- [51] Cordis. Instructions for use angioguard xp™ emboli capture guidewire system. accessed 16 march 2009. www.cordislabeling.com/pdf/24408544_3.pdf, 2009.
- [52] pyFormex. A tool for generating, manipulating and operating on large geometrical models of 3d structures by sequences of mathematical transformations. accessed september 1, 2009. <http://pyformex.berlios.de/>, 2009.
- [53] A.R. Pelton, J. DiCello, and S. Miyazaki. Self-expanding nitinol stents: material and design considerations. *Minimally Invasive Therapy and Allied Technologies*, 9(1):107–118, 2000.
- [54] Cabot Corp. Tantalum material properties from cabot corp. accessed august 2010. <http://www.cabot-corp.com/Tantalum>, 2010.
- [55] Bumper-cluster. A low cost/high performance linux cluster dedicated to computational mechanics. accessed september 1, 2009. <http://bumps.ugent.be/bumper/>, 2009.
- [56] J.M. Hendriks, J.D. Zindler, A. van der Lugt, P. Pattynama, M. van Sambeek, J. Bosch, and L. van Dijk. Embolic protection filters for carotid artery stenting: Differences in flow obstruction depending on filter construction. *Journal of Endovascular Therapy*, 13:47–50, 2006.

- [57] G.M. Siewiorek, M.H. Wholey, and E.A. Finol. Vascular resistance in the carotid artery: An in vitro investigation of embolic protection filters. *Journal of Vascular and Interventional Radiology*, 19:1467–1476, 2008.
- [58] Food and Drug Administration US. *Guidance for Industry and FDA Staff, Coronary and Carotid Embolic Protection Devices - Premarket Notification [510(k)] Submissions*. 2009.
- [59] S. Chaturvedi, A. Bruno, T. Feasby, R. Holloway, O. Benavente, S.N. Cohen, R. Cote, D. Hess, J. Saver, J.D. Spence, B. Stern, and J. Wilterdink. Carotid endarterectomy - an evidence-based review: report of the Therapeutics and Technology Assessment Subcommittee of the American Academy of Neurology. *Neurology*, 65:794–801, 2005.
- [60] Cavatas. Endovascular versus surgical treatment in patients with carotid stenosis in the Carotid and Vertebral Artery Transluminal Angioplasty Study (CAVATAS): a randomised trial. *Lancet*, 357:1729–1737, 2001.
- [61] M.A. Creager, C.R. White, W.R. Hiatt, M.H. Criqui, S.C. Josephs, M.J. Alberts, W.H. Pearce, B.H. Gray, and K.J. Rocha-Singh. Atherosclerotic Peripheral Vascular Disease Symposium II: Executive Summary. *Circulation*, 118:2811–2825, 2008.
- [62] T.L. Forbes. Preliminary results of Carotid Revascularization Endarterectomy vs Stenting Trial (CREST). *Journal of Vascular Surgery*, 51:1300–1301, 2010.
- [63] Z. Liu, Z. Shi, Y. Wang, B. Chen, T. Zhu, Y. Si, and W. Fu. Carotid Artery Stenting Versus Carotid Endarterectomy: Systematic review and Meta-Analysis. *World J Surg*, 33:586–596, 2009.
- [64] S. Brahmanandam, E.L. Ding, M.S. Conte, M. Belkin, and L.L. Nguyen. Clinical results of carotid artery stenting compared with carotid endarterectomy. *Journal of Vascular Surgery*, 47:343–349, 2008.
- [65] P. Mortier, M. De Beule, D. Van Loo, B. Verheghe, and P. Verdonck. Finite element analysis of side branch access during bifurcation stenting. *Medical Engineering & Physics*, 31:434–440, 2009.

- [66] I. Pericevic, C. Lally, D. Toner, and D.J. Kelly. The influence of plaque composition on underlying arterial wall stress during stent expansion: The case for lesion-specific stents. *Medical Engineering & Physics*, 31:428–433, 2009.
- [67] M. Conti, M. De Beule, P. Mortier, D. Van Loo, P. Verdonck, F. Vermassen, P. Segers, F. Auricchio, and B. Verhegghe. Nitinol Embolic Protection Filters: design investigation by Finite Element Analysis. *Journal of Materials Engineering and Performance*, 18:787–792, 2009.
- [68] M. Conti, F. Auricchio, M. De Beule, and B. Verhegghe. Numerical simulation of Nitinol peripheral stents: from laser-cutting to deployment in a patient specific anatomy. *Proceeding of ESOMAT 2009*, page 06008, 2009.
- [69] W. Wu, M. Qi, X.P. Liu, D.Z. Yang, and W.Q. Wang. Delivery and release of nitinol stent in carotid artery and their interactions: A finite element analysis. *Journal of Biomechanics*, 40:3034–3040, 2007.
- [70] G. De Santis, P. Mortier, M. De Beule, P. Segeres, P. Verdock, and B. Verhegghe. Patient-specific computational fluid dynamics: structured mesh generation from coronary angiography. *Medical & Biological Engineering & Computing Medical & Biological Engineering & Computing*, 48:371–378, 2010.
- [71] G. De Santis, M. De Beule, P. Segeres, P. Verdock, and B. Verhegghe. Patient-specific computational hemodynamics: Generation of structured and conformal hexahedral meshes from triangulated surfaces of vascular bifurcations. *Computer Methods in Biomechanics and Biomedical Engineering (in press)*, 2010.
- [72] G. Sommer, P. Regitnig, L. Koltringer, and G. Holzapfel. Biaxial mechanical properties of intact and layer-dissected human carotid arteries at physiological and suprphysiological loadings. *American Journal of Physiology - Heart and Circulatory Physiology*, 298:H898–912, 2009.
- [73] P.J. Prendergast, C. Lally, S. Daly, A.J. reid, T.C. Lee, D. Quinn, and F. Dolan. Analysis of prolapse in cardiovascular stents: a constitutive equation for vascular tissue and finite-element modellin. *Journal of Biomechanical Engineering*, 125:693–699, 2003.

- [74] M. De Beule. *Finite Element Stent Design*. PhD Thesis, Ghent University, Belgium, 2008.
- [75] M. De Beule, S. Van Cauter, P. Mortier, D. Van Loo, R. Van Impe, P. Verdonck, and B. Verheghe. Virtual stent optimization of self-expandable braided wire stents. *Medical Engineering & Physics*, 31:448–453, 2009.
- [76] N. Rebelo, N. Walker, and H. Foadian. Simulation of implantable stents. *Abaqus User's Conference*, 143:421–434, 2001.
- [77] F. Auricchio and R. Taylor. Shape-memory alloys: macromodeling and numerical simulations of the superelastic behavior. *Computer Methods in Applied Mechanics and Engineering*, 146:281–312, 1997.
- [78] F. Auricchio and R. Taylor. Shape-memory alloys: modeling and numerical simulations of the finite-strain superelastic behavior. *Computer Methods in Applied Mechanics and Engineering*, 143:175–194, 1996.
- [79] J. Lubliner and F. Auricchio. Generalized plasticity and shape memory alloy. *Int. J. Solid Strc*, 33:991–1003, 1996.
- [80] C. Kleinstreuer, Z. Li, C.A. Basciano, S. Seelecke, and M.A. Farber. Computational mechanics of Nitinol stent grafts. *Journal of Biomechanics*, 41:2370–2378, 2008.
- [81] O.C. Clerc, M.R. Jedwab, D.W. Mayer, P.J. Thompson, and J.S. Stinson. Assessment of Wrought ASTM F1058 Cobalt Alloy Properties for Permanent Surgical Implants. *Journal of Biomedical Materials Research*, 38:229–234, 1997.
- [82] E.R. Edelman and C. Rogers. Pathobiologic response to stenting. *American Journal of Cardiology*, 81:4E–6E, 1998.
- [83] J.B. Thomas, L. Antiga, S.L. Che, J.S. Milner, D.A. Hangan Steinman, J.D. Spence, B.K. Kutt, and D.A. Steinman. Variation in the Carotid Bifurcation Geometry of Young Versus Older Adults: Implications for Geometric Risk of Atherosclerosis. *Stroke*, 36:2450–6, 2005.

- [84] T.T. de Weert, M. Ouhlous, E. Meijering, P.E. Zondervan, J.M. Hendriks, M.R.H.M. van Sambeek, D.W.J. Dippel, and A. van der Lugt. In Vivo Characterization and Quantification of Atherosclerotic Carotid Plaque with Components With Multidetector Computed Tomography and Histopathological correlation. *Arteriosclerosis, Thrombosis, and Vascular Biology*, 26:2366–2372, 2006.
- [85] T.T. de Weert, M. Ouhlous, P.E. Zondervan, J.M. Hendriks, D.W.J. Dippel, M.R.H.M. van Sambeek, and A. van der Lugt. In vitro characterization of atherosclerotic carotid plaque with multidetector computed tomography and histopathological correlation. *European Radiology*, pages 1906–1914, 2005.
- [86] A. Creane, E. Maher, S. Sultan, N. Hynes, D.J. Kelly, and C. Lally. Finite element modelling of diseased carotid bifurcations generated from in vivo computerised tomographic angiography. *Computers in Biology and Medicine*, 40:419–429, 2010.
- [87] G.W. Albers, Y.J. Chang, and A.J. Golby. Detection of carotid stenosis: from NASCET results to clinical practice. *Stroke*, 26:1325–1328, 1995.
- [88] B.D. Stemper, N. Yoganandan, and F.A. Pintar. Methodology to study intimal failure mechanics in human internal carotid arteries. *Journal of Biomechanics*, 38:2491–2496, 2005.
- [89] D. Tang, C. Yang, S. Kobayashi, and N.K. Ku. Effect of a Lipid Pool on Stress/Strain Distributions in Stenotic Arteries: 3-D Fluid-Structure Interactions (FSI) Models. *Journal of Biomechanical Engineering*, 126:363–370, 2004.
- [90] A. Delfino, N. Stergiopoulos, J.E. Moore, and J.J. Meister. Residual strain effects in the stress field in a thick wall finite element model of the human carotid bifurcation. *Journal of Biomechanics*, 30:777–786, 1997.
- [91] P. Serruys, M.J.B. Kutryk, and A.T.L. Ong. Coronary-artery stents. *New England Journal of Medicine*, 354:483–495, 2006.
- [92] K. Gröschel, A. Riecker, J.B. Schulz, U. Ernemann, and A. Kastrup. Systematic review of early recurrent stenosis after angioplasty and stenting. *Stroke*, 36:367–373, 2005.

- [93] M. Henry, I. Henry, C. Klonaris, I. Masson, M. Hugel, K. Tzvetanov, G. Ethevenot, B.E. Le, S. Kownator, F. Luizi, and B. Folliguet. Benefits of cerebral protection during carotid stenting with the percusurge guardwire system: midterm results. *Journal of Endovascular Therapy*, 9:1–13, 2002.
- [94] M.H. Christiaans, J.M. Ernst, M.J. Suttorp, J.C. van den Berg, T.T. Overtom, J.C. Kelder, H.W. Mauser, R.G. Ackerstaff, and Antonius Carotid Endarterectomy, Angioplasty, and Stenting Study Group. Restenosis after carotid angioplasty and stenting: a follow-up study with duplex ultrasonography. *European Journal of Vascular and Endovascular Surgery*, 26:141–144, 2003.
- [95] M. Bosiers, P. Peeters, K. Deloose, J. Verbist, H. Sievert, J. Sugita, F. Castriota, and A. Cremonesi. Does carotid artery stenting work on the long run: 5-year results in high-volume centers (ELOCAS Registry). *Journal of Cardiovascular Surgery (Torino)*, 46:241–247, 2005.
- [96] G. De Donato, C. Setacci, K. Deloose, P. Peeters, A. Cremonesi, and M. Bosiers. Long-term results of carotid artery stenting. *Journal of Vascular Surgery*, 48:1431–1441, 2008.
- [97] M.G.M. Steinbauer, K. Pfister, M. Greind, F. Schlachetzki, I. Borisch, G. Schuirer, S. Feuerbach, and P.M. Kasprzak. Alert for increased long-term follow-up after carotid artery stenting: Results of a prospective, randomized, single-center trial of carotid artery stenting vs carotid endarterectomy. *Journal of Vascular Surgery*, 48:93–98, 2008.
- [98] J.U. Harrer, R. Morschel, M. Mull, and C.M. Kosinski. High rate of restenosis after carotid artery stenting in patients with high-grade internal carotid artery stenosis. *Journal of Neurology*, 255:1309–1314, 2008.
- [99] R. Nolz, R.E. Schernthaner, M. Cejna, M. Schernthaner, J. Lammer, and M. Schoder. Carotid artery stenting: Single-center experience over 11 years. *Cardiovasc Intervent Radiol*, 33:251–259, 2010.
- [100] R.S. Schwartz and K.C. Huber. Restenosis and the proportional neointimal response to coronary artery injury: results in a porcine model. *Journal of the American College of Cardiology*, 19:267–274, 1992.

- [101] R. Kornowski, M.K. Hong, F.O. Tio, O. Bramwell, H.W. Wu, and M.B. Leon. In-stent restenosis: contributions of inflammatory responses and arterial injury to neointimal hyperplasia. *Journal of the American College of Cardiology*, 31:224–230, 1998.
- [102] D. Kioussis, C. Gasser, and G.A. Holzapfel. A numerical model to study the interaction of vascular stents with human atherosclerotic lesions. *Annals of Biomedical Engineering*, 11:1857–1869, 2007.
- [103] F. Gijssen, F. Migliavacca, S. Schievano, L. Socci, L. Petrini, A. Thury, J. Wentzel, A. van der Steen, P. Serruys, and G. Dubini. Simulation of stent deployment in a realistic human coronary artery. *BioMedical Engineering OnLine*, 7, 2008.
- [104] F. Auricchio, M. Conti, M. De Beule, G. De Santis, and B. Verheghe. Carotid artery stenting simulation: from patient-specific images to finite element analysis. *Medical Engineering & Physics*, in press, 2010.
- [105] A. Rosset, L. Spadola, and O. Ratib. Osirix: An open-source software for navigating in multidimensional dicom images. *Journal of Digital Imaging*, 17:205–216, 2004.
- [106] A. Delfino. Analysis of the stress field in a model of the human carotid bifurcation. *Ph.D. thesis. Federal Institute of Technology Lausanne. Switzerland.*, 1996.
- [107] I. Hariton, G. deBotton, T.C. Gasser, and G.A. Holzapfel. Stress-modulated collagen fiber remodeling in a human carotid bifurcation. *Journal of Theoretical Biology*, 248:460–470, 2007.
- [108] G.A. Holzapfel, T.C. Gasser, and R.W. Ogden. A new constitutive framework for arterial wall mechanics and a comparative study of material models. *J Elast*, 61:1–48, 2000.
- [109] G.A. Holzapfel, C.A.J. Schulze-Bauer, and M. Stadler. *Mechanics of angioplasty: wall, balloon and stent*. Springer, Berlin Heidelberg New York, 2000.
- [110] H. Gao and Q. Long. Effects of varied lipid core volume and fibrous cap thickness on stress distribution in carotid arterial plaques. *Journal of Biomechanics*, 41, 2008.

- [111] C. Yang, D. Tang, C. Yuan, T.S. Hatsukami, J. Zheng, and P.K. Woodard. In Vivo/Ex Vivo MRI-Based 3D Non-Newtonian FSI Models for Human Atherosclerotic Plaques Compared with Fluid/Wall-Only Models. *Computer Modeling in Engineering & Sciences*, 19:233–246, 2007.
- [112] D. Tang, C. Yang, S. Mondal, F. Liu, G. Canton, T.S. Hatsukami, and C. Yuan. A negative correlation between human carotid atherosclerotic plaque progression and plaque wall stress: In vivo MRI-based 2D/3D FSI models. *Journal of Biomechanics*, 41:727–736, 2008.
- [113] J.D. Humphrey. *Cardiovascular Solid Mechanics*. Springer-Verlag; New York, 2002.
- [114] S. Kobayashi, D. Tsunoda, Y. Fukuzawa, H. Morikawa, D. Tang, and D.N. Ku. Flow and compression in arterial models of stenosis with lipid core. *Proceedings of 2003 ASME Summer Bioengineering Conference*, pages 497–498, 2003.
- [115] E. Maher, A. Creane, S. Sultan, N. Hynes, C. Lally, and D.J. Kelly. Tensile and compressive properties of fresh human carotid atherosclerotic plaques. *Journal of Biomechanics*, 16:2760–2767, 2009.
- [116] Gerhard Sommer. *Mechanical Properties of Healthy and Diseased Human Arteries: Insights into Human Arterial Biomechanics and Related Material Modeling*. Monographic Series TU Graz, Computation in Engineering and Science, 2010.
- [117] T.C. Gasser, R.W. Ogden, and G.A. Holzapfel. Hyperelastic modelling of arterial layers with distributed collagen fibre orientations. *Journal of the Royal Society Interface*, 3:15–35, 2006.
- [118] C. Lally, F. Dolan, and P. Prendergast. Erratum to Cardiovascular Stent Design and Vessel Stresses: a Finite Element Analysis. *Journal of Biomechanics*, 39:1760, 2005.
- [119] Simulia. *Abaqus Manual*. Dassault Systèmes, Providence, RI, USA, 2009.
- [120] D. Kioussis, S.F. Rubinigg, M. Auer, and G.A. Holzapfel. A Methodology to Analyze Changes in Lipid Core and Calcification Onto Fibrous Cap Vulnerability: The Human Atherosclerotic Carotid Bifurcation

- as an Illustratory Example. *Journal of Biomechanical Engineering*, 131:121002(9 pages), 2009.
- [121] G.A. Holzapfel, M. Stadler, and C.A. Schulze-Bauer. A layer-specific three dimensional model for the simulation of balloon angioplasty using magnetic resonance imaging and mechanical testing. *Annals of Biomedical Engineering*, 30:753–767, 2002.
- [122] Thomas S. Maldonado. What are current preprocedure imaging requirements for carotid artery stenting and carotid endarterectomy: Have magnetic resonance angiography and computed tomographic angiography made a difference? *Seminars in Vascular Surgery*, 20(4):205 – 215, 2007.
- [123] Brad C. Astor, A. Richey Sharrett, Josef Coresh, Lloyd E. Chambless, and Bruce A. Wasserman. Remodeling of Carotid Arteries Detected with MR Imaging: Atherosclerosis Risk in Communities Carotid MRI Study1. *Radiology*, 256(3):879–886, 2010.
- [124] G.A. Holzapfel, G. Sommer, and P. Regitnig. Anisotropic mechanical properties of the tissue components in human atherosclerotic plaques. *Journal of Biomechanical Engineering*, 126:657–665, 2004.
- [125] I. Hariton, G. deBotton, T.C. Gasser, and G.A. Holzapfel. How to incorporate collagen fibers orientations in an arterial bifurcation? *Proceeding of 3rd IASTED Int Conference on Biomechanics*, 2005.
- [126] SPACE Collaborative Group. 30 day results from the space trial of stent-protected angioplasty versus carotid endarterectomy in symptomatic patients: a randomised non-inferiority trial. *Lancet*, 368:1239–1247, 2006.
- [127] EVA-3S Investigators. Endarterectomy versus stenting in patients with symptomatic severe carotid stenosis. *New England Journal of Medicine*, 355:1660–1671, 2006.
- [128] E. Lim, A. Brown, A. Helmy, S. Mussa, and D.G. Altman. Composite outcomes in cardiovascular research: A survey of randomized trials. *Annals of Internal Medicine*, 149:612–618, 2008.
- [129] M.H. Wholey, M. Wholey, K. Mathias, G.S. Roubin, E.B. Diethrich, M. Henry, S. Bailey, P. Bergeron, G. Dorros, G. Eles, P. Gaines, C.R.

- Gomez, B. Gray, J. Guimaraens, R. Higashida, D.S. Ho, B. Katzen, A. Kambara, V. Kumar, J.C. Laborde, M. Leon, M. Lim, H. Londero, J. Mesa, A. Musacchio, S. Myla, S. Ramee, A. Rodriguez, K. Rosenfield, F. Shawl, H. Sievert, G. Teitelbaum, J.G. Theron, P. Vaclav, C. Vozzi, J.S. Yadav, and S.I. Yoshimura. Global experience in cervical carotid artery stent placement. *Catheter Cardiovasc Interv*, 50:160–167, 2000.
- [130] A. Cremonesi, R. Manetti, C. Setacci, and F. Castriota. Protected carotid stenting: clinical advantages and complications of emboli protection devices in 442 consecutive patients. *Stroke*, 34:1936–1941, 2003.
- [131] C. Sherif, P. Dick, S. Sabeti, W. Mlekusch, J. Amighi, R. Ahmadi, W. Lalouschek, E. Minar, and M. Schillinger. Neurological outcome after carotid artery stenting compared to medical therapy in patients with asymptomatic high grade carotid artery stenosis. *J Endovasc Ther.*, 12:145–155, 2005.
- [132] J. Boltuch, S. Sabeti, J. Amighi, W. Mlekusch, P. Dick, O. Schlager, R. Ahmadi, E. Minar, and M. Schillinger. Procedure-related complications and neurological adverse events after protected vs. unprotected carotid stenting. *J Endovasc Ther.*, 12:538–547, 2005.
- [133] A. Cremonesi, C. Setacci, F. Castriota, and M. Valgimigli. Carotid stent cell design: lack of benefit or lack of evidence? *Stroke*, 39:e130, 2009.
- [134] C. Setacci, G. de Donato, and M. Bosiers. Two different studies on carotid stent cell design importance, or are we just saying the same thing? *Stroke*, 39:e129, 2008.
- [135] M. Schillinger, M. Gschwendtner, B. Reimers, J. Trenkler, L. Stockx, J. Mair, S. Macdonald, F. Karnel, K. Huber, and E. Minar. Does carotid stent cell design matter? *Stroke*, 39:905–909, 2008.
- [136] J.P. Hart, P. Peeters, J. Verbist, K. Deloose, and M. Bosiers. Do device characteristics impact outcome in carotid artery stenting? *J of Vascular Surgery*, 44:725–730, 2006.

- [137] N. Tanaka, J.B. Martin, K. Tokunaga, T. Abe, Y. Uchiyama, N. Hayabuchi, J. Berkefeld, and D.A. Rufenacht. Conformity of Carotid Stents with Vascular Anatomy: Evaluation in Carotid Models. *American Society of Neuroradiology*, 25:604–607, 2004.
- [138] S. Müller-Hülsbeck, P.J Schäfer, N. Charalambous, S.R. Schaffner, M. Heller, and T. Jahnke. Comparison of carotid stents: An in-vitro experiment focusing on stent design. *Journal of Endovascular Therapy*, 16:168–177, 2009.
- [139] G.M. Siewiorek, M.H. Wholey, and E.A. Finol. In vitro performance assessment of distal protection filters: Pulsatile flow conditions. *Journal of Endovascular Therapy*, 16:735–743, 2009.
- [140] C.R. Bartoli, P.A. Spence, and G.A. Giridharan. Novel J stents reduce the risk of embolic stroke in vitro. *Neuroradiology*, 52:345–347, 2010.
- [141] A.R. Pelton, V. Schroeder, M.R. Mitchell, X.Y. Gong, M. Barney, and S.W. Robertson. Fatigue and durability of nitinol stents. *Fatigue and durability of Nitinol stents*, 1:153–164, 2008.
- [142] A. Sulaiman, L. Boussel, F. Taconnet, J.M. Serfaty, H. Alsaïd, C. Attia, L. Huet, and P. Douek. In vitro non-rigid life-size model of aortic arch aneurysm for endovascular prosthesis assessment. *European Journal of Cardio-thoracic Surgery*, 33:53–57, 2008.
- [143] Ouriel. K. Endovascular skills training and assessment. *European Journal of Cardio-thoracic Surgery*, 46:1055–64, 2007.
- [144] S. Müller-Hülsbeck, E.J. Hüsler, S.R. Schaffner, T. Jahnke, C. Glass, R. Wenke, and M. Heller. An in vitro analysis of a carotid artery stent with a protective porous membrane. *Journal of Vascular and Interventional Radiology*, 15:1295–1305, 2004.
- [145] Y. Suzuki, M. Fujitsika, and J. Chaloupa. Simulation of Endovascular Neurointervention Using Silicone Models: Imaging and Manipulation. *Neurol Med Chir (Tokyo)*, 45:567–573, 2005.
- [146] R. Ramesh, E.R. Strobe, K.S. Price, and J.C. Conti. Frequency dependent hysteresis of silicone and latex mock arteries used in stent testing. *Biomedical Science Instrumentation*, 41:163–168, 2005.

- [147] N. Rebelo, R. Fu, and M. Lawrenchuk. Study of a Nitinol Stent Deployed into Anatomically Accurate Artery Geometry and Subjected to Realistic Service Loading. *Journal of Materials Engineering and Performance*, doi: 10.1007/s11665-009-9375-0:655–663, 2009.
- [148] P. Thériault, P. Terriault, V. Brailovski, and R. Gallo. Finite element modeling of a progressively expanding shape memory stent. *Journal of Biomechanics*, 39:2837–2844, 2006.
- [149] S. Prabhu, C. Feezor, A. Denison, N. Rebelo, and M. Serrar. Deployment of a Self-expanding Stent in an Artery. *Abaqus Users' Conference*. Available from: www.simulia.com, 2004.
- [150] P. Mortier, D. Van Loo, M. De Beule, P. Segers, Y. Taeymans, P. Verdonck, and B. Verheghe. Comparison of drug-eluting stent cell size using micro-ct: important data for bifurcation stent selection. *Eurointervention*, 4:391–396, 2000.
- [151] T. Okamura, S. Garg, J.L. Gutiérrez-Chico, E.S. Shin, Y. Onuma, H.M. García-García, R.J. Rapoza, K. Sudhir, E. Regar, and P.W. Serruys. In vivo evaluation of stent strut distribution patterns in the bioabsorbable everolimus-eluting device: an oct ad hoc analysis of the revision 1.0 and revision 1.1 stent design in the absorb clinical trial. *EuroIntervention*, 5:932–938, 2010.
- [152] R.L. Varcoe, J Mah, N. Young, S.S. So, M. Vicaretti, and J. Swinnen. Prevalence of carotid stent fractures in a single-center experience. *J Endovasc Ther.*, 15:485–489, 2008.
- [153] L. Antiga and D. Steinman. Robust and objective decomposition and mapping of bifurcating vessels. *IEEE Transactions on Medical Imaging*, in press.
- [154] Q. Long, X.Y. Xu, M.W. Collins, M. Bourne, and T.M. Griffith. Magnetic resonance image processing and structured grid generation of a human abdominal bifurcation. *Computer Methods and Programs in Biomedicine*, 56:249–259, 1998.
- [155] J.A. Cottrell, T.J.R Hughes, and Y. Bazilevs. *Isogeometric Analysis: Toward Integration of CAD and FEA*. Wiley, 2010.